

Wireless Communications and Mobile Computing

Machine Learning for Communication Performance Enhancement

Lead Guest Editor: Xin-Lin Huang

Guest Editors: Fei Hu, Xiaomin Ma, Ioannis Krikidis, and Dejan Vukobratovic





Machine Learning for Communication Performance Enhancement

Wireless Communications and Mobile Computing

Machine Learning for Communication Performance Enhancement

Lead Guest Editor: Xin-Lin Huang

Guest Editors: Fei Hu, Xiaomin Ma, Ioannis Krikidis,
and Dejan Vukobratovic



Copyright © 2018 Hindawi. All rights reserved.

This is a special issue published in “Wireless Communications and Mobile Computing.” All articles are open access articles distributed under the Creative Commons Attribution License, which permits unrestricted use, distribution, and reproduction in any medium, provided the original work is properly cited.

Editorial Board

- Javier Aguiar, Spain
Wessam Ajib, Canada
Muhammad Alam, China
Eva Antonino-Daviu, Spain
Shlomi Arnon, Israel
Leyre Azpilicueta, Mexico
Paolo Barsocchi, Italy
Alessandro Bazzi, Italy
Zdenek Becvar, Czech Republic
Francesco Benedetto, Italy
Olivier Berder, France
Ana M. Bernardos, Spain
Mauro Biagi, Italy
Dario Bruneo, Italy
Jun Cai, Canada
Zhipeng Cai, USA
Claudia Campolo, Italy
Gerardo Canfora, Italy
Rolando Carrasco, UK
Vicente Casares-Giner, Spain
Luis Castedo, Spain
Ioannis Chatzigiannakis, Greece
Lin Chen, France
Yu Chen, USA
Hui Cheng, UK
Ernestina Cianca, Italy
Riccardo Colella, Italy
Mario Collotta, Italy
Massimo Condoluci, Sweden
Daniel G. Costa, Brazil
Bernard Cousin, France
Telmo Reis Cunha, Portugal
Igor Curcio, Finland
Laurie Cuthbert, Macau
Donatella Darsena, Italy
Pham Tien Dat, Japan
André de Almeida, Brazil
Antonio De Domenico, France
Antonio de la Oliva, Spain
Gianluca De Marco, Italy
Luca De Nardis, Italy
Liang Dong, USA
Mohammed El-Hajjar, UK
Oscar Esparza, Spain
- Maria Fazio, Italy
Mauro Femminella, Italy
Manuel Fernandez-Veiga, Spain
Gianluigi Ferrari, Italy
Ilario Filippini, Italy
Jesus Fontecha, Spain
Luca Foschini, Italy
A. G. Fragkiadakis, Greece
Sabrina Gaito, Italy
Óscar García, Spain
Manuel García Sánchez, Spain
L. J. García Villalba, Spain
José A. García-Naya, Spain
Miguel Garcia-Pineda, Spain
A.-J. García-Sánchez, Spain
Piedad Garrido, Spain
Vincent Gauthier, France
Carlo Giannelli, Italy
Carles Gomez, Spain
Juan A. Gomez-Pulido, Spain
Ke Guan, China
Antonio Guerrieri, Italy
Daojing He, China
Paul Honeine, France
Sergio Ilarri, Spain
Antonio Jara, Switzerland
Xiaohong Jiang, Japan
Minho Jo, Republic of Korea
Shigeru Kashiara, Japan
Dimitrios Katsaros, Greece
Minseok Kim, Japan
Mario Kolberg, UK
Nikos Komninos, UK
Juan A. L. Riquelme, Spain
Pavlos I. Lazaridis, UK
Tuan Anh Le, UK
Xianfu Lei, China
Hoa Le-Minh, UK
Jaime Lloret, Spain
Miguel López-Benítez, UK
Martín López-Nores, Spain
Javier D. S. Lorente, Spain
Tony T. Luo, Singapore
Maode Ma, Singapore
- Imadeldin Mahgoub, USA
Pietro Manzoni, Spain
Álvaro Marco, Spain
Gustavo Marfia, Italy
Francisco J. Martinez, Spain
Davide Mattera, Italy
Michael McGuire, Canada
Nathalie Mitton, France
Klaus Moessner, UK
Antonella Molinaro, Italy
Simone Morosi, Italy
Kumudu S. Munasinghe, Australia
Enrico Natalizio, France
Keivan Navaie, UK
Thomas Newe, Ireland
Wing Kwan Ng, Australia
Tuan M. Nguyen, Vietnam
Petros Nicopolitidis, Greece
Giovanni Pau, Italy
Rafael Pérez-Jiménez, Spain
Matteo Petracca, Italy
Nada Y. Philip, UK
Marco Picone, Italy
Daniele Pinchera, Italy
Giuseppe Piro, Italy
Vicent Pla, Spain
Javier Prieto, Spain
Rüdiger C. Prys, Germany
Sujan Rajbhandari, UK
Rajib Rana, Australia
Luca Reggiani, Italy
Daniel G. Reina, Spain
Abusayeed Saifullah, USA
Jose Santa, Spain
Stefano Savazzi, Italy
Hans Schotten, Germany
Patrick Seeling, USA
Muhammad Z. Shakir, UK
Mohammad Shojafar, Italy
Giovanni Stea, Italy
Enrique Stevens-Navarro, Mexico
Zhou Su, Japan
Luis Suarez, Russia
Ville Syrjälä, Finland



Hwee Pink Tan, Singapore
Pierre-Martin Tardif, Canada
Mauro Tortonesi, Italy
Federico Tramarin, Italy
Reza Monir Vaghefi, USA

Juan F. Valenzuela-Valdés, Spain
Aline C. Viana, France
Enrico M. Vitucci, Italy
Honggang Wang, USA
Jie Yang, USA

Sherali Zeadally, USA
Jie Zhang, UK
Meiling Zhu, UK

Contents

Machine Learning for Communication Performance Enhancement

Xin-Lin Huang , Fei Hu, Xiaomin Ma , Ioannis Krikidis, and Dejan Vukobratovic
Editorial (2 pages), Article ID 3018105, Volume 2018 (2018)

WiFi Positioning Based on User Orientation Estimation and Smartphone Carrying Position Recognition

Zhi-An Deng , Zhiyu Qu , Changbo Hou, Weijian Si, and Chunjie Zhang
Research Article (11 pages), Article ID 5243893, Volume 2018 (2018)

Distributed Routing Strategy Based on Machine Learning for LEO Satellite Network

Zhenyu Na , Zheng Pan, Xin Liu , Zhian Deng , Zihao Gao, and Qing Guo 
Research Article (10 pages), Article ID 3026405, Volume 2018 (2018)

Pedestrian Motion Learning Based Indoor WLAN Localization via Spatial Clustering

Xiaolong Yang , Yanmeng Wang , Mu Zhou , and Yiyao Liu
Research Article (10 pages), Article ID 2571671, Volume 2018 (2018)

Multilayer Learning Network for Modulation Classification Assisted with Frequency Offset Cancellation in Satellite to Ground Link

Guan Qing Yang 
Research Article (13 pages), Article ID 1372439, Volume 2018 (2018)

The Parallel Algorithm Based on Genetic Algorithm for Improving the Performance of Cognitive Radio

Liu Miao , Zhenxing Sun, and Zhang Jie
Research Article (6 pages), Article ID 5986482, Volume 2018 (2018)

Editorial

Machine Learning for Communication Performance Enhancement

Xin-Lin Huang ¹, Fei Hu,² Xiaomin Ma ³, Ioannis Krikidis,⁴ and Dejan Vukobratovic⁵

¹Tongji University, Shanghai, China

²The University of Alabama, Tuscaloosa, AL, USA

³Oral Roberts University, Tulsa, OK, USA

⁴University of Cyprus, Nicosia, Cyprus

⁵University of Novi Sad, Novi Sad, Serbia

Correspondence should be addressed to Xin-Lin Huang; xlhuang@tongji.edu.cn

Received 8 October 2018; Accepted 9 October 2018; Published 1 November 2018

Copyright © 2018 Xin-Lin Huang et al. This is an open access article distributed under the Creative Commons Attribution License, which permits unrestricted use, distribution, and reproduction in any medium, provided the original work is properly cited.

Along with the fast development of mobile communication technologies, a large number of high-quality wireless services are required. According to the report of Cisco VNI Global Mobile Data Traffic Forecast 2017, global mobile data traffic will increase nearly sevenfold from 2016 to 2021, and mobile network connection speeds will increase threefold by 2021. There is a big gap between the future requirements of wireless services and current communications technologies, even using 4G/5G technique. How to design intelligent algorithms/schemes to make full use of the limited wireless resources is the theme of this special issue. As an important discipline, machine learning includes pattern recognition and computational learning theory in artificial intelligence, and algorithms to learn from the past and make predictions in complicated scenarios. It can be used to analyze the previous/current radio conditions and communication paradigms in wireless communications, such as spectrum utilization, channel capacity, power level, antenna configurations, and heterogeneous link properties and help to generate an optimal action to improve the quality of service (QoS).

Recently, some machine learning algorithms have been proposed for wireless sensor networks, cognitive radio networks, bio-inspired networks, machine-to-machine communications, MIMO link adaption, antenna selection, congestion control, etc. Machine learning has been one of the most active research fields due to its great success in a wide range of domains. However, its impact on wireless communications has so far been very limited. The main challenge is how

to formulate the problems in communication systems as a proper machine learning model.

The paper “Multilayer Learning Network for Modulation Classification Assisted with Frequency Offset Cancellation in Satellite to Ground Link” addresses the issue of carrier frequency offset. The frequency offset is canceled using multilayer learning framework, while the same learning framework is also used for modulation classification. The paper “Pedestrian Motion Learning Based Indoor WLAN Localization via Spatial Clustering” proposes a new pedestrian motion learning-based indoor wireless local area network localization approach. This paper achieves satisfactory location-based services without the demand for location calibration or motion sensors. The paper “Distributed Routing Strategy Based on Machine Learning for LEO Satellite Network” focuses on effective and reliable routing for LEO satellite network. Considering the traffic distribution density on the surface of the earth, the extreme learning machine based distributed routing strategy makes routing decision based on traffic prediction. The paper “WiFi Positioning Based on User Orientation Estimation and Smartphone Carrying Position Recognition” proposes a novel WiFi fingerprinting positioning approach considering both user orientations using a variant of principle-component analysis and smartphone carrying positions by employing robust random forest classifier. Experimental results show that the proposed WiFi positioning approach may improve positioning accuracy significantly. The paper “The Parallel Algorithm Based on

Genetic Algorithm for Improving the Performance of Cognitive Radio” focuses on the intercarrier interference (ICI) problem of cognitive radio (CR). In this paper, the machine learning algorithm is used to obtain the optimal interference subcarriers of an unlicensed user. Moreover, the parallel ICI suppression algorithm is designed to improve the calculation speed and meet the practical requirement of CR.

The set of five papers is carefully selected to present the readers with how different machine learning technologies, ranging from classical principal component analysis to multilayer learning networks, find their applications in different areas of wireless communications. In particular, the works presented in this special issue demonstrate machine learning applications across the communication protocol stack, from techniques of digital modulations, cognitive radio, and routing, to applications in positioning and motion learning.

Conflicts of Interest

The authors declare that there are no conflicts of interest regarding the publication of this paper.

Acknowledgments

The guest editors would like to thank all reviewers for their efforts in reviewing manuscripts submitted to this special issue. This special issue is partially supported by the National Natural Science Foundation of China under Grant No. U1733114 and No. 61631017 and the Fundamental Research Funds for the Central Universities under Grant No. 22120180089.

Xin-Lin Huang
Fei Hu
Xiaomin Ma
Ioannis Krikidis
Dejan Vukobratovic

Research Article

WiFi Positioning Based on User Orientation Estimation and Smartphone Carrying Position Recognition

Zhi-An Deng , Zhiyu Qu , Changbo Hou, Weijian Si, and Chunjie Zhang

College of Information and Communication Engineering, Harbin Engineering University, Harbin 150001, China

Correspondence should be addressed to Zhiyu Qu; quzhiyu@hrbeu.edu.cn

Received 28 December 2017; Revised 24 March 2018; Accepted 15 April 2018; Published 27 September 2018

Academic Editor: Xin-Lin Huang

Copyright © 2018 Zhi-An Deng et al. This is an open access article distributed under the Creative Commons Attribution License, which permits unrestricted use, distribution, and reproduction in any medium, provided the original work is properly cited.

Accuracy performance of WiFi fingerprinting positioning systems deteriorates severely when signal attenuations caused by human body are not considered. Previous studies have proposed WiFi fingerprinting positioning based on user orientation using compasses built in smartphones. However, compasses always cannot provide required accuracy of user orientation estimation due to the severe indoor magnetic perturbations. More importantly, we discover that not only user orientations but also smartphone carrying positions may affect signal attenuations caused by human body greatly. Therefore, we propose a novel WiFi fingerprinting positioning approach considering both user orientations and smartphone carrying positions. For user orientation estimation, we deploy Rotation Matrix and Principal Component Analysis (RMPCA) approach. For carrying position recognition, we propose a robust Random Forest classifier based on the developed orientation invariant features. Experimental results show that the proposed WiFi positioning approach may improve positioning accuracy significantly.

1. Introduction

Location awareness [1–5] based on pervasively available devices such as smartphones has received increasing attentions for Internet of Things (IoT) applications. The Global Navigation Satellite Systems (GNSS) [6] have dominated the outdoor positioning solutions. For indoor environments, since the GNSS signal cannot penetrate man-made infrastructures, many indoor positioning technologies, such as ultra-wideband [7] and radio frequency identification [8], have been developed. Most existing indoor positioning solutions with high positioning accuracy require extra hardware and high cost. Because of the large-scale deployment of access points (APs) and pervasively available smartphones with wireless network card installed, WiFi positioning using received signal strength (RSS) has been considered as one of the most popular indoor positioning solutions.

WiFi positioning systems can be divided into model based approach and fingerprinting based approach. The model based approach [9, 10] constructs the function relating RSS with the physical distance between the mobile devices and the AP. If more than three physical distances are obtained, user location estimation can be obtained by deploying a

trilateration method. In contrast, the fingerprinting based approach [11–13] includes two phases: offline phase and online phase. During offline phase, RSS values from available APs are collected at predefined calibration points and stored as fingerprints to generate the so-called radio map. During online phase, the new measured RSS vectors are matched with the prestored fingerprints in the radio map. The user location is ultimately estimated by weighting locations of the matched calibration points [14, 15] or deploying some machine learning based methods [16, 17]. Due to the complex radio propagation environment, it is difficult for model based approach to construct an accurate function to estimate the distance information. As a result, the accuracy performance cannot be guaranteed by the model based approach. Therefore, we deploy WiFi fingerprinting approach in our paper.

For WiFi fingerprinting approach, a key challenge is the RSS radio mismatch [18–20] phenomenon. This phenomenon occurs when radio environments between RSS radio map construction during offline phase and online positioning phase are obviously different and may deteriorate accuracy performance of WiFi fingerprinting positioning greatly. One main reason of radio mismatch is caused by the

neglected user orientations [21]. Users tend to carry smartphones near to their body, which consists of more than 50% water. The human body might block WiFi signal transmission of 2.4 GHz, especially when the body is between an AP and a smartphone [22]. Previous works [23–25] have carried experiments to confirm the substantial RSS variations caused by user orientations. RSS may vary up to 15dBm [21] at a fixed location when the user facing an AP turns around. As a result, for a fingerprinting based approach, the mismatch of user orientations between offline training phase and online positioning phase may degrade the positioning accuracy greatly.

In order to solve the user orientation mismatch problem, in [26] a user orientation based fingerprinting positioning approach has been proposed. A digital compass built in a smartphone is utilized to detect the user orientation. During offline phase, the user orientation information is also added to enhance the radio map. During online phase, based on the estimated user orientation information, new measured RSS vector samples are only compared with the selected fingerprints sharing a similar user orientation. Similar approaches have been proposed in [27, 28], in which the radio map is extended with user orientation information. However, two problems still need to be solved to enhance the reliability and applicability of fingerprinting based positioning. Firstly, for indoor environments, Earth's magnetic field exploited by digital compass is always noisy and severely perturbed by man-made infrastructures, rendering the user orientation estimations using compasses unavailable. Secondly, we discover that not only user orientations but also smartphone carrying positions may affect RSS greatly due to the different human body attenuation schemes. The impact of different carrying positions on RSS patterns is not considered by previous works, which always assume that the smartphones are held in hand in front of users. However, for daily uses of a smartphone, other carrying positions [29, 30] such as in the trouser pocket or near to ear during phone calls are also widely deployed.

This paper proposes a novel WiFi fingerprinting positioning approach based on user orientation estimation and smartphone carrying position recognition. To the best of our knowledge, our research is the first to consider impacts of user orientation and smartphone carrying position information on RSS patterns simultaneously. Both the user orientation and the smartphone carrying position information are added into the radio map. For user orientation estimation, rather than deploy noisy digital compasses, we deploy our previous proposed Rotation Matrix and Principal Component Analysis (RMPCA) approach [31]. The basic principle is to exploit the principal component of accelerations in the horizontal plane, which is assumed to be parallel with user walking direction. For smartphone carrying position recognition, we investigate the four most classical positions [32], including being held in hand in front of the user (hand-held), put in the trouser pocket (inpocket), near to the right ear during phone calls (phone-call), and in the swinging-hand (swinging-hand). We deploy the Random Forest classifier [33] to recognize the four carrying positions. In order to adapt the changing device orientations, we exploit several orientation invariant features as input features of the classifier.

Experiments in a realistic indoor environment show that the proposed WiFi fingerprinting positioning approach may enhance reliability and applicability significantly. In summary, our work makes the main contributions as follows:

(i) We propose a novel WiFi fingerprinting approach considering both user orientations and smartphone carrying positions.

(ii) We discover that not only user orientations but also smartphone carrying positions may affect RSS patterns greatly.

(iii) We propose a robust carrying position recognition classifier by exploiting several orientation invariant features.

(iv) We report the evaluation of the proposed fingerprinting approach based on extensive experimental samples and compare it with existing approaches.

The remainder of this paper is structured as follows. We present an overview of the proposed WiFi fingerprinting positioning in the following section. In Section 3, we propose a robust carrying position classifier. Section 4 describes the user orientation estimation algorithm using RMPCA approach. Section 5 firstly introduces the impact of user orientations and carrying positions on RSS and then presents the proposed user orientation and carrying position based fingerprinting approach. The experimental results are reported and analyzed in detail in Section 6. In the last section, we give a conclusion and our future works.

2. Overview of the Proposed WiFi Fingerprinting Positioning Approach

Figure 1 presents an overview of the proposed WiFi fingerprinting positioning approach based on user orientation estimation and carrying position recognition. The approach is divided into offline phase and online phase. During offline phase, RSS data at predefined calibration points are collected at eight orientations equally distributed in a circle with four investigated different carrying positions, respectively. As a result, an enhanced radio map, whose fingerprints are labeled with both user orientations and carrying positions, is constructed.

During online phase, we deploy a robust Random Forest based classifier to recognize the smartphone carrying positions. The classifier exploits orientation invariant features generated by acceleration signals as input features. Furthermore, we develop RMPCA based user orientation estimation upon a continuous device attitude tracking. Using the estimated user orientations and recognized carrying positions, we select the fingerprints with similar orientation and the same carrying position, instead of all the fingerprints in the enhanced radio map. Finally, a pattern matching algorithm based on maximum likelihood [22] is used for ultimate location estimation.

3. Robust Smartphone Carrying Position Recognition

For daily uses of smartphones, it is more applicable to assume an unfixd carrying position. For example, it is more common for male users to put the smartphones in their trouser pockets

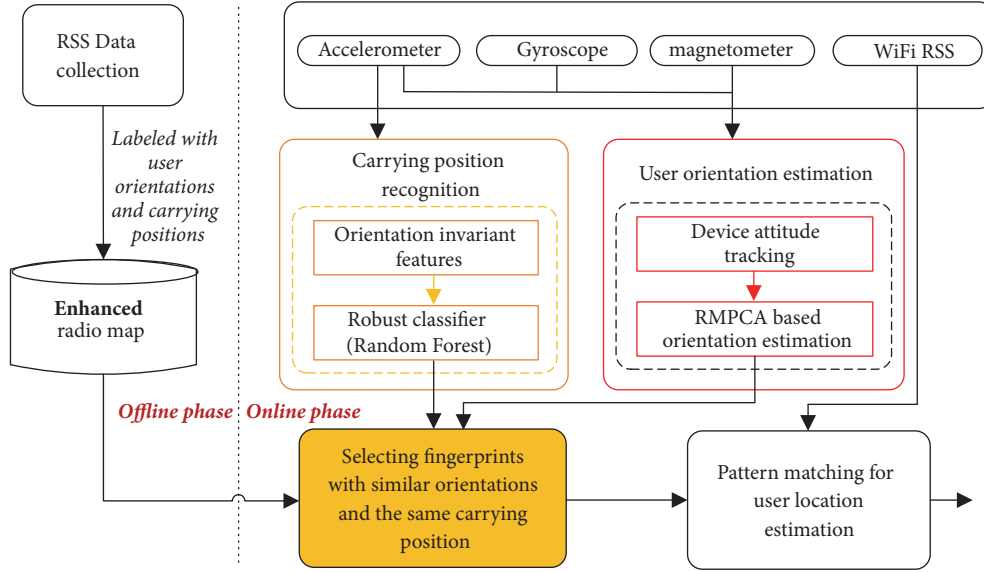


FIGURE 1: Overview of the proposed WiFi fingerprinting positioning approach.

[29]. Different RSS values will be collected with different carrying positions, even in a fixed location with the same user orientation, as will be seen later in Section 5.1. Therefore, we develop a smartphone carrying position recognition method to detect the device carrying position before pattern matching of fingerprinting based approach. For simplicity, we only investigate the four most widely used carrying positions: hand-held, in-pocket, swinging-hand, and phone call.

As previous works [34, 35] suggested, acceleration signals with different device carrying positions show different patterns. Previous classifiers are always founded on relatively fixed and controlled device orientations and deploy normal time domain features [34] for carrying position classifier. The statistics of raw acceleration signal samples over a sliding window, including maximum, minimum, mean, medium, and variance, are computed and deployed as input features to train the carrying position classifier. However, the device orientations may vary for different users due to different user habits. For the same user, the device orientation may also change with the user walking and the other body locomotion. If the device orientations are not fixed, the three-dimensional acceleration signals may vary a lot with unconstrained device orientations at a fixed carrying position. As a result, classification accuracy of previous carrying position classifiers may deteriorate significantly with unconstrained device orientations.

In order to recognize carrying positions with unconstrained device orientations, we propose a robust classifier upon orientation invariant features. Instead of deploying raw three-dimensional accelerations, we exploit three variables, including total magnitude of acceleration M_{Acc} , magnitude of the horizontal acceleration H_{Acc} , and acceleration in the gravity direction G_{Acc} ,

$$M_{Acc} = |\mathbf{Acc}|_2 = \sqrt{Acc_x^2 + Acc_y^2 + Acc_z^2} \quad (1)$$

$$H_{Acc} = |\mathbf{Acc} - (\mathbf{Acc} \cdot \mathbf{g}_{normal}) \mathbf{g}_{normal}|_2 \quad (2)$$

$$G_{Acc} = |(\mathbf{Acc} \cdot \mathbf{g}_{normal}) \mathbf{g}_{normal}|_2 \quad (3)$$

where $\mathbf{Acc} = [Acc_x \ Acc_y \ Acc_z]^T$ is the raw acceleration signal, $|\cdot|_2$ is the 2-norm operator, and \mathbf{g}_{normal} is related gravity vector with normalized value. The gravity vector can be obtained by transforming standard gravity vector using tracked quaternion vector as in (4). These variables show distinct patterns at different carrying positions. Compared with raw acceleration signals, these variables remain relatively stable when the carrying positions are the same, regardless of changing device orientations.

The classifier design includes three stages: data preprocessing, feature extraction, classifier training, and testing. Firstly, we collect raw acceleration signal samples from an accelerometer continuously and split them into segments by a sliding window [34]. Size of the window is two seconds and with one second overlap between neighboring windows. Then, we compute three-orientation invariant variable samples over each window. After data preprocessing, we exploit the statistics of the three variables as input features of carrying positioning classifier, including maximum, minimum, mean, medium, and variance. The input features are all useful to distinguish different carrying positions. For example, because of the higher locomotion intensity of leg than the upper user body, maximum values of H_{Acc} for in-pocket are always significantly larger than those of phone-call positions. Variance values of M_{Acc} of the phone-call positions are always significantly smaller than those of in-pocket positions. More importantly, these input features are insensitive to device orientations and almost independent with device orientations.

After feature extraction, we deploy Random Forest as the classifier, which performs well in many multiclass classification problems. We collect acceleration signals over four thousand sliding windows with four investigated carrying positions. For each position, we sample acceleration signals over all possible device orientations uniformly. We use the widely used 10-fold cross-validation method to train and test the classifier. The extracted features are partitioned into ten parts randomly. Nine of the ten parts are used for training and the rest part for testing. We repeat the whole process for one hundred times by randomly selecting one part for testing. Experimental results show that the robust Radom Forest classifier may improve classification accuracy than compared previous classifiers, as will be seen in Section 6.2.

4. User Orientation Estimation

In order to obtain and represent the absolute user orientation, we firstly define global coordinate system (GCS). GCS consists of three axes X_G , Y_G , and Z_G , which point to east, north, and the sky, respectively. To describe the raw measured signals from inertial sensors, we also define device coordinate system (DCS), which consists of three axes X_{DCS} , Y_{DCS} , and Z_{DCS} . The X_{DCS} and Y_{DCS} axes point right and forward in the front face of smartphone screen, respectively, while Z_{DCS} axis is a standard cross-product of the former two axes. We assume that the initial user orientation is known by other techniques such as landmarks [36]. The user orientation is just the user walking direction, whose value at GCS is defined as the rotation angle from the positive Y_G to user walking direction counterclockwise.

4.1. Device Attitude Tracking. For RMPCA based user orientation approach, it is important to obtain the device attitude continuously. We deploy Extended Kalman Filter (EKF) to model the device attitude tracking. Before designing EKF, we describe device attitude by quaternion vector as given,

$$\mathbf{h}^{DCS}(t) = (\mathbf{C}_{GCS}^{DCS}(\mathbf{q}(t)))^T \mathbf{h}^{GCS}(t) \quad (4)$$

where $\mathbf{C}_{GCS}^{DCS}(\mathbf{q}(t))$ is the rotation matrix from DCS to GCS, $\mathbf{h}^{GCS}(t)$ and $\mathbf{h}^{DCS}(t)$ are the vectors represented at GCS and DCS, and argument t represents the time, which will be omitted in the following equations, rotation matrix can be given as

$$\mathbf{C}_{GCS}^{DCS}(\mathbf{q}) = \begin{bmatrix} q_0^2 + q_1^2 - q_2^2 - q_3^2 & 2(q_1q_2 - q_0q_3) & 2(q_1q_3 + q_0q_2) \\ 2(q_1q_2 + q_0q_3) & q_0^2 - q_1^2 + q_2^2 - q_3^2 & 2(q_2q_3 - q_0q_1) \\ 2(q_1q_3 - q_0q_2) & 2(q_0q_1 + q_2q_3) & q_0^2 - q_1^2 - q_2^2 + q_3^2 \end{bmatrix} \quad (5)$$

where $\mathbf{q} = [q_0 \ q_1 \ q_2 \ q_3]^T$ is the quaternion vector with normalized magnitude.

Secondly, following the kinematic law of rigid body [37], the discrete time evolution model of rotation quaternion vector is given as follows:

$$\begin{aligned} \mathbf{q}_{k+1} &= \exp(0.5 \times \Omega(\mathbf{w}_k T_s)) \mathbf{q}_k \\ &= \left(\mathbf{I} \cos(0.5 \times \Delta\theta_k) + \frac{\Omega(\mathbf{w}_k T_s) \sin(0.5 \times \Delta\theta_k)}{\Delta\theta_k} \right) \mathbf{q}_k \end{aligned} \quad (6)$$

where T_s is the time interval, k and $k+1$ represent time instants kT_s and $(k+1)T_s$, \mathbf{q}_k and \mathbf{q}_{k+1} are the related time evolution quaternion vectors, $\mathbf{w}_k = [w_k^x \ w_k^y \ w_k^z]^T$ is three-dimensional angular velocity at DCS, \mathbf{I} is a 3×3 identity matrix, $\Delta\theta_k = T_s \sqrt{(w_k^x)^2 + (w_k^y)^2 + (w_k^z)^2}$, and $\Omega(\mathbf{w}_k T_s)$ is given by

$$\Omega(\mathbf{w}_k T_s) = T_s \begin{bmatrix} 0 & -w_k^x & -w_k^y & -w_k^z \\ w_k^x & 0 & w_k^z & -w_k^y \\ w_k^y & -w_k^z & 0 & w_k^x \\ w_k^z & w_k^y & -w_k^x & 0 \end{bmatrix} \quad (7)$$

The quaternion \mathbf{q}_{k+1} is determined once the initial quaternion vector \mathbf{q}_0 is known. Therefore, state model of EKF is given by

$$\mathbf{q}_{k+1} = F_k \mathbf{q}_k + \mathbf{w}_k^q \quad (8)$$

where the state transition matrix $F_k = \exp(0.5 * \Omega(\mathbf{w}_k T_s))$ and

$$\mathbf{w}_k^q = \Xi_k \mathbf{w}_k^{gyro} = -\frac{T_s}{2} \begin{bmatrix} [\mathbf{e}_k \times] + q_0^k \mathbf{I} \\ -\mathbf{e}_k^T \end{bmatrix} \mathbf{w}_k^{gyro} \quad (9)$$

$\mathbf{q}_k = [q_0^k \ q_1^k \ q_2^k \ q_3^k]^T$ is the rotation quaternion vector at time instants kT_s with vector part $\mathbf{e}_k = [q_1^k \ q_2^k \ q_3^k]^T$, \mathbf{w}_k^{gyro} is the Gaussian measurement noise variable of angular velocity, and $[\mathbf{e}_k \times]$ is a standard vector cross-product operator.

The measurement model of EKF is given by

$$\begin{aligned} \mathbf{z}_{k+1} &= \begin{bmatrix} \mathbf{a}_{k+1} \\ \mathbf{m}_{k+1} \end{bmatrix} = \phi(\mathbf{q}_{k+1}) + \mathbf{v}_{k+1} \\ &= \begin{bmatrix} (\mathbf{C}_{GCS}^{DCS}(\mathbf{q}_{k+1}))^T & \mathbf{0} \\ \mathbf{0} & (\mathbf{C}_{GCS}^{DCS}(\mathbf{q}_{k+1}))^T \end{bmatrix} \begin{bmatrix} \mathbf{g}_0 \\ \mathbf{h}_0 \end{bmatrix} \\ &\quad + \begin{bmatrix} \mathbf{v}_{k+1}^a \\ \mathbf{v}_{k+1}^m \end{bmatrix} \end{aligned} \quad (10)$$

where \mathbf{a}_{k+1} and \mathbf{m}_{k+1} are the raw measured acceleration and magnetic vectors at DCS, respectively; \mathbf{v}_{k+1}^a and \mathbf{v}_{k+1}^m are the related measurement noise variables; \mathbf{g}_0 and \mathbf{h}_0 are the local gravity and magnetic vectors at GCS, respectively. The measurement noise covariance matrix \mathbf{R}_{k+1} is given by

$$\mathbf{R}_{k+1} = \begin{bmatrix} \mathbf{R}_{k+1}^a & \mathbf{0} \\ \mathbf{0} & \mathbf{R}_{k+1}^m \end{bmatrix} = \begin{bmatrix} R \sigma_a^2 \mathbf{I}_3 & \mathbf{0} \\ \mathbf{0} & R \sigma_m^2 \mathbf{I}_3 \end{bmatrix} \quad (11)$$

where ${}^R\sigma_a^2$ and ${}^R\sigma_m^2$ are set adaptively as follows:

$${}^R\sigma_a^2 = \begin{cases} \sigma_a^2, & \|\mathbf{a}_{k+1}\|_2 - \|\mathbf{g}_0\|_2 < \varepsilon_{a1} \cap \text{var}(\|\mathbf{a}_{k+1-Na/2}\|_2 : \|\mathbf{a}_{k+1+Na/2}\|_2) < \varepsilon_{a2} \\ \infty, & \text{otherwise} \end{cases} \quad (12)$$

$${}^R\sigma_m^2 = \begin{cases} \sigma_m^2, & \|\mathbf{m}_{k+1}\|_2 - \|\mathbf{h}_0\|_2 < \varepsilon_{m1} \cap \text{var}(\|\mathbf{m}_{k+1-Nm/2}\|_2 : \|\mathbf{m}_{k+1+Nm/2}\|_2) < \varepsilon_{m2} \\ \infty, & \text{otherwise} \end{cases} \quad (13)$$

where ε_{a1} is the allowed maximum difference between magnitude of new measured acceleration signal and that of the local gravity vector, $\text{var}(\cdot)$ calculates the variance of signals within a centered window, ε_{a2} is the allowed maximum variance of N_a acceleration signals, ε_{m1} is the allowed maximum difference between magnitude of new measured magnetic signal and that of the local magnetic signal, and ε_{m2} is the allowed maximum variance of N_m magnetic signals.

Based on the state model in (8) and the measurement model in (10), the state vector \mathbf{q}_{k+1} can be iteratively updated by EKF model.

4.2. RMPCA Based User Orientation Estimation. Many works [38] assume that the user orientation is the same as the device forward direction or the angle difference between them is fixed. Therefore, they can directly estimate the user orientation using the device attitude tracking model described in Section 4.1. However, the angle difference between user orientation and device forward direction always varies rapidly with highly dynamic body locomotion, rendering attitude estimation inapplicable for user orientation estimation. Therefore, we deploy RMPCA approach [31] for user orientation estimation. During pedestrian walking period, we assume that the user orientation is just the walking direction. The basic principle of RMPCA is that walking direction is parallel to the principal component of the acceleration signals in the horizontal plane, which dominates most of the horizontal acceleration signal energy.

In detail, RMPCA firstly transforms all raw measured RSS signals during a walking step at DCS into GCS, as follows:

$$\mathbf{a}_{GCS}^i = \mathbf{C}_{GCS}^{DCS}(\mathbf{q}) \mathbf{a}_{DCS}^i, \quad i = 1, \dots, N_{step} \quad (14)$$

where $\mathbf{a}_{GCS}^i = [\mathbf{a}_{GCS}^i(x) \ \mathbf{a}_{GCS}^i(y) \ \mathbf{a}_{GCS}^i(z)]^T$ is the i -th acceleration signal represented at GCS, N_{step} is the number of acceleration signals within the walking step, and \mathbf{q} is the tracked quaternion vector. Each walking step is detected by a widely used peak detection algorithm [39], which relates the heel strike of each step to an acceleration peak value. The acceleration signals in the horizontal plane are in fact the former two acceleration components of \mathbf{a}_{GCS}^i . Then, we perform PCA over horizontal acceleration signals within a walking step to extract the walking direction $\mathbf{WD}_{global} =$

$[\mathbf{WD}_{global}^x \ \mathbf{WD}_{global}^y]^T$. The user orientation O_{user} can be estimated as follows:

$$O_{user} = \arctan\left(\frac{\mathbf{WD}_{global}^y}{\mathbf{WD}_{global}^x}\right) - \frac{\pi}{2} \quad (15)$$

5. Proposed WiFi Fingerprinting Positioning Approach

This section firstly describes the impact of user orientations and carrying positions on RSS, which may directly indicate the motivation of the proposed approach. Then, we describe the proposed fingerprinting approach based on an enhanced radio map considering both user orientations and carrying positions. The user location is ultimately estimated by a maximum likelihood based pattern matching algorithm.

5.1. Impact of User Orientations and Carrying Positions on RSS.

We have carried four experiments to evaluate the impact of user orientations and carrying positions on RSS: line-of-sight (LOS) environment near to AP, LOS environment far away from AP, none-line-of-sight (NLOS) environment near to AP, and NLOS environment far away from AP. We program a smartphone to collect RSS readings every 500 milliseconds from an AP with a total 200 samples for each fixed user orientation and carrying position. The experimental user rotates its orientation by an interval of 45 degrees for a total number of eight orientations. For near and far environments, the distances between AP and user are four and twelve meters, respectively. For user orientation of 90 degrees and 180 degrees, the user is faced with and points away from the AP, respectively.

Figure 2 shows the mean RSS of different user orientations with four carrying positions under the LOS environment near to AP. For hand-held position, RSS values of the user just facing to AP or with the adjacent orientations are greatly larger than those of back toward AP. In particular, compared with user orientation of 180 degrees (back toward AP), the mean RSS values with user orientation of 90 degrees (facing to AP) increase about 20 dB. This is because a user holding the smartphone in hand may block the LOS WiFi signal totally when he stands between the AP and the smartphone. Similarly, for hand-held position under LOS environment far away from AP, RSS values of the user just faced with AP or with the adjacent orientations are also significantly larger

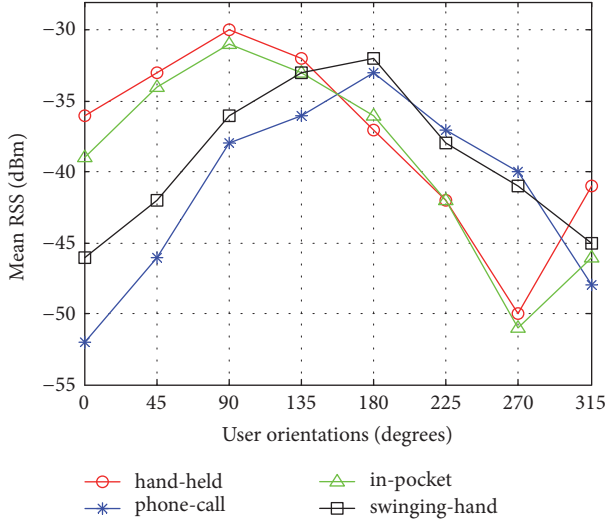


FIGURE 2: Impact of user orientations and carrying positions on mean RSS under the LOS environment near to AP.

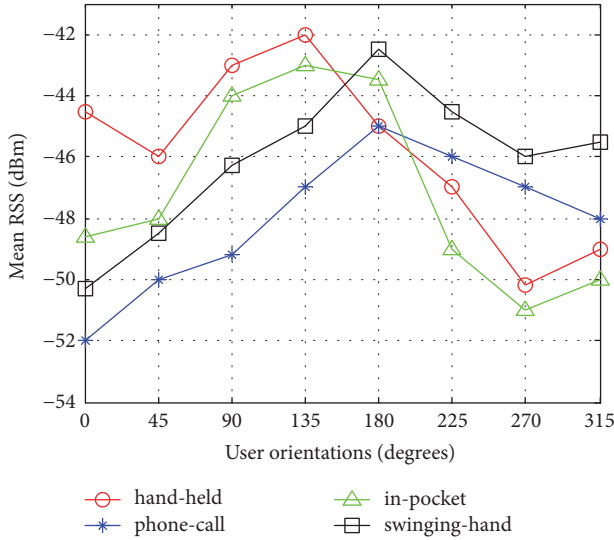


FIGURE 3: Impact of user orientations and carrying positions on mean RSS under the NLOS environment near to AP.

than those of back toward AP, while the increments are a little smaller than those of the near to AP environment.

For the other three carrying positions, there are also significant RSS variations caused by varied user orientations. However, the maximum and minimum RSS values may occur in a very different user orientation. For the phone-call position, the minimum RSS value occurs in the user orientation of 0 degrees instead of 270 degrees for the hand-held position, since the side of user body rather than the whole user body blocks the LOS WiFi signal. As a result, RSS patterns of the same user orientation and different carrying positions are also distinct due to the different signal blocking scheme of user body. It is necessary to add both user orientations and carrying positions to enhance the radio map.

Figure 3 shows the mean RSS of different user orientations with four carrying positions under the NLOS environments

near to AP. We can see that, for hand-held position, RSS values of the user just facing to AP increase about 8 dB than those of back toward AP. Since there is no direct path between AP and the smartphone, the blocking effect of user body under NLOS environment is significantly smaller than that of LOS environment. Furthermore, for NLOS environment far away from AP, the signal blocking effect of user body can be neglected, due to the more complex multipath and NLOS propagation environments. However, for different user orientations and carrying positions, RSS patterns are also different due to different radio propagation environments, though there are no obvious effects of signal absorptions caused by user body. Therefore, in order to avoid introducing the radio mismatch during pattern matching process, both user orientations and carrying positions should be considered in the WiFi fingerprinting approach.

5.2. Enhanced Radio Map Based Location Estimation Using Maximum Likelihood. The proposed WiFi fingerprinting positioning approach consists of two stages: offline enhanced radio map construction and online location estimation. During the offline stage, RSS readings from multiple available APs are collected to build the radio map. The raw RSS value is denoted as $\psi_{i,j}^{o,c}[\tau]$, which indicates RSS from the i -th AP at the j -th calibration point, with user orientation o and carrying position c . For each calibration point, we collect RSS data at eight orientations $O = \{0^\circ, 45^\circ, \dots, 315^\circ\}$ with four different carrying positions $C = \{\text{hand-held, in-pocket, swinging-hand, phone-call}\}$. Then, the enhanced radio map can be represented by ψ as

$$\psi^{o,c}[\tau] = \begin{pmatrix} \psi_{1,1}^{o,c}[\tau] & \psi_{1,2}^{o,c}[\tau] & \cdots & \psi_{1,N}^{o,c}[\tau] \\ \psi_{2,1}^{o,c}[\tau] & \psi_{2,2}^{o,c}[\tau] & \cdots & \psi_{2,N}^{o,c}[\tau] \\ \vdots & \vdots & \ddots & \vdots \\ \psi_{M,1}^{o,c}[\tau] & \psi_{M,2}^{o,c}[\tau] & \cdots & \psi_{M,N}^{o,c}[\tau] \end{pmatrix} \quad (16)$$

where M is the number of APs, N is the number of calibration points, $\tau = 1, \dots, Q$ is time index of temporal RSS samples, and Q is the number of RSS samples. The row vector of ψ represents the RSS data of one AP over N calibration points with Q temporal length. The column vector of ψ represents the M -dimensional RSS samples at the j -th calibration point.

During online stage, a maximum likelihood based pattern matching algorithm is used for location estimation. Maximum likelihood algorithm estimates the likelihood value of new measured RSS observations for all candidate calibration points and weights the points having maximum likelihood as the positioning result. The new measured RSS vectors can be represented as

$$\psi_{\text{new}}^{\bar{o},\bar{c}} = [\psi_{1,\text{new}}^{\bar{o},\bar{c}} \quad \psi_{2,\text{new}}^{\bar{o},\bar{c}} \quad \cdots \quad \psi_{M,\text{new}}^{\bar{o},\bar{c}}]^T \quad (17)$$

where \bar{o} is the estimated user orientation as in (15) and \bar{c} is the recognized carrying position of the four investigated positions. Based on the estimated user orientation

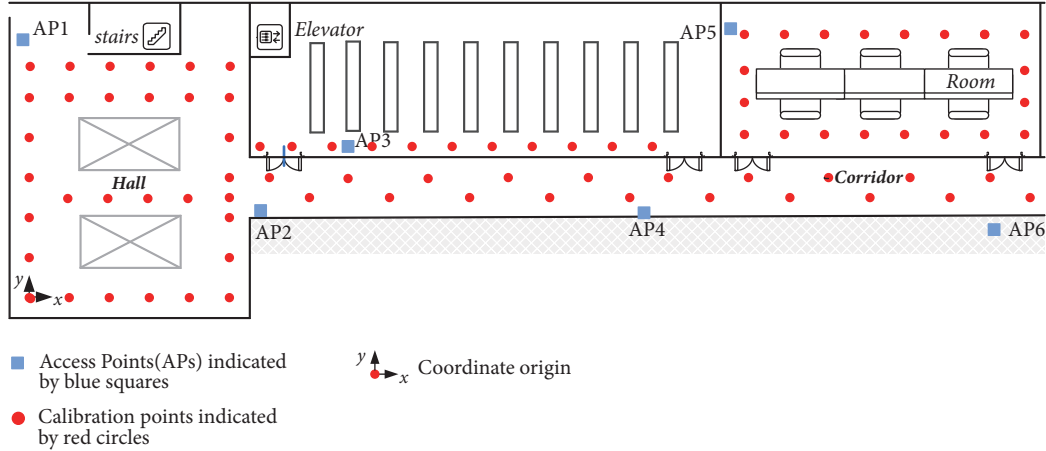


FIGURE 4: Realistic indoor experimental environments for WiFi positioning.

and recognized carrying position, we select the fingerprints with similar orientations and the same positions for pattern matching. Particularly, we obtain the two orientations $o1, o2$ in the set O , which have the smallest absolute differences with the estimated user orientation \bar{o} . The selected radio map can be generated by selecting fingerprints $\psi^{o1, \bar{c}}[\tau]$ and $\psi^{o2, \bar{c}}[\tau]$. For each calibration point, RSS values collected at two orientations $o1, o2$ are merged into one group.

Maximum likelihood algorithm treats the statistical distribution of RSS from one AP at each calibration point as Gaussian distribution. For new RSS vectors, the likelihood at calibration point L_i is calculated by the product of likelihood of all available APs:

$$f(\psi_{\text{new}}^{\bar{o}, \bar{c}} | L_i) = \prod_{j=1}^M f(\psi_{j, \text{new}}^{\bar{o}, \bar{c}} | L_i) \quad (18)$$

where $f(\psi_{j, \text{new}}^{\bar{o}, \bar{c}} | L_i)$ is the likelihood of calibration point L_i for the j -th AP. The Gaussian function is deployed as likelihood function for RSS statistical distribution:

$$f(\psi_{j, \text{new}}^{\bar{o}, \bar{c}} | L_i) = \frac{1}{\sqrt{2\pi}\sigma} \exp\left(-\frac{(\psi_{j, \text{new}}^{\bar{o}, \bar{c}} - \mu_i^j)^2}{2\sigma^2}\right) \quad (19)$$

where μ_i^j is the mean RSS value for the j -th AP at calibration point L_i with carrying position \bar{c} and the user orientations $o1, o2$ and σ is the parameter relating with standard variance. The user location is ultimately estimated by averaging the K calibration points,

$$L_{\text{user}} = \frac{1}{K} \sum_{i=1}^K \tilde{L}_i \quad (20)$$

where \tilde{L}_i are the locations of K calibration points with the maximum likelihood value.

6. Evaluation

6.1. Experimental Setup. We performed experiments in a typical realistic indoor environment, whose size is 27.4 m

\times 11.2 m, as shown in Figure 4. We deploy a Samsung Galaxy S4 smartphone as experimental device with wireless network card, gyroscope, accelerometer, and magnetometer installed. For offline radio map construction, we collect RSS vector samples from all available APs at 82 calibration points with eight user orientations and four investigated carrying positions. The eight user orientations are set along the four coordinate axes directions and four middle directions of them. For each calibration point, 3200 samples are collected with 100 samples per user orientation and carrying position. The calibration points are approximately uniformly distributed in the target environment with a distance of about one meter along the x -axis direction. A total number of eight APs are available, with six APs seen in the target environment and the rest ones in the adjacent area. For testing points, the participant walked along a path with one of the four investigated carrying positions reaching almost all coverage area of the calibration points. Six different walking paths with relatively different user orientations were carried. Each walking path is about one hundred meters long reaching most of the target environment and repeated ten times for each carrying position. The user true locations are obtained by placing multiple tags on the floor and deploying a video to record the walking path. For each experimental run, we assumed that the initial user orientation was known and the inertial sensors were already well calibrated [31].

6.2. Carrying Position Recognition Results. We collect one thousand sliding window samples for each carrying position and a total number of four thousand samples are used to train and test the classifiers. In order to make the classifier more robust to the changing device orientation, we collect acceleration signals under all possible device orientations as uniformly as possible. To avoid introducing noisy acceleration signals, we deploy a five-point average filter to smooth them.

Table 1 compares the classification accuracy performance of the proposed orientation invariant features and normal time domain features. The results show that the proposed robust carrying position classifier shows an average accuracy

TABLE I: Confusion table of Random Forest classifier with orientation invariant and normal features.

(Orientation Invariant/Normal Features)	Hand-Held	Phone-Call	Swinging-Hand	In-Pocket
Hand-Held	0.982/0.904	0.018/0.063	0/0.033	0/0
Phone-Call	0.01/0.064	0.990/0.915	0/0.004	0/0.017
Swinging-Hand	0/0.018	0/0.001	0.986/0.896	0.014/0.085
In-Pocket	0/0	0/0	0.028/0.081	0.972/0.919

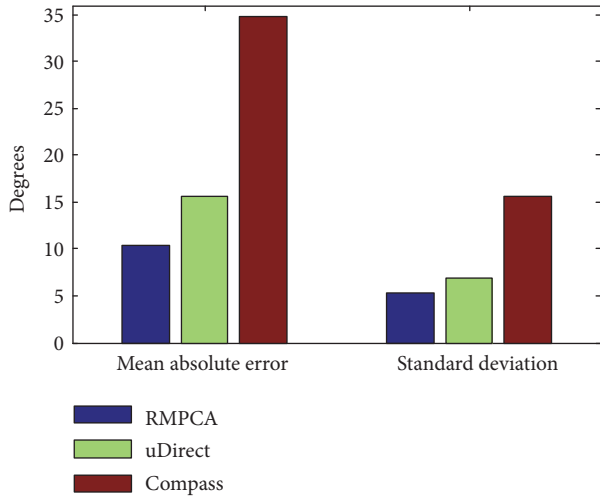


FIGURE 5: Mean absolute user orientation estimation error and the standard deviation comparisons between RMPCA, uDirect, and compass approaches.

reaching 98.5%, which is high enough for recognizing the carrying position accurately. Therefore, the subsequent experiments assume that the used carrying position information is correctly recognized initially. Compared with the traditional normal time domain features, the proposed classifier achieves a significant accuracy improvement from 90.9% to 98.5%. The improvement can be contributed to the higher discrimination and generalization ability of the extracted orientation invariant features. Rather than previous normal time domain features vary greatly with the changing device orientation, the extracted features keep relatively stable. Besides, the probabilities of confusing between swinging-hand and in-pocket pairs, hand-held, and phone-call pairs are higher than the other pairs, since the acceleration patterns within these pairs are more confused than the other pairs, due to their more similar patterns of body locomotion.

6.3. User Orientation Estimation Results. Figure 5 compares mean absolute user orientation estimation error and the standard deviation values between RMPCA, uDirect [40], and compass [26] approaches. The deployed RMPCA approach decreases the mean absolute estimation error by 33.8 percent (5.3 degrees) and 70.2 percent (24.4 degrees) more than those of the compared uDirect and compass approaches, respectively. For standard deviation, RMPCA approach decreases by 22.6 percent (1.6 degrees) and 66.1 percent (10.4 degrees) more than those of the compared uDirect and compass approaches, respectively. Clearly, the

deployed RMPCA approach achieves the best user heading estimation accuracy.

For the uDirect approach, the user orientation during a walking period is extracted at the moment when acceleration signals along the waling direction dominate the accelerations in the horizontal plane. Unfortunately, such a moment is susceptible to noisy acceleration signals. Instead of exploiting some specific acceleration samples by uDirect approach, the RMPCA approach exploits all acceleration samples during a walking period by performing PCA over the horizontal acceleration signals. Therefore, the RMPCA approach is more robust and achieves smaller user orientation estimation error and standard deviation than the uDirect approach. For user orientation using a compass, since the indoor magnetic perturbations are severe and is difficult to be calibrated, the accuracy performance of user orientation is much worse than the two other approaches.

6.4. Location Estimation Results. This section compares the proposed WiFi positioning approaches considering user orientations and carrying positions; WiFi positioning approach based on user orientation estimation using a compass and traditional WiFi positioning approach do not consider these information. We perform traditional WiFi positioning approach by selecting fingerprints with random user orientations and carrying positions to construct the radio map. The pattern matching algorithm deploys the widely used maximum likelihood method. The positioning error is defined as the Euclidean distance between the estimated coordinates per step and the labeled coordinates per step along the true path. Positioning accuracy is mainly evaluated by the accumulative probability distribution of positioning errors.

As seen in Figure 6, accumulative error distribution within 1 m of the proposed approach is 35.1%, while those of approach (compass) and traditional approach are 20.1% and 17.1%, respectively. Accumulative error distribution within 3 m of the proposed approach is 88.9%, while those of approach (compass) and traditional approach are 63.6% and 57.9%, respectively. Table 2 also indicates error reduction of the proposed approach than the other two compared approaches. Compared with approach (compass) and traditional approach, the proposed approach decreases mean positioning errors by 41.7% (1.15 m) and 46.7% (1.41 m), respectively.

Compared with approach (compass) and traditional approach, the proposed approach obtains significant positioning accuracy improvement. This is because the proposed positioning approach may exploit the user orientation and carrying position information to enhance the radio map

TABLE 2: Positioning error (meters) comparisons.

Compared Approaches	Proposed approach	Approach (Compass)	Traditional Approach
Mean error	1.61	2.76	3.02
75 percentile	2.35	3.87	4.42
90 percentile	3.11	5.68	6.05
Standard variance	0.40	0.48	0.53

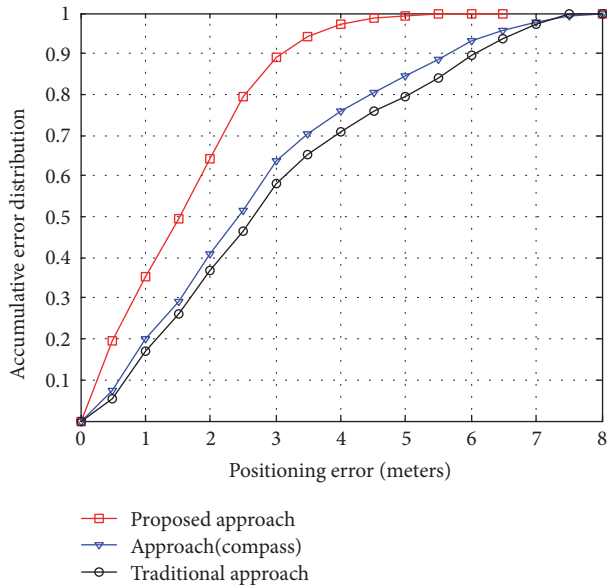


FIGURE 6: Accuracy comparisons between the proposed approach, approach (compass), and traditional approach.

and thus the radio mismatch can be avoided effectively. For approach (compass), user orientation information is estimated by a compass and exploited in the fingerprinting pattern matching. However, the user orientation estimation accuracy is rather poor due to serve indoor magnetic perturbations. Therefore, the selected fingerprints may differ from the right fingerprints with similar orientations greatly. Therefore, the approach (compass) achieves small accuracy improvement than the traditional approach.

7. Conclusions

In this paper, we propose a novel WiFi fingerprinting positioning approach by considering both user orientations and carrying positions. Since the compass incurs large user orientation estimation errors due to indoor magnetic perturbations, we deploy RMPCA approach. For carrying position recognition, we propose a robust Random Forest classifier based on orientation invariant features, which may better adapt the changing device orientations. Under both LOS and NLOS environments, RSS patterns with different user orientations and smartphone carrying positions are distinct from one another. Therefore, the proposed WiFi fingerprinting approach may effectively avoid the radio mismatch during pattern matching. Experimental results show that compared with WiFi fingerprinting positioning approach

only considering user orientation estimation using a compass and the approach considering neither user orientation nor carrying position information, our approach decreases mean positioning errors by 41.7% (1.15 m) and 46.7% (1.41 m), respectively. In our future works, we will further integrate pedestrian dead reckoning approach to improve the positioning performance.

Conflicts of Interest

The authors declare no conflicts of interest.

Authors' Contributions

Zhi-An Deng and Zhiyu Qu proposed the original idea and developed the proposed fingerprinting approach; Changbo Hou developed the user orientation algorithm; Weijian Si analyzed the data and revised the paper; Chunjie Zhang designed the experiments and gave some valuable suggestions.

Acknowledgments

This research is supported by the National Natural Science Foundation of China (Grant nos. 61671168, 61301132, 61300188, and 61301131) and the Fundamental Research Funds for the Central Universities (Grant nos. HEUCF180801 and HEUCFJ180801).

References

- [1] Y. Sun, W. Meng, C. Li, N. Zhao, K. Zhao, and N. Zhang, "Human localization using multi-source heterogeneous data in indoor environments," *IEEE Access*, vol. 5, pp. 812–822, 2017.
- [2] M. Cobos, F. Antonacci, A. Alexandridis, A. Mouchtaris, and B. Lee, "A survey of sound source localization methods in wireless acoustic sensor networks," *Wireless Communications and Mobile Computing*, vol. 2017, 2017.
- [3] X.-L. Huang, J. Wu, W. Li, Z. Zhang, F. Zhu, and M. Wu, "Historical Spectrum Sensing Data Mining for Cognitive Radio Enabled Vehicular Ad-Hoc Networks," *IEEE Transactions on Dependable and Secure Computing*, vol. 13, no. 1, pp. 59–70, 2016.
- [4] M. Zhou, Q. Zhang, K. Xu, Z. Tian, Y. Wang, and W. He, "PRIMAL: Page rank-based indoor mapping and localization using gene-sequenced unlabeled WLAN received signal strength," *Sensors*, vol. 15, no. 10, pp. 24791–24817, 2015.
- [5] X. Huang, J. Wu, Y. Wen, F. Hu, Y. Wang, and T. Jiang, "Rate-Adaptive Feedback with Bayesian Compressive Sensing in Multiuser MIMO Beamforming Systems," *IEEE Transactions on Wireless Communications*, pp. 1-1.

- [6] X. Li, X. Zhang, X. Ren, M. Fritsche, J. Wickert, and H. Schuh, "Precise positioning with current multi-constellation Global Navigation Satellite Systems: GPS, GLONASS, Galileo and BeiDou," *Scientific Reports*, vol. 5, p. 8328, 2015.
- [7] S. Gezici, Z. Tian, G. B. Giannakis et al., "Localization via ultra-wideband radios: a look at positioning aspects of future sensor networks," *IEEE Signal Processing Magazine*, vol. 22, no. 4, pp. 70–84, 2005.
- [8] J. Xiao, Z. Zhou, Y. Yi, and L. M. Ni, "A survey on wireless indoor localization from the device perspective," *ACM Computing Surveys*, vol. 49, no. 2, pp. 1–31, 2016.
- [9] S. He and S.-H. G. Chan, "Wi-Fi fingerprint-based indoor positioning: recent advances and comparisons," *IEEE Communications Surveys & Tutorials*, vol. 18, no. 1, pp. 466–490, 2016.
- [10] G. Caso and L. De Nardis, "Virtual and Oriented WiFi Fingerprinting Indoor Positioning based on Multi-Wall Multi-Floor Propagation Models," *Mobile Networks and Applications*, vol. 22, no. 5, pp. 825–833, 2017.
- [11] M. Zhou, F. Qiu, K. Xu, Z. Tian, and H. Wu, "Error bound analysis of indoor Wi-Fi location fingerprint based positioning for intelligent Access Point optimization via Fisher information," *Computer Communications*, vol. 86, pp. 57–74, 2016.
- [12] L. Ma and Y. Xu, "Received signal strength recovery in a green WLAN indoor positioning system using singular value Thresholding," *Sensors*, vol. 15, no. 1, pp. 1292–1311, 2015.
- [13] Z.-A. Deng, Y.-B. Xu, and L. Ma, "Indoor positioning via nonlinear discriminative feature extraction in wireless local area network," *Computer Communications*, vol. 35, no. 6, pp. 738–747, 2012.
- [14] P. Bahl, V. Padmanabhan, and A. Balachandran, "Enhancements to the RADAR user location and tracking system," *Microsoft Research*, vol. 2, no. MSR-TR-2000-12, pp. 775–784, 2000.
- [15] M. Youssef and A. Agrawala, "The Horus WLAN location determination system," in *Proceedings of the 3rd International Conference on Mobile Systems, Applications, and Services (MobiSys '05)*, pp. 205–218, ACM, June 2005.
- [16] S.-H. Fang and T.-N. Lin, "Indoor location system based on discriminant-adaptive neural network in IEEE 802.11 environments," *IEEE Transactions on Neural Networks and Learning Systems*, vol. 19, no. 11, pp. 1973–1978, 2008.
- [17] Y. Xu, Z. Deng, L. Ma, W. Meng, and C. Li, "Signal perturbation based support vector regression for Wi-Fi positioning," in *Proceedings of the 2012 IEEE Wireless Communications and Networking Conference, WCNC 2012*, pp. 3123–3127, France, April 2012.
- [18] S. Han, Z. Gong, W. Meng, C. Li, D. Zhang, and W. Tang, "Automatic Precision Control Positioning for Wireless Sensor Network," *IEEE Sensors Journal*, vol. 16, no. 7, pp. 2140–2150, 2016.
- [19] L. Kanaris, A. Kokkinis, A. Liotta, and S. Stavrou, "Fusing bluetooth beacon data with Wi-Fi radiomaps for improved indoor localization," *Sensors*, vol. 17, no. 4, 2017.
- [20] Z. A. Deng, Y. Bin Xu, and L. Ma, "Joint Access Point Selection and Local Discriminant Embedding for Energy Efficient and Accurate Wi-Fi Positioning," *KSII Transactions on Internet and Information Systems*, vol. 6, no. 3, pp. 794–814, 2012.
- [21] K. Kaemarungsi and P. Krishnamurthy, "Properties of indoor received signal strength for WLAN location fingerprinting," in *Proceedings of the 1st Annual International Conference on Mobile and Ubiquitous Systems: Networking and Services (MOBIQUITOUS '04)*, pp. 14–23, August 2004.
- [22] S.-H. Fang, C.-H. Wang, and Y. Tsao, "Compensating for Orientation Mismatch in Robust Wi-Fi Localization Using Histogram Equalization," *IEEE Transactions on Vehicular Technology*, vol. 64, no. 11, pp. 5210–5220, 2015.
- [23] Z. Zhang, X. Zhou, W. Zhang et al., "I am the antenna: accurate outdoor AP location using smartphones," in *Proceedings of the 17th Annual International Conference on Mobile Computing and Networking (MobiCom '11)*, pp. 109–120, September 2011.
- [24] F. Della Rosa, M. Pelosi, and J. Nurmi, "Human-Induced Effects on RSS Ranging Measurements for Cooperative Positioning," *International Journal of Navigation and Observation*, vol. 2012, Article ID 959140, 13 pages, 2012.
- [25] F. Della Rosa, L. Xu, J. Nurmi, M. Pelosi, C. Laoudias, and A. Terrezza, "Hand-grip and body-loss impact on RSS measurements for localization of mass market devices," in *Proceedings of the 2011 International Conference on Localization and GNSS, ICL-GNSS 2011*, pp. 58–63, Finland, June 2011.
- [26] T. King, S. Kopf, T. Haenselmann, C. Lubberger, and W. Effelsberg, "COMPASS: A probabilistic indoor positioning system based on 802.11 and digital compasses," in *Proceedings of the WiNTECH 2006 - First ACM International Workshop on Wireless Network Testbeds, Experimental Evaluation and Characterization*, pp. 34–40, USA, September 2006.
- [27] D. Sánchez, J. M. Quinteiro, P. Hernández-Morera, and E. Martel-Jordán, "Using data mining and fingerprinting extension with device orientation information for WLAN efficient indoor location estimation," in *Proceedings of the 2012 IEEE 8th International Conference on Wireless and Mobile Computing, Networking and Communications, WiMob 2012*, pp. 77–83, Spain, October 2012.
- [28] A. Papapostolou and H. Chaouchi, "Orientation-based radio map extensions for improving positioning system accuracy," in *Proceedings of the International Wireless Communications and Mobile Computing Conference*, pp. 947–951, ACM, June 2009.
- [29] F. Ichikawa, J. Chipchase, and R. Grignani, "Where's the phone? A study of mobile phone location in public spaces," in *Proceedings of the 2nd International Conference on Mobile Technology, Applications and Systems*, pp. 1–8, IEEE, November 2005.
- [30] E. M. Diaz, A. L. M. Gonzalez, and F. De Ponte Müller, "Standalone inertial pocket navigation system," in *Proceedings of the 2014 IEEE/ION Position, Location and Navigation Symposium, PLANS 2014*, pp. 241–251, USA, May 2014.
- [31] Z.-A. Deng, G. Wang, Y. Hu, and D. Wu, "Heading estimation for indoor pedestrian navigation using a smartphone in the pocket," *Sensors*, vol. 15, no. 9, pp. 21518–21536, 2015.
- [32] M. Kourogi and T. Kurata, "A method of pedestrian dead reckoning for smartphones using frequency domain analysis on patterns of acceleration and angular velocity," in *Proceedings of the IEEE/ION Position, Location and Navigation Symposium (PLANS '14)*, vol. 19, pp. 164–168, IEEE, May 2014.
- [33] L. Breiman, "Random forests," *Machine Learning*, vol. 45, no. 1, pp. 5–32, 2001.
- [34] M. Shoaib, S. Bosch, O. Durmaz Incel, H. Scholten, and P. J. M. Havinga, "Fusion of smartphone motion sensors for physical activity recognition," *Sensors*, vol. 14, no. 6, pp. 10146–10176, 2014.
- [35] Q. Tian, Z. Salcic, K. I.-K. Wang, and Y. Pan, "A Multi-Mode Dead Reckoning System for Pedestrian Tracking Using Smartphones," *IEEE Sensors Journal*, vol. 16, no. 7, pp. 2079–2093, 2016.
- [36] Z. Deng, W. Si, Z. Qu, X. Liu, and Z. Na, "Heading estimation fusing inertial sensors and landmarks for indoor navigation

- using a smartphone in the pocket,” *EURASIP Journal on Wireless Communications and Networking*, vol. 2017, no. 1, 2017.
- [37] J. C. K. Chou, “Quaternion kinematic and dynamic differential equations,” *IEEE Transactions on Robotics and Automation*, vol. 8, no. 1, pp. 53–64, 1992.
- [38] Y. Li, J. Georgy, X. Niu, Q. Li, and N. El-Sheimy, “Autonomous calibration of MEMS gyros in consumer portable devices,” *IEEE Sensors Journal*, vol. 15, no. 7, pp. 4062–4072, 2015.
- [39] A. Brajdic and R. Harle, “Walk detection and step counting on unconstrained smartphones,” in *Proceedings of the ACM International Joint Conference on Pervasive and Ubiquitous Computing (UbiComp ’13)*, pp. 225–234, September 2013.
- [40] S. A. Hoseinitabatabaei, A. Gluhak, R. Tafazolli, and W. Headley, “Design, realization, and evaluation of uDirect-An approach for pervasive observation of user facing direction on mobile phones,” *IEEE Transactions on Mobile Computing*, vol. 13, no. 9, pp. 1981–1994, 2014.

Research Article

Distributed Routing Strategy Based on Machine Learning for LEO Satellite Network

Zhenyu Na ¹, Zheng Pan,¹ Xin Liu ², Zhian Deng ³, Zihe Gao,⁴ and Qing Guo ⁴

¹School of Information Science and Technology, Dalian Maritime University, Dalian 116026, China

²School of Information and Communication Engineering, Dalian University of Technology, Dalian 116024, China

³College of Information and Communication Engineering, Harbin Engineering University, Harbin 150001, China

⁴Communication Research Center, Harbin Institute of Technology, Harbin 150001, China

Correspondence should be addressed to Xin Liu; liuxinstar1984@dlut.edu.cn

Received 31 October 2017; Revised 24 January 2018; Accepted 7 February 2018; Published 14 June 2018

Academic Editor: Fei Hu

Copyright © 2018 Zhenyu Na et al. This is an open access article distributed under the Creative Commons Attribution License, which permits unrestricted use, distribution, and reproduction in any medium, provided the original work is properly cited.

As the indispensable supplement of terrestrial communications, Low Earth Orbit (LEO) satellite network is the crucial part in future space-terrestrial integrated networks because of its unique advantages. However, the effective and reliable routing for LEO satellite network is an intractable task due to time-varying topology, frequent link handover, and imbalanced communication load. An Extreme Learning Machine (ELM) based distributed routing (ELMDR) strategy was put forward in this paper. Considering the traffic distribution density on the surface of the earth, ELMDR strategy makes routing decision based on traffic prediction. For traffic prediction, ELM, which is a fast and efficient machine learning algorithm, is adopted to forecast the traffic at satellite node. For the routing decision, mobile agents (MAs) are introduced to simultaneously and independently search for LEO satellite network and determine routing information. Simulation results demonstrate that, in comparison to the conventional Ant Colony Optimization (ACO) algorithm, ELMDR not only sufficiently uses underutilized link, but also reduces delay.

1. Introduction

In last decade, with the widespread applications of high-speed mobile Internet and the rapid advances of space technologies, satellite network has become the inseparable component of global mobile communications. Because of global coverage, satellite network can provide reliable communication services to the regions without terrestrial networks. Since Low Earth Orbit (LEO) satellite has the relatively low orbit altitude, it has the advantages of low transmission delay and link loss. The invulnerability is another feature of LEO satellite network due to the following reasons. On the one hand, the networking of LEO satellites is more flexible. On the other hand, inter-satellite links make the communication between satellites independent of the terrestrial infrastructure. Therefore, LEO satellite communications draw much attention of academia and industrial world [1–4].

However, the global coverage of LEO satellite network needs tens to hundreds of satellites because of the relatively small coverage. Moreover, LEO satellite network has the

characteristics of short orbit period, highly dynamic topology, and frequent link handovers. In addition, the advanced physical-layer techniques oriented to the Fifth Generation (5G) mobile communications greatly enhance the data transmission rate leading to an explosive growth of network traffic [5]. In such a LEO satellite network, how to design a reliable, efficient, and robust routing strategy is the primary task to guarantee reliable data transmission [6, 7].

Some routing strategies for LEO satellite network were put forward at home and abroad. When it comes to early routing strategies, their focus mainly concentrates on connection-oriented routing [8–10]. Due to their offline computation resulting in the lagged routing information, they were quickly replaced by dynamic and non-connection-oriented routing strategies [11]. Many strategies were proposed [12–14], which mainly focus on the so-called logical address. These strategies are ultimately converted into the problem of the shortest path. However, the overload and congestion at satellite nodes on the shortest path are not taken into account by the strategies. To overcome the shortcoming, the balanced-load

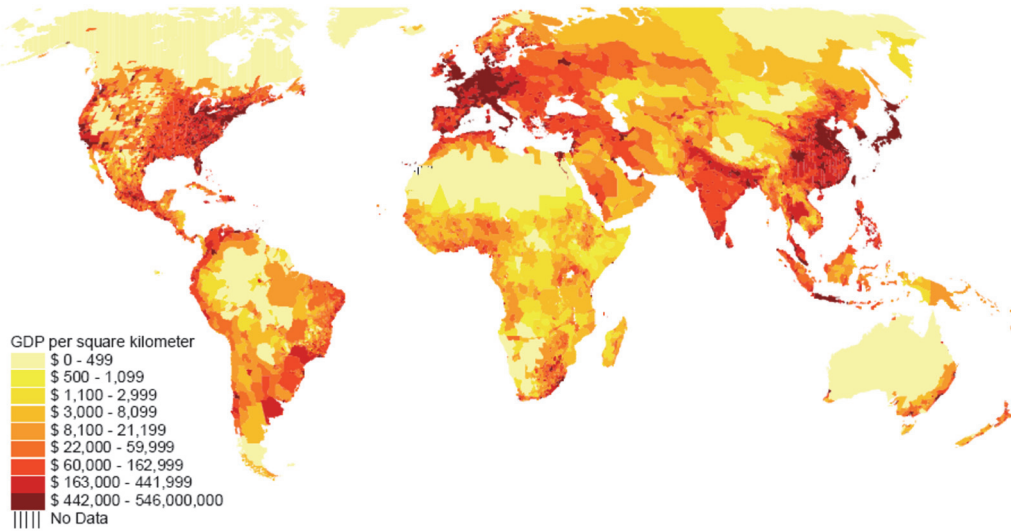


FIGURE 1: GDP density in the world.

and prediction based routing strategies draw researchers' attention.

[15, 16] proposed the routing strategies combined with load balancing. In [15], the authors hold that the overloaded satellite node should be bypassed to relieve network congestion. In [16], the authors utilize multiagent system and physical-layer information to make routing decision and then convert load balancing into a multiobjective optimization problem. However, the combination of multiagent, physical-layer information and multiobjective optimization makes the routing almost impractical for real-time services in long-delay environment. Because prediction can provide the information in the future, some references proposed prediction based routing strategies. In [17], a time series analysis based routing scheme was proposed. Though the prediction method is simple, it suffers from low prediction accuracy. In [18], a routing algorithm based on load balancing and congestion prediction was proposed, in which only the congestion state is predicted, but it results in incomplete routing information.

Considering dynamic network topology, the approaches based on Artificial Intelligence (AI) were put forward [19–26]. Though some traditional Artificial Neural Network (ANN) based strategies take Quality of Service (QoS) into consideration, they are often time-consuming because of complex training process. Another disadvantage is that they only focus on current routing information without considering the future state. At present, machine learning (ML) catches the eyes of the academic world [27, 28] because it can highly improve the performance of algorithms by learning of experience. ML has already been applied to many fields. Similar to traditional ANN, the training process of ML is also time-consuming. The appearance of Extreme Learning Machine (ELM) is a breakthrough to enhance training speed [29]. A distributed routing strategy on the basis of ELM is proposed in this paper. Firstly, ELM is used to predict

upcoming traffic load at satellite nodes. Then, mobile agents (MAs) collect network information to make routing decision using the predicted traffic load. Finally, according to the routing decision, adjacent satellite nodes dynamically adjust traffic load.

2. Traffic Distribution Density and Its Quantification

The traffic distribution density (TDD) on the surface of the earth has a nonnegligible impact on routing performance. Traditionally, most routing strategies only react to the traffic load of satellite node itself. In fact, if the TDD on the surface of the earth below the satellite is considered, a proactive routing decision can be taken in advance to enhance routing performance. There are three factors to influence TDD on the surface of the earth, including two natural factors and one human factor. The first natural factor is the land-sea distribution. Specifically, a satellite over the ocean is often in the state of light load, while a satellite over a city is frequently in the state of heavy load. Another natural factor is relevant to the earth's rotation. Obviously, the regions in day time are heavier in traffic load than the regions in night time. The human factor is often associated with economic level. In general, the developed countries and regions are equipped with the advanced infrastructure. Figure 1 presents the Gross Domestic Product (GDP) density in the world [30]. The imbalance of the worldwide economic development brings about the imbalanced development of telecommunications. In general, the regions with dense population and developed economics are abundant in terrestrial telecommunication infrastructure.

We divide the surface of the earth into several grids, which are quantified according to GDP density. As demonstrated in Figure 2, we use the numbers from 1 to 10 as traffic index to represent the TDD. Both longitude and latitude are divided

training time and ELM can realize universal function approximation [32]. In this paper, the incremental ELM [32] is used to predict upcoming traffic because it is not subject to overfitting. Because LEO satellite runs on its orbit at high speed, its traffic load changes with the location change of subsatellite point. ELM is used to forecast the traffic for the satellite over specific grids below subsatellite point.

3. ELMDR Strategy for LEO Satellite Network

In order to make routing decision, MA is used to collect and exchange path information for LEO satellite network. MA is the distributed and intelligent agent with mobility, which can decide its movement behavior between nodes by itself in a high-efficiency way. MA can be classified into forward MA and backward MA. The former is generated and sent by the source satellite node to explore path information, while the latter is produced by the destination satellite node. Both forward MA and backward MA have a maximum time to live (TTL) which is defined as the hop limits of a MA. If their hops exceed TTL, they are deemed to expire and destroyed directly. The intention of setting TTL is partially to avoid loop and lagging routing information. In addition, satellite node would generate prediction agent to get traffic information to revise a routing preference factor which is used to adjust the traffic from adjacent satellite nodes.

In order to record and update routing information, a data structure is maintained by each satellite node which is comprised of the pheromone matrix T , data-routing table R , delay model D , link queue model L , traffic prediction model P , and local statistical model M . T and R are the functions of a "distance vector", which is not the ordinary concept of distance but the probability representing the path condition. D stands for the expected delay between the current node and each possible destination node. L denotes local traffic information. P records the predicted traffic. Statistical model M maintains the time related information.

The routing strategy of ELMDR is presented as follows.

(1) *Behavior of Forward MA.* For each interval Δt , forward MA expressed as $F_{s \rightarrow d}$ is produced, which is responsible for the collection of nonlocal routing information. $F_{s \rightarrow d}$ has the same priority as the information data and accurately records network state. The traversal time between arbitrary two nodes and the identifiers of all nodes from s to d are recorded in a private memory H . The next node is selected according to the following rule:

$$p_{i,j} = \begin{cases} \frac{1}{M_0 \tau_{ij}} & q < q_1 \\ \frac{1}{\sum_{j \in \mathcal{M}} \tau_{ij}} & q \geq q_1, \end{cases} \quad (1)$$

where p_{ij} is the probability to select the link(i, j); M_0 represents the node set adjacent to node i ; and τ_{ij} means the pheromone on the link(i, j).

Loop routing should be removed from forward MA and an adjacent node is randomly selected as the next hop. If the constraints of $q < q_1$ and $q \geq q_1$ are not included in (1),

after a while, the probability of an optimal path selected based on pheromone distribution would get close to 1 that means path search approaches standstill. In other words, even if the optimal path is congested, subsequent data packets are still transferred along the path regardless of other potential idle paths. Such a case is considered by (1). q is a stochastic number between 0 and 1, while q_1 is a constant between 0 and 1. A smaller q_1 can be empirically selected to stop the search standstill. According to (1), forward MA selects the next node according to either the distribution of pheromone (i.e., when $q \geq q_1$) or random selection probability (i.e., when $q < q_1$). As a result, though the probability to select the optimal path is still high, it is not equal to 1. The use of a small probability q_1 makes some forward MAs explore other potentially optimal paths. When the originally optimal path is getting bad, forward MA can quickly discover the newly optimal path.

(2) *Behavior of Backward MA.* After forward MA $F_{s \rightarrow d}$ gets to node d , it is automatically deleted. In the meantime, the backward MA expressed as $B_{d \rightarrow s}$, which includes all information collected by $F_{s \rightarrow d}$, is generated by the destination node d . $B_{d \rightarrow s}$ goes back to node s along the same path passed by forward MA but from d to s . Carrying routing information, backward MA can quickly return to node s because of its higher priority than information data. All intermediate nodes update their routing tables according to the delay information provided by backward MA. The update rules are given below:

$$\begin{aligned} \tau_{ij}(t+1) &= (1-\rho) \cdot \tau_{ij}(t) + \sum_{b=1}^m \Delta \tau_{ij}^b(t) + \Delta \tau'_{ij}(t) \\ \Delta \tau_{ij}^b(t) &= \begin{cases} \frac{P_h}{d_b} & \text{link } L_{i \rightarrow j} \text{ passed by } B_{d \rightarrow s} \\ 0 & \text{otherwise.} \end{cases} \end{aligned} \quad (2)$$

where ρ is the evaporation factor of pheromone whose value is between 0 and 1; the term of $\sum_{b=1}^m \Delta \tau_{ij}^b(t)$ is the pheromone increment on link(i, j) taken by $B_{d \rightarrow s}$; P_h is the pheromone brought by $B_{d \rightarrow s}$; d_b is the latency on link(i, j); and the term $\Delta \tau'_{ij}(t)$ stands for the pheromone increment given to the agents to find the new optimal path. Specifically, when a new optimal path is discovered, most agents still select the originally optimal path and leave their pheromone. By using the pheromone increment, convergence speed of routing search can be enhanced.

(3) *Data Update.* For each intermediate satellite passed by node k , three actions are taken by backward MA, including to update M , evaluate the quality of path from node k to node d , and update local paths. Referring to the local traffic model M_d , the path from node k to node d is assessed based on traversal time $T_{k \rightarrow d}$. The smaller $T_{k \rightarrow d}$ is, the higher the path weight is. Based on the weight, all paths which use d as the destination node and k as the next hop are strengthened.

μ_d is the mean of $T_{k \rightarrow d}$, while σ_d^2 is the variance of $T_{k \rightarrow d}$. W_d is the optimum traversal time of recent W values of

traversal time experienced by forward MA. They are updated according to the following:

$$\begin{aligned}\mu_d &\leftarrow \mu_d + \eta(T_{k \rightarrow d} - \mu_d) \\ \sigma_d^2 &\leftarrow \sigma_d^2 + \eta[(T_{k \rightarrow d} - \mu_d)^2 - \sigma_d^2] \\ W_d &= T_{k \rightarrow d} \quad (\text{when } T_{k \rightarrow d} < W_d),\end{aligned}\quad (3)$$

where η is weight factor.

After updating M , the path passed by $F_{s \rightarrow d}$ is evaluated according to the following expression:

$$r = c_1 \left(\frac{W_d}{T_{k \rightarrow d}} \right) + c_2 \left(\frac{I_{\text{sup}} - I_{\text{inf}}}{(I_{\text{sup}} - I_{\text{inf}}) + (T_{k \rightarrow d} - I_{\text{inf}})} \right). \quad (4)$$

Here, r is a preference factor. It represents the quality of the path found by forward MA. The aim of evaluation is to update pheromone table and routing table by the preference factor. I_{sup} and I_{inf} are the estimations of the maximum value and the minimum value of μ_d . c_1 and c_2 stand for the weighting factors. r is revised according the predicted traffic. In general, when satellite flies over the region with heavy/light load, the potential node congestion/idleness is reported based on the corresponding large/small traffic index. When the predicted traffic is heavy, it means that satellite runs from the region with light load to the region with heavy load. In this case, the traffic sent to the satellite from its adjacent satellite nodes is reduced by using the revised r . When the predicted traffic is light, the traffic sent to the satellite from its adjacent satellite nodes is increased by using the revised r . Thus, the preference factor r should be adjusted according to the traffic model P .

(4) *Prediction and Routing Update.* Each satellite node maintains a data structure which records required information including the local traffic. The training process for ELM in each source node is started since source node sends data and forward MA goes to destination node. When backward MA returns to source node, a prediction agent is activated. Factually, the training process has been in progress before the activation. Thus, the required predicted traffic can be quickly given by the prediction MA. The future state of satellite node, the preference factor, and routing update are determined according to the predicted traffic.

Let Δt denote the prediction interval, \hat{P} denote the traffic load forecast at the time $t + \Delta t$, Q denote the queue size, $q(t)$ denote the queue occupancy state at the time t , C denote the capacity of ISL, d_{avg} denote the packet length in average, and B denote the router buffer capacity, respectively. The following metric named congestion indicator is defined to characterize the load state of satellite node:

$$\xi(t) = \frac{(Q - q(t)) \cdot d_{\text{avg}} + C \cdot \Delta t - \hat{P}}{B}. \quad (5)$$

The revising factor γ is defined as

$$\gamma = \frac{1}{1 + \exp(-a\xi)}. \quad (6)$$

In (6), a denotes the slope parameter. The routing update is presented below:

$$\tau_{ij}(t+1) = (1 - \rho)\tau_{ij}(t) + \gamma \cdot \left[\sum_{k=1}^m \Delta\tau_{ij}^k(t) + \Delta\tau'_{ij}(t) \right]. \quad (7)$$

(5) *Link Handover Strategy.* Since link handover in LEO satellite network would have a negative impact on routing performance, the corresponding routing strategy must adapt to links' disconnection and reconnection. In view of the periodicity and predictability of satellite network topology, the link states of disconnection and reconnection can be calculated and stored in advance to facilitate the execution of link handover strategy. In order to illustrate the link handover strategy, we first specify the topology of LEO satellite network. Either Walker constellation or polar-orbit constellation has the topological snap demonstrated in Figure 4, in which the solid lines represent permanent intra-orbit link, while the dashed lines stand for inter-orbit links.

As shown in Figure 4, we suppose that a link handover happens to the inter-orbit link between LEO_101 and LEO_201. The influenced satellites mainly are LEO_101 and LEO_201, as well as their adjacent satellites. As illustrated in Figure 4, the four links of LEO_101 which connect LEO_102, LEO_201, LEO_111, and LEO_601 are numbered with 1, 2, 3, and 4, respectively. When the link between LEO_101 and LEO_201 is disconnected, the probability in the routing table of LEO_101 to send data packets to LEO_201 is proportionally allocated to LEO_102, LEO_111, and LEO_601, respectively. Likewise, LEO_201 takes the same action as LEO_101. We have the following expression:

$$\begin{aligned}P_{\text{LEO}_201,d} &= 0 \quad \forall d \in N, d \neq \text{LEO}_101 \\ P_{n,d} &= P_{n,d} + \frac{P_{n,d}}{\sum_{n=1}^{|N_{\text{LEO}_101}|-1}} \cdot P_{\text{LEO}_201,d} \\ n &\in N_{\text{LEO}_101}, n \neq \text{LEO}_201,\end{aligned}\quad (8)$$

where N_{LEO_101} is a collection including the satellite nodes whose data packets are sent to LEO_101. $|N_{\text{LEO}_101}|$ represents the number of satellite nodes in the collection N_{LEO_101} .

When the link between LEO_101 and LEO_201 is reconnected, the probabilities of links numbered 1, 3, and 4 are allocated to link 2 according to the following rule. Specifically, the number of hops from LEO_101 to the destination node is calculated. The smaller the number of hops is, the higher the probability of link 2 is [33]. Correspondingly, LEO_201 takes the action similar to LEO_101. Thus, we have

$$\begin{aligned}P_{\text{LEO}_201,d} &= \frac{\text{dist}(\text{LEO}_201, d)}{\sum_{n=1}^{|N_{\text{LEO}_101,d}|-1} \text{dist}(n, d)} \\ \forall d \in N, d \neq \text{LEO}_101, n &\in N_{\text{LEO}_101}, n \neq \text{LEO}_201 \\ P_{n,d} &= P_{n,d} \cdot \left[1 - \frac{\text{dist}(\text{LEO}_201, d)}{\sum_{n=1}^{|N_{\text{LEO}_101,d}|-1} \text{dist}(n, d)} \right] \\ \forall d \in N, d \neq \text{LEO}_101, n &\in N_{\text{LEO}_101}, n \neq \text{LEO}_201,\end{aligned}\quad (9)$$

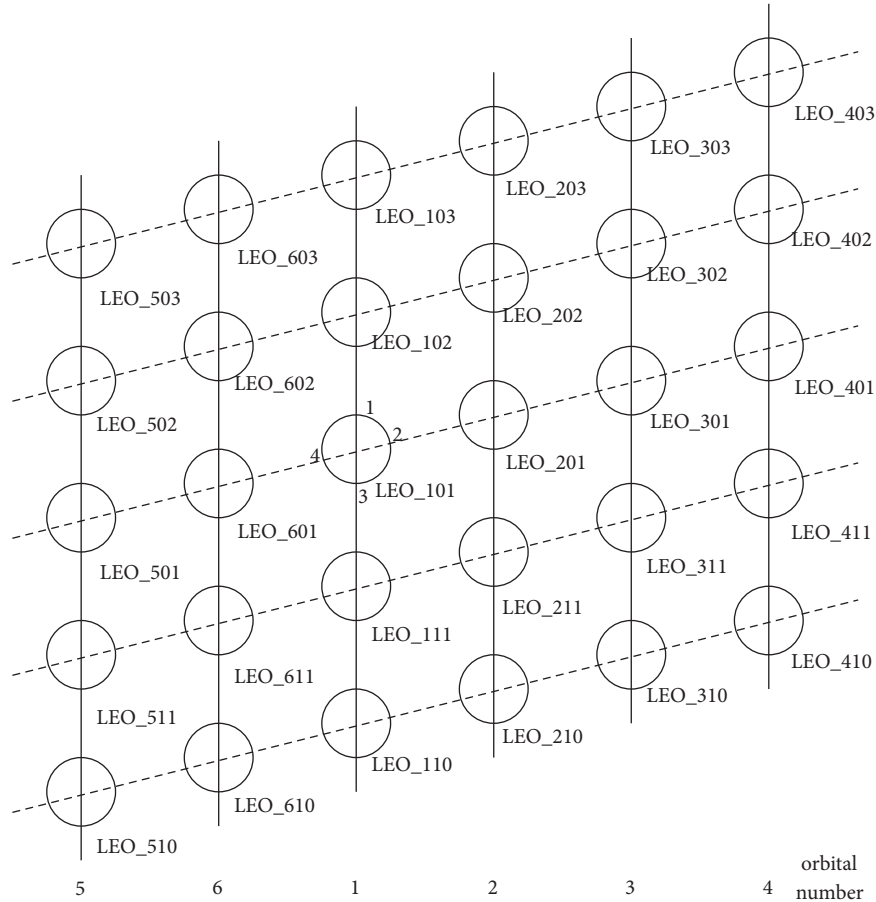


FIGURE 4: Typical topological snap of LEO satellite network.

where $\text{dist}(n, d)$ is used to calculate the number of hops on link (n, d) .

When link disconnection happens, routing table can fast-track it according to (8) because neither MAs nor data packets will be forwarded over the disconnected link. Considering the frequent link handover in LEO satellite network, if the routing strategy is always behind the change of network state, routing performance is bound to be affected. Fortunately, the periodicity and predictability of LEO satellite network topology make the real-time tracking of link handover possible.

(6) *Main Flow of ELMDR Strategy.* The main flow of ELMDR strategy is listed in Algorithm 1, which illustrates the process of routing establishment, update, and revision.

4. Simulation Results and Discussions

The performance of ELMDR is dependent on the accuracy of traffic prediction method to a large extent. In order to validate the prediction effect of ELM, we select the Internet data trace which is available on the website: <http://ita.ee.lbl.gov/index.html>. There are many data traces last updated on April 9, 2008, on the website. We use the trace of BC-pAug89 which started from 11:25 to 12:17 (about

3143 s) on August 29, 1989. 1,000,000 packets are included in the trace. As IP packets to a given destination in the modern Internet backbone present high self-similarity [34], there are no accurate models to predict Internet traffic [35]. We select one percent of the trace to train ELM. Because of traffic similarity, the data segment can be selected arbitrarily in the trace. We select the data in the first 5 s as the testing data. In view of the randomness of the time that a packet arrived at measurement hardware, we count the bytes in each interval of 0.04 s from the first to the 2140th packet captured (about 5 s). We implement the traffic prediction by using ELM based on MATLAB. The real traffic and the predicted traffic by ELM are compared and demonstrated in Figure 5. It is obvious that ELM can follow the change of real traffic only with minor errors. When real traffic sharply increases or decreases, the predicted traffic is often slightly below or above real traffic because of both the high similarity and the passiveness of prediction algorithm. Overall, ELM is competent for traffic prediction in the proposed routing strategy.

To verify the proposed routing strategy, the Iridium satellite system with the topology depicted in Figure 4 is used as the simulation scenario. The following parameters are used in our simulations: $a = 1$, $\rho = 0.75$, $q_1 = 0.2$, $c_1 = 0.7$, and $c_2 = 0.3$; the bandwidth of ISL is 10 Mbps. The simulation scenario is presented in Figure 6. We suppose Gateway 1 and Gateway

```

begin
  initialize routing table and data structure
  (A) satellite node generates and sends forward MA
  (B) select the next node according to (1)
  (C) handover judgement according to (8) and (9)
  (D) if loop avoidance == true
    go to step (E)
  else
    go to step (B)
  (E) record delay at intermediate node
  (F) forward MA arrives at destination node
  (G) destination node generates and sends backward MA
  (H) backward MA returns to source node
  (I) handover judgement according to (8) and (9)
  (J) update routing table according to (2) and data structure according to (3)
  (K) prediction MA is activated to predict traffic at satellite node
  (L) revise routing table according to (4)–(7)
End

```

ALGORITHM 1: Main flow of ELMDR strategy.

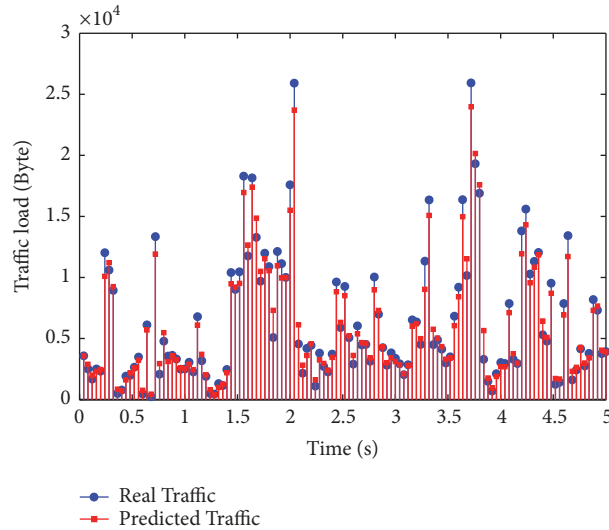


FIGURE 5: Real traffic and predicted traffic.

2 are connected to LAN1 and LAN2, respectively. LAN1 sends data to LAN2 10 s later. All scenario parameters are implemented on OPNET. The Ant Colony Optimization algorithm abbreviated as ACO [36] and proposed ELMDR are compared.

Figures 7 and 8 present the link utilization performance of ACO and ELMDR. When LAN1 starts sending data to LAN2, the optimal path from LEO_301 to LEO_401 for both ACO and ELMDR is utilized with the similar link utilization. However, ACO only selects one optimal path, while ELMDR offloads a part of traffic to the suboptimal path from LEO_301 to LEO_302. In simulation, the training time and the testing time are less than 0.1 s. As shown in Figure 8, though the activation of prediction MA and the training and testing process need time, the discovery of suboptimal path for ELMDR is still earlier than ACO mainly because

ELMDR can avoid path search falling into standstill and find suboptimal path promptly. Therefore, the discovery of paths from LEO_301 to LEO_302 and from LEO_301 to LEO_311 for ELMDR is earlier than ACO. It should be noted that the link utilization of the path from LEO_301 to LEO_201 for both ELMDR and ACO is zero, because the path is neither selected by ELMDR nor selected by ACO.

Figure 9 presents the queuing delay of LEO_301 in the case of link handover. Compared with ACO, as shown in Figure 9, the queuing delay for ELMDR caused by link handover changes slightly mainly because ELMDR can fast update routing table and follow the change of link state. Since the links from satellite LEO_301 to satellite LEO_302 and from satellite LEO_301 to satellite LEO_311 are utilized, a part of data packets avoids being sent to the originally congested node LEO_301. Though the distance between source node

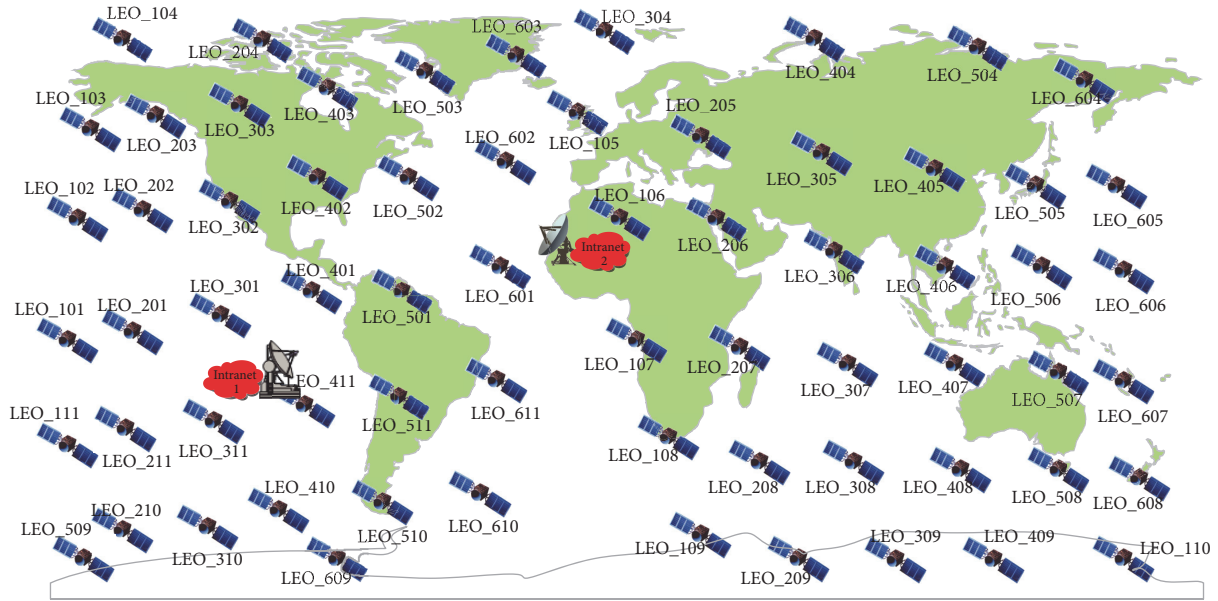


FIGURE 6: LEO satellite network scenario.

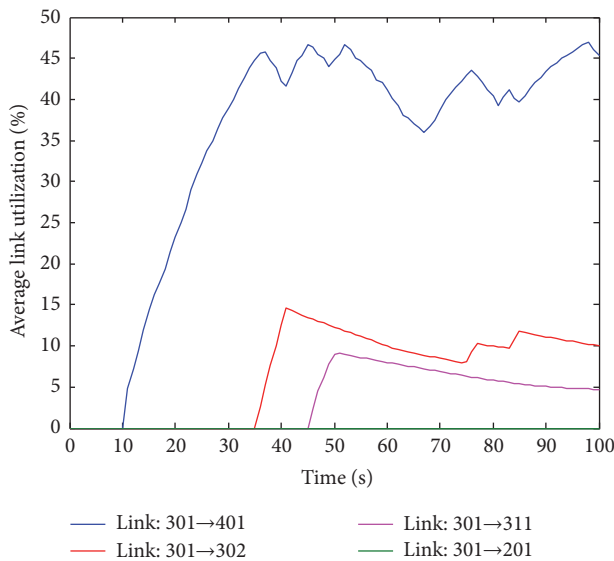


FIGURE 7: Link utilization of ACO.

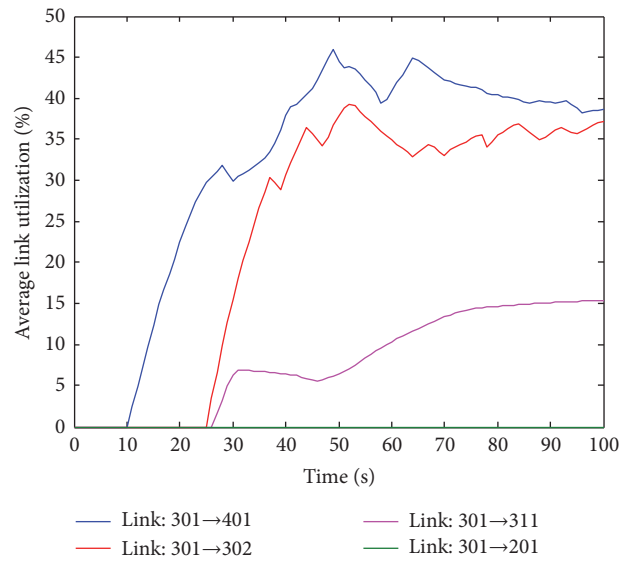


FIGURE 8: Link utilization of ELMDR.

and destination node would increase, the queuing delay for LEO_301 is highly decreased.

Figures 10 and 11 present packet loss ratio (PLR) and average packet delay of ACO and ELMDR, respectively. In Figure 10, when sending rate is relatively low, both ACO and ELMDR provide almost the same PLR. However, when sending rate is high, ELMDR takes a slight lead. Because traffic prediction is adopted by ELMDR, data is diverted to suboptimal path. As a result, the packet losses due to timeout over congested link are decreased. Figure 11 demonstrates that ELMDR has slightly higher average delay than ACO. Though the paths from LEO_301 to LEO_302 and from LEO_301 to LEO_311 would increase the communication

distance between source node and destination node, the sacrifice in average delay is affordable considering the lower link handover delay, PLR, and higher link utilization.

5. Conclusions

In this paper, a distributed routing strategy based on machine learning for Low Earth Orbit satellite network is put forward. The traffic load on the ground is analyzed and quantified, and then Extreme Learning Machine is adopted to forecast the traffic load of satellite node. The proposed routing is realized based on distributed mobile agents, which can search for, collect, update, and revise routing information. Prediction

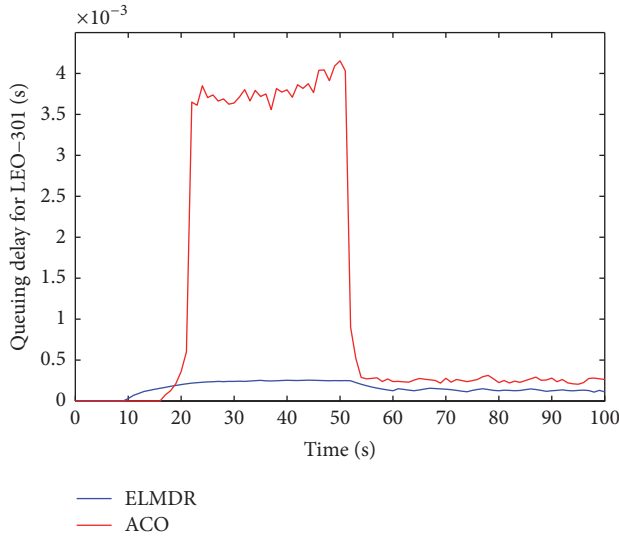


FIGURE 9: Queuing delay with handover for LEO_301.

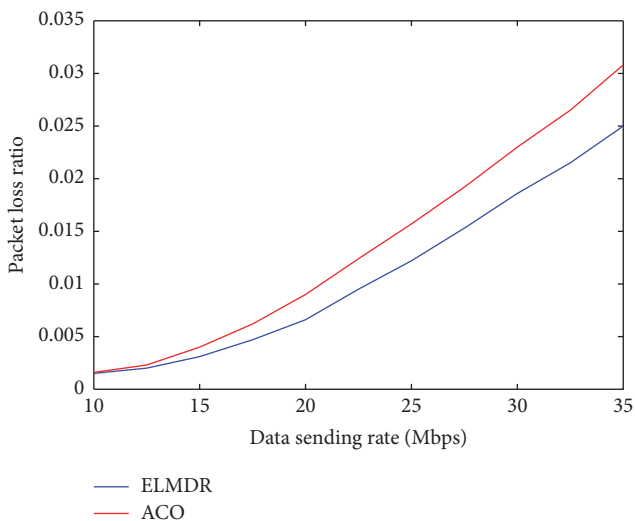


FIGURE 10: Packet loss ratio.

mobile agents revise routing by a preference factor so that congestion can be avoided. The additional link handover strategy ensures that traffic load can be diverted to the appropriate satellite nodes according to the probability in the case of link disconnection or reconnection. Simulation results demonstrate that, compared with ACO, the proposed ELMDR provides suboptimal path in the case of link handover and has low packet loss ratio and handover delay at the cost of slighter average delay.

Conflicts of Interest

The authors declare that there are no conflicts of interest regarding the publication of this paper.

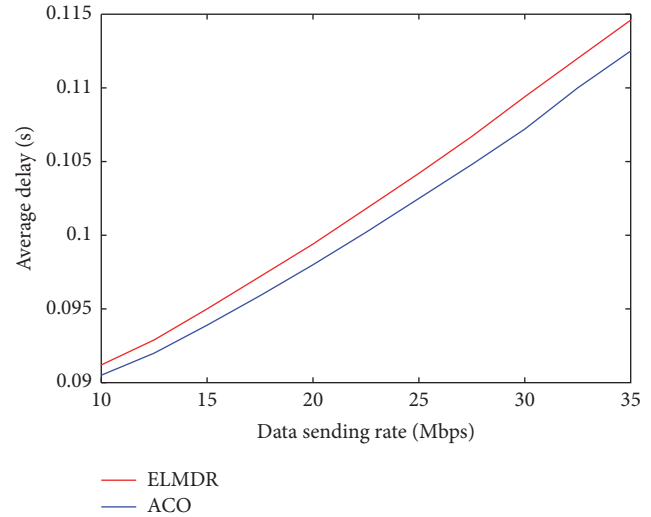


FIGURE 11: Average delay.

Acknowledgments

The authors would especially like to thank Professor Mu-Di Xiong and Professor Dian-Wu Yue from Dalian Maritime University for their help in laboratory space and experiment fund. The research and publication of this work were funded by the National Natural Science Foundation of China under Grants nos. [61301131] and [61601221], the Natural Science Foundation of Jiangsu Province under Grant no. [BK20140828], the China Postdoctoral Science Foundation under Grant no. [2015M580425], and the Fundamental Research Funds for the Central Universities under Grants nos. [3132016347] and [DUT16RC(3)045].

References

- [1] R. Wang, M. Qiu, K. Zhao, and Y. Qian, "Optimal RTO timer for best transmission efficiency of DTN protocol in deep-space vehicle communications," *IEEE Transactions on Vehicular Technology*, vol. 66, no. 3, pp. 2536–2550, 2017.
- [2] A. Meloni and L. Atzori, "The role of satellite communications in the smart grid," *IEEE Wireless Communications Magazine*, vol. 24, no. 2, pp. 50–56, 2017.
- [3] Y. Rahmat-Samii and A. C. Densmore, "Technology trends and challenges of antennas for satellite communication systems," *Institute of Electrical and Electronics Engineers. Transactions on Antennas and Propagation*, vol. 63, no. 4, part 1, pp. 1191–1204, 2015.
- [4] M. Jia, X. Gu, Q. Guo, W. Xiang, and N. Zhang, "Broadband hybrid satellite-terrestrial communication systems based on cognitive radio toward 5G," *IEEE Wireless Communications Magazine*, vol. 23, no. 6, pp. 96–106, 2016.
- [5] Z. Na, Z. Pan, M. Xiong et al., "Turbo receiver channel estimation for GFDM-based cognitive radio networks," *IEEE Access*, vol. 6, pp. 9926–9935, 2018.
- [6] G. Song, M. Chao, B. Yang, and Y. Zheng, "TLR: a traffic-light-based intelligent routing strategy for N GEO satellite IP networks," *IEEE Transactions on Wireless Communications*, vol. 13, no. 6, pp. 3380–3393, 2014.

- [7] Y. Yang, M. Xu, D. Wang, and Y. Wang, "Towards energy-efficient routing in satellite networks," *IEEE Journal on Selected Areas in Communications*, vol. 34, no. 12, pp. 3869–3886, 2016.
- [8] H. Uzunalioglu, I. F. Akyildiz, and M. D. Bender, "A routing algorithm for connection-oriented Low Earth Orbit (LEO) satellite networks with dynamic connectivity," *Wireless Networks*, vol. 6, no. 3, pp. 181–190, 2000.
- [9] M. Werner, "A dynamic routing concept for ATM-based satellite personal communication networks," *IEEE Journal on Selected Areas in Communications*, vol. 15, no. 8, pp. 1636–1648, 1997.
- [10] H. S. Chang, B. W. Kim, C. G. Lee et al., "FSA-based link assignment and routing in low-earth orbit satellite networks," *IEEE Transactions on Vehicular Technology*, vol. 47, no. 3, pp. 1037–1048, 1998.
- [11] A. Z. Shahriar, M. Atiquzzaman, and S. Rahman, "Mobility management protocols for next-generation all-IP satellite networks," *IEEE Wireless Communications Magazine*, vol. 15, no. 2, pp. 46–54, 2008.
- [12] E. Ekici, I. Akyildiz, and M. Bender, "Datagram routing algorithm for LEO satellite networks," in *Proceedings of the IEEE INFOCOM 2000. Conference on Computer Communications. Nineteenth Annual Joint Conference of the IEEE Computer and Communications Societies*, vol. 2, pp. 500–508, Tel Aviv, Israel.
- [13] M. De Sanctis, E. Cianca, and M. Ruggieri, "Improved algorithms for Internet routing in low earth orbit satellite networks," *Space Communications*, vol. 20, no. 3-4, pp. 171–182, 2005.
- [14] W. Xu, M. Jiang, F. Tang, and Y. Yang, "Network coding-based multi-path routing algorithm in two-layered satellite networks," *IET Communications*, vol. 12, no. 1, pp. 2–8, 2018.
- [15] T. Taleb, Z. M. Fadlullah, T. Takahashi, R. Wang, Y. Nemoto, and N. Kato, "Tailoring ELB for multi-layered satellite networks," in *Proceedings of the 2009 IEEE International Conference on Communications, ICC 2009*, June 2009.
- [16] H. Wang, Q. Zhang, X. Xin, Y. Tao, and N. Liu, "Cross-layer design and ant-colony optimization based routing algorithm for low earth orbit satellite networks," *China Communications*, vol. 10, no. 10, Article ID 6650318, pp. 37–46, 2013.
- [17] D. Yan and L. Wang, "TPDR: traffic prediction based dynamic routing for LEO&GEO satellite networks," in *Proceedings of the 5th IEEE International Conference on Electronics Information and Emergency Communication, ICEIEC 2015*, pp. 104–107, May 2015.
- [18] H. Nishiyama, D. Kudoh, N. Kato, and N. Kadowaki, "Load balancing and qos provisioning based on congestion prediction for GEO/LEO hybrid satellite networks," *Proceedings of the IEEE*, vol. 99, no. 11, pp. 1998–2007, 2011.
- [19] A. Jankowska, M. C. Schut, and N. Ferreira-Schut, "A wireless actuator-sensor neural network for evacuation routing," in *Proceedings of the 2009 3rd International Conference on Sensor Technologies and Applications, SENSORCOMM 2009*, pp. 139–144, June 2009.
- [20] S.-Z. Huang and L.-Y. Huang, "The optimal routing algorithm of communication networks based on neural network," in *Proceedings of the 2010 International Conference on Intelligent Computation Technology and Automation, ICICTA 2010*, vol. 3, pp. 866–869, May 2010.
- [21] P. P. Repoussis, C. D. Tarantilis, O. Bräysy, and G. Ioannou, "A hybrid evolution strategy for the open vehicle routing problem," *Computers & Operations Research*, vol. 37, no. 3, pp. 443–455, 2010.
- [22] X. Zhang, L. Ding, and Y. Rao, "QoS routing by genetic algorithm for LEO satellite networks," in *Proceedings of the 2009 Second International Symposium on Computational Intelligence and Design*, vol. 1 of 344, 341 pages, 2009.
- [23] B.-B. Jiang, H.-M. Chen, L.-N. Ma, and L. Deng, "Time-dependent pheromones and electric-field model: a new ACO algorithm for dynamic traffic routing," *International Journal of Modelling, Identification and Control*, vol. 12, no. 1-2, pp. 29–35, 2011.
- [24] X.-M. Wang and A. N. Xiao-Ming, "An energy and location aware ACO based routing algorithm for wireless sensor networks," *Tien Tzu Hsueh Pao/Acta Electronica Sinica*, vol. 38, no. 8, pp. 1763–1769, 2010.
- [25] G. Zihe, G. Qing, and N. Zhenyu, "A distributed routing algorithm with traffic prediction in LEO satellite networks," *Information Technology Journal*, vol. 10, no. 2, pp. 285–292, 2011.
- [26] Z. Na, Z. Gao, Y. Cui, L. Chen, and Q. Guo, "Agent-based distributed routing algorithm with traffic prediction for LEO satellite network," vol. 6, pp. 67–84.
- [27] C. Jiang, H. Zhang, Y. Ren, Z. Han, K.-C. Chen, and L. Hanzo, "Machine learning paradigms for next-generation wireless networks," *IEEE Wireless Communications Magazine*, vol. 24, no. 2, pp. 98–105, 2017.
- [28] J. Kremer, K. Stensbo-Smidt, F. Gieseke, K. S. Pedersen, and C. Igel, "Big universe, big data: machine learning and image analysis for astronomy," *IEEE Intelligent Systems*, vol. 32, no. 2, pp. 16–22, 2017.
- [29] G. B. Huang, Q. Y. Zhu, and C. K. Siew, "Extreme learning machine: a new learning scheme of feedforward neural networks," in *Proceedings of the IEEE International Joint Conference on Neural Networks*, vol. 2, pp. 985–990, July 2004.
- [30] T. Alumni, "Bites from the classroom: GDP density and unemployment," <http://logos.nationalinterest.in/2015/01/bites-from-the-classroom-gdp-density-and-unemployment/>, 2015.
- [31] S. Wang, C. Deng, W. Lin, G. Huang, and B. Zhao, "NMF-based image quality assessment using extreme learning machine," *IEEE Transactions on Cybernetics*, vol. 47, no. 1, pp. 232–243, 2017.
- [32] G. Huang, L. Chen, and C. Siew, "Universal approximation using incremental constructive feedforward networks with random hidden nodes," *IEEE Transactions on Neural Networks and Learning Systems*, vol. 17, no. 4, pp. 879–892, 2006.
- [33] Z. Gao, Q. Guo, and Z. Na, "A novel routing algorithm combined with multi-agent system for LEO satellite IP networks," in *Proceedings of the 2009 International Conference on Wireless Communications and Signal Processing, WCSP 2009*, November 2009.
- [34] M. Grossglauser and J.-C. Bolot, "On the relevance of long-range dependence in network traffic," *IEEE/ACM Transactions on Networking*, vol. 7, no. 5, pp. 629–640, 1999.
- [35] B. Zhou, D. He, and Z. Sun, "Traffic predictability based on ARIMA/GARCH model," in *Proceedings of the 2006 2nd Conference on Next Generation Internet Design and Engineering, NGI 2006*, pp. 200–207, Spain, April 2006.
- [36] Z. Zhang, K. Long, J. Wang, and F. Dressler, "On swarm intelligence inspired self-organized networking: its bionic mechanisms, designing principles and optimization approaches," *IEEE Communications Surveys & Tutorials*, vol. 16, no. 1, pp. 513–537, 2014.

Research Article

Pedestrian Motion Learning Based Indoor WLAN Localization via Spatial Clustering

Xiaolong Yang , Yanmeng Wang , Mu Zhou , and Yiyao Liu

Chongqing Key Lab of Mobile Communications Technology, Chongqing University of Posts and Telecommunications, Chongqing 400065, China

Correspondence should be addressed to Yanmeng Wang; hiwangym@gmail.com

Received 25 December 2017; Revised 8 March 2018; Accepted 16 April 2018; Published 15 May 2018

Academic Editor: Xin-Lin Huang

Copyright © 2018 Xiaolong Yang et al. This is an open access article distributed under the Creative Commons Attribution License, which permits unrestricted use, distribution, and reproduction in any medium, provided the original work is properly cited.

Applications on Location Based Services (LBSs) have driven the increasing demand for indoor localization technology. The conventional location fingerprinting based localization involves heavy time and labor cost for database construction, while the well-known Simultaneous Localization and Mapping (SLAM) technique requires assistant motion sensors as well as complicated data fusion algorithms. To solve the above problems, a new pedestrian motion learning based indoor Wireless Local Area Network (WLAN) localization approach is proposed in this paper to achieve satisfactory LBS without the demand for location calibration or motion sensors. First of all, the concept of pedestrian motion learning is adopted to construct users' motion paths in the target environment. Second, based on the timestamp relation of the collected Received Signal Strength (RSS) sequences, the RSS segments are constructed to obtain the signal clusters with the newly defined high-dimensional linear distance. Third, the PageRank algorithm is performed to establish the hotspot mapping relations between the physical and signal spaces which are then used to localize the target. Finally, the experimental results show that the proposed approach can effectively estimate the target's locations and analyze users' motion preference in indoor environment.

1. Introduction

For well over a decade, the rapid development of wireless communication technology has driven the increasing demand for the Location Based Services (LBSs) [1–3]. Because of the complicated indoor building structure and multipath effect, the performance of the outdoor positioning systems such as Global Positioning will dramatically deteriorate in indoor environment. Meanwhile, with the wide deployment of Wireless Local Area Network (WLAN) infrastructure, WLAN has become one of the priorities for indoor positioning [4].

Due to the easily accessible WLAN Received Signal Strength (RSS), the location fingerprinting based WLAN indoor localization systems [5, 6] have been widely researched. These systems generally contain two phases, namely, offline and online phases. In offline phase, the RSS data from the hearable Access Points (APs) at each precalibrated Reference Point (RP) are collected to construct fingerprint database. Then, in online phase, the newly collected RSS data are

matched against fingerprint database to obtain the target location estimate [7]. However, because of the heavy time and labor cost for fingerprint database construction, this technology cannot be widely spread especially in the large-scale environment.

To mitigate the cost of fingerprint database construction, the calibration-free indoor localization approaches have been intensively studied. By integrating the RSS data with motion sensor information, the Simultaneous Localization and Mapping (SLAM) technique [8] is proposed to effectively reduce the overhead of fingerprints calibration. Based on the specially designed sniffers, the authors in [9] conduct the dynamic radio map of target indoor environment to perform localization. In [10], the RSS measurements are fused with the odometric data from the foot-mounted Inertial Measurements Units (IMU) to conduct pedestrian navigation, and the odometry based Bayesian inference theory used for localization is analyzed in [11]. In all, the SLAM based localization techniques need additional motion sensors [12],

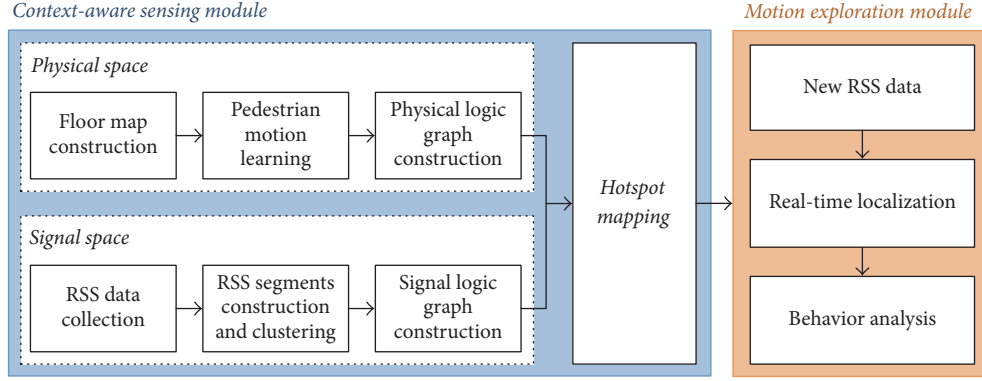


FIGURE 1: Flowchart of the proposed approach.

as well as the sophisticated algorithms for feature extraction and data fusion [13].

Different from these approaches, a new pedestrian motion learning based indoor WLAN localization approach is proposed in this paper, which has no demands for fingerprints calibration or assistant motion sensors. In general, there are four contributions of this paper as follows.

- (1) Indoor user's behavior model construction by pedestrian motion learning: with the statistical observation of users' motion patterns, a heuristic pedestrian motion learning approach is performed to construct users' walking paths in indoor environment.
- (2) RSS data collection without fingerprints calibration: different from the location fingerprinting or SLAM based approaches, the RSS data in our approach are collected based on the motion behavior model corresponding to the users' daily routines in the target area.
- (3) Signal clustering on RSS segments: based on the timestamp relations of the collected RSS sequences, the RSS segments which reflect users' continuous movement are constructed to obtain the signal clusters with newly defined high-dimensional linear distance.
- (4) Comprehensive motion behavior analysis: the activity frequency of each physical subarea and the related transfer frequency between different physical subareas exhibit the users' movement preference in the target environment.

The rest of this paper is organized as follows. Section 2 describes the proposed approach in detail. Then, Section 3 illustrates the experimental results. Finally, Section 4 concludes the paper and gives some future directions.

2. System Description

The proposed approach contains two main modules, namely, the context-aware sensing module and the motion exploration module as shown in Figure 1.

In the process of context-aware sensing, we first construct the floor map of target environment and then adopt the pedestrian motion learning to establish the users' motion

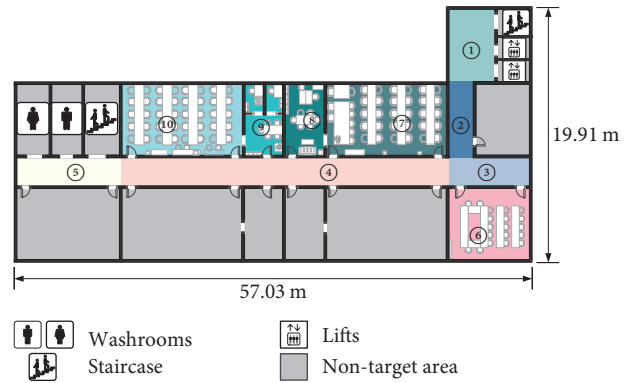


FIGURE 2: Division of target environment.

behavior model. After that, according to the transfer relations between different physical subareas which are associated with users' motion paths, the physical logic graph is constructed. Meanwhile, the RSS segments are constructed by mapping the raw RSS data into two-dimensional plane, and the density based spatial clustering is adopted to merge the RSS segments with respect to the similar motion behavior together. Then, with the transfer relations between different signal clusters, the signal logic graph is constructed. After the construction of logic graphs, PageRank algorithm [15] is performed to establish hotspot mapping relations between the physical and signal spaces.

Then, in the process of motion exploration, the new RSS data collected by users is compared with each signal cluster, and the physical subarea mapped to the most similar one is selected as the area that the user most likely belongs to. In addition, based on the area-level localization results, the users' motion behavior in the target environment is analyzed.

2.1. Floor Map Construction. By considering the functional differentiation of different physical subareas in floor map, we divide the target environment into $N_{\text{area}} (= 10)$ physical subareas as shown in Figure 2. In this figure, subarea #1 is the doorway to the lifts and a staircase, subareas #2, #3, and #4 are the corridors to the office rooms, subarea #5 is the doorway to the washrooms and another staircase, and the other subareas are the office rooms.

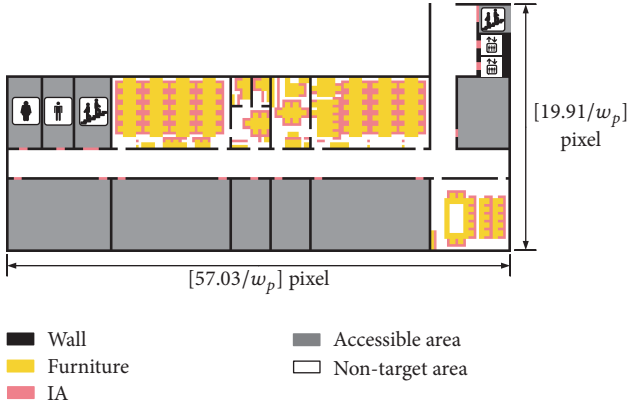


FIGURE 3: Transformed image of floor map.

The objects in target environment mainly involve the walls, doors, and furniture. Among them, the furniture is the most favored target at which the users much probably arrive. When the user arrives at a piece of furniture like the table, chair, bookcase, and drinking fountain, he/she will normally stay for a while. Thus, we define the physical area around each piece of furniture as *Interested Area* (IA), and meanwhile the users' motion paths are much likely to be the paths between different IAs. For example, the path from a chair to a drinking fountain indicates that the user has planned to get some water during the work time.

To simulate the users' motion paths in target environment, we transform the floor map into an image with the pixel width equalling w_p ($= 0.3$ m) in Figure 3, where the notation "[•]" represents the integer operation. In this case, the motion paths simulation is equivalent to the determination of the pixels reflecting the users' motion behavior in target environment.

2.2. Pedestrian Motion Learning. By using the pedestrian motion learning, we construct the motion paths in the transformed image of floor map. Then, according to the statistical observation, there are three typical types of users' motion behavior as follows.

- (i) The motion paths from the staircases and lifts to office rooms.
- (ii) The motion paths between different IAs.
- (iii) The motion paths from office rooms to staircase or staircases and lifts.

Meanwhile, based on our previous A* algorithm based motion path simulation approach [16], we define the cost function with respect to the walking distance from start to end points as

$$F(t, i) = G(t, i) + H(t, i), \quad (1)$$

where $G(t, i)$ is the distance from the starting pixel to current one i at moment t , which is the distance estimation of the passed path. In this paper, the Euclidean distance is adopted to estimate this type of distance since it is in accordance with users' habit of measuring the path he/she has passed. $H(t, i)$ is the distance from the current to ending pixels, which is measured by Manhattan distance by considering that the

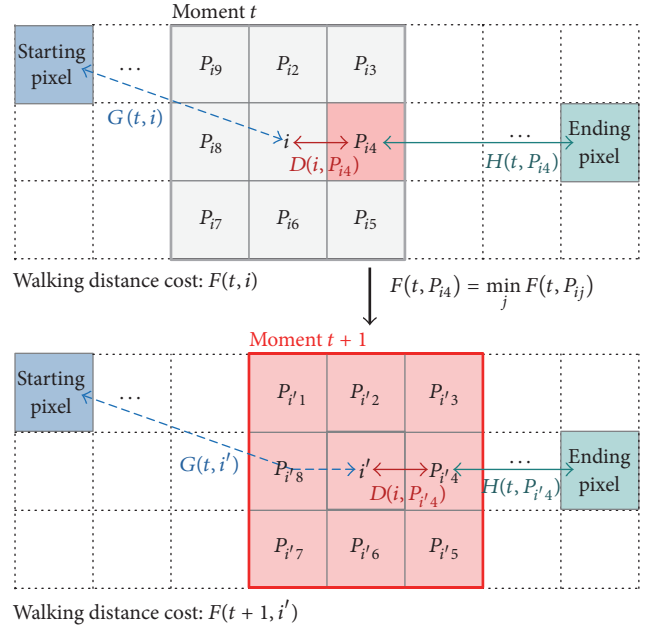


FIGURE 4: Walking distance cost updating.

ending pixel is non-line-of-sight (NLOS) to the user in most cases.

At each moment, the defined walking distance cost of each motion path is iteratively updated. Specifically, on each motion path, when the current pixel i is obtained (in the first iteration, the current pixel is randomly selected from the starting IA which is determined by the related motion behavior), the walking distance cost with respect to the eight adjacent pixels of i , P_{ij} , can be represented by

$$F(t, P_{ij}) = G(t, i) + D(i, P_{ij}) + H(t, P_{ij}), \quad (2)$$

where $D(i, P_{ij})$ is the Euclidean distance between the current pixel i and its adjacent one. Then, the accessible adjacent pixel with the smallest walking distance cost is selected as the next pixel i' (or the current pixel at the next moment $t + 1$). We continue this process until the current pixel falls into the ending IA which is determined by the related motion behavior. Following this heuristic learning way, each motion path of pedestrians in target environment, which is constituted by a series of consecutive pixels, can be obtained. Figure 4 gives an example of walking distance cost updating in the process of one motion path construction.

In addition, in order to incorporate the randomness property into motion paths construction, a small proportion of accessible pixels are randomly converted into inaccessible ones, which will block the users' motion paths in target environment. The pseudocode of pedestrian motion learning is shown in Algorithm 1.

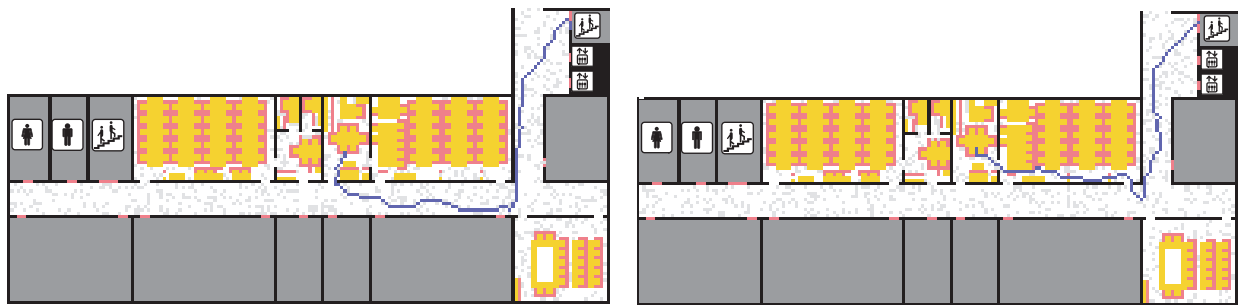
Figure 5 shows an example of two different generated motion paths starting from the same staircase to a table, from which we can find that the randomness property results in different constructed motion paths even if the starting and ending pixels are the same.

Finally, according to the transfer relations of motion paths between different physical subareas, the physical logic

Input: Starting and ending pixels, A and B
Output: Motion path from A to B

- (1) Set starting pixel as $A = (x_A, y_A)$; // Starting pixel
- (2) Set ending pixel as $B = (x_B, y_B)$; // Ending pixel
- (3) A certain proportion of accessible pixels are converted into inaccessible ones;
- (4) Add A into Possible Path Location (PPL) set;
- (5) Initialize Existing Path Location (EPL) as an empty set;
- (6) $i \leftarrow A$; // Current pixel
- (7) **while** i is not equal to B **do**
- (8) **for** (each adjacent pixel around i, P_{ij}) // Pixel traversal
- (9) **if** P_{ij} is an inaccessible pixel **then**
- (10) **Continue**;
- (11) **else if** P_{ij} belongs to EPL set **then**
- (12) **Continue**;
- (13) **else if** P_{ij} is neither in EPL set nor in PPL set **then**
- (14) Add P_{ij} into PPL set;
- (15) Set i as the father pixel of P_{ij} ;
- (16) Calculate the Euclidean distance from P_{ij} to A, G_{ij} ;
- (17) Calculate the Manhattan distance from P_{ij} to B, H_{ij} ;
- (18) Set $F_{ij} = G_{ij} + H_{ij}$;
- (19) **else if** P_{ij} belongs to PPL set **then**
- (20) Calculate the distance from i to P_{ij}, D_{ij} ;
- (21) $G'_{ij} \leftarrow G_i + D_{ij}$;
- (22) **If** $G'_{ij} < G_{ij}$ **then**
- (23) $G_{ij} \leftarrow G'_{ij}$;
- (24) $F_{ij} \leftarrow G'_{ij} + H_{ij}$;
- (25) Set i as the father pixel of P_{ij} ;
- (26) **end if**
- (27) **end if**
- (28) **end for**
- (29) Add i into EPL set;
- (30) Remove i from PPL set;
- (31) Update i with the pixel with the smallest value F_{ij} in PPL set;
- (32) **end while**
- (33) $N_t = B$; // Initialize traversal pixel
- (34) Add B into set **Trace** as the 1st pixel;
- (35) $k \leftarrow 2$;
- (36) **while** N_t is not equal to A
- (37) Add the father pixel of N_t into **Trace** as k -th pixel;
- (38) $k \leftarrow k + 1$;
- (39) $N_t \leftarrow$ Father pixel of N_t ;
- (40) **end while**
- (41) Consecutively connect the pixels in **Trace** as the constructed motion path.

ALGORITHM 1: Pseudocode of pedestrian motion learning.



■ Converted inaccessible pixels
 — Motion path 1

(a) Motion path #1

■ Converted inaccessible pixels
 — Motion path 2

(b) Motion path #2

FIGURE 5: Construction of two motion paths with the same starting and ending locations.

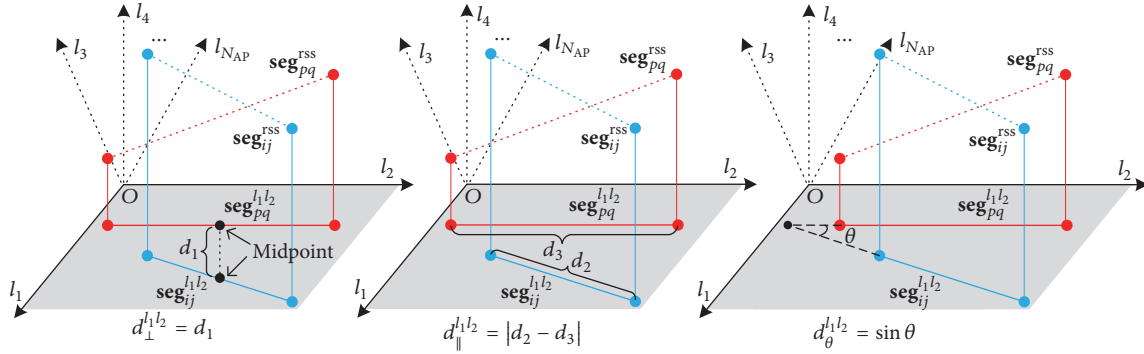


FIGURE 6: Definition of the vertical, parallel, and angular distances.

graph can be constructed, where a transfer between any two adjacent physical subareas is counted only if there is a pair of consecutive pixels located into these two subareas, respectively.

2.3. RSS Segments Construction and Clustering. Based on the pedestrian motion learning, some specific pixels on each motion path are labeled with the consideration of the statistical result corresponding to pedestrians' motion velocities [17]. At the same time, the RSS data at each labeled pixel is calculated from the COST231 model [18, 19] which has a good compromise among the computation complexity, system flexibility, and practicability. The set of RSS data at the labeled pixels on the i th motion path forms the RSS sequence collected on the i th motion path, $\mathbf{RSS}_i = \{\mathbf{rss}_{i1}, \dots, \mathbf{rss}_{im_i}\}$, where \mathbf{rss}_{ij} ($j = 1, \dots, m_i$) is the RSS data at the j th labeled pixel on the i th motion path and m_i is the number of labeled pixels on the i th motion path, and \mathbf{rss}_{ij} is the RSS value from the l th ($l = 1, \dots, N_{\text{AP}}$) AP which is calculated by

$$\text{rss}_{ijl} = \text{rss}_0 - 10\beta \log\left(\frac{d_l}{d_0}\right) - n_0 - P_a, \quad (3)$$

where N_{AP} is the number of APs, d_l is the Euclidean distance between the target and l th AP, d_0 is the reference distance which is usually set as 1m, rss_0 is the RSS at reference location, β is attenuation exponent, n_0 is Gaussian noise, and $P_a = P_a^{\text{wall}} + P_a^{\text{body}}$ is the attenuation caused by walls and pedestrian's body between the target and l th AP, where P_a^{wall} and P_a^{body} ($= 9.32$ dB) stand for the attenuation factors with respect to the walls and human body, respectively, which are obtained from [20].

After the RSS sequences are generated, the RSS segments are constructed with the timestamp relations of RSS sequences. In concrete terms, the RSS segments are constructed as $\mathbf{seg}_{ij}^{\text{rss}} = [\mathbf{rss}_{ij}, \mathbf{rss}_{i(j+1)}]$, in which each RSS data is viewed as a vertex and the connection between every two consecutive RSS data is viewed as an edge in the N_{AP} -dimensional space. To measure the similarity between two RSS segments, $\mathbf{seg}_{ij}^{\text{rss}} = [\mathbf{rss}_{ij}, \mathbf{rss}_{i(j+1)}]$ and $\mathbf{seg}_{pq}^{\text{rss}} = [\mathbf{rss}_{pq}, \mathbf{rss}_{p(q+1)}]$, we define a new N_{AP} -dimensional linear distance as

$$d_{\text{seg}}^{ij-pq} = \sum_{l_1, l_2 \in \{1, \dots, N_{\text{AP}}\}; l_1 \neq l_2} \bar{d}_{\perp}^{l_1 l_2} + \bar{d}_{\parallel}^{l_1 l_2} + \bar{d}_{\theta}^{l_1 l_2}, \quad (4)$$

where $\bar{d}_{\perp}^{l_1 l_2}$, $\bar{d}_{\parallel}^{l_1 l_2}$, and $\bar{d}_{\theta}^{l_1 l_2}$ are the normalized values of the vertical distance $d_{\perp}^{l_1 l_2}$, parallel distance $d_{\parallel}^{l_1 l_2}$, and angle distances $d_{\theta}^{l_1 l_2}$ between $\mathbf{seg}_{ij}^{l_1 l_2} = [(\text{rss}_{ijl_1}, \text{rss}_{ijl_2}), (\text{rss}_{i(j+1)l_1}, \text{rss}_{i(j+1)l_2})]$ and $\mathbf{seg}_{pq}^{l_1 l_2} = [(\text{rss}_{pql_1}, \text{rss}_{pql_2}), (\text{rss}_{p(q+1)l_1}, \text{rss}_{p(q+1)l_2})]$, which are the mapping data of $\mathbf{seg}_{ij}^{\text{rss}}$ and $\mathbf{seg}_{pq}^{\text{rss}}$ in the 2-dimensional space with respect to the l_1 -th and l_2 -th APs. To be clearer, the geometric definition of $\bar{d}_{\perp}^{l_1 l_2}$, $\bar{d}_{\parallel}^{l_1 l_2}$, and $\bar{d}_{\theta}^{l_1 l_2}$ is shown in Figure 6. As can be seen from this figure, the smaller N_{AP} -dimensional distance reflects the higher similarity of the RSS segments.

Based on the definition of N_{AP} -dimensional linear distance, the density based spatial clustering is conducted to merge the RSS linear segments corresponding to the similar motion patterns together. The pseudocode of density based spatial clustering is shown in Algorithm 2.

Finally, similar to physical logic graph, the RSS logic graph is constructed by selecting the RSS clusters and the corresponding transfer relations between them as the vertices and edges, respectively, where a transfer between any two RSS clusters is counted if and only if there is a pair of consecutive RSS segments falling into these two RSS clusters, respectively.

2.4. Hotspot Mapping between Physical and Signal Spaces.

With the PageRank algorithm [15], a PageRank (PR) value is distributed to each physical subarea and RSS cluster, and then the hotspot mapping is performed between the physical and signal spaces. To achieve this goal, we first count the transfer number between every two adjacent physical subareas, A_{η} and A_l , as $T_{\eta l}^A$ ($\eta, l \in \{1, \dots, N_{\text{area}}\}; \eta \neq l$), where N_{area} is the number of physical subareas, and calculate the transfer probability, $P_{\eta \rightarrow l}^A$, as

$$P_{\eta \rightarrow l}^A = \frac{T_{\eta l}^A}{\sum_{k=1}^{N_{\text{area}}} T_{\eta k}^A} \quad (5)$$

When the appearance probability of the pedestrian in A_{η} at the moment t is $P_t^A(A_{\eta})$, the appearance probability in A_l at the moment $t + 1$, $P_{t+1}^A(A_l)$ can be estimated by

$$P_{t+1}^A(A_l) = \sum_{\eta=1}^{N_{\text{area}}} P_t^A(A_{\eta}) P_{\eta \rightarrow l}^A \quad (6)$$

```

Input: RSS segments
Output: Signal clusters
(1)  $m = 1$ ; // Initialize the number of RSS clusters
(2) for (each RSS segment  $\mathbf{seg}_{ij}^{\text{RSS}}$ ) do // Data traversal
(3)   Calculate the  $N_{\text{AP}}$ -dimensional linear distance between  $\mathbf{seg}_{ij}^{\text{RSS}}$  and each of the rest RSS segments;
(4)   Save the RSS segments with the  $N_{\text{AP}}$ -dimensional linear distance smaller than a given threshold,  $e$ , into set  $C_{ij}$ ;
(5)   if (the number of elements in  $C_{ij}$  is not smaller than a given threshold,  $Min$ ) then
(6)     continue;
(7)   else
(8)     for (each RSS segment in  $C_{ij}$ ,  $\mathbf{seg}_{pq}^{\text{RSS}}$ ) do // Data traversal
(9)       if (the number of RSS segments in  $C_{pq}$  is not smaller than the threshold  $Min$ ) then
(10)        Merge  $C_{pq}$  into  $C_{ij}$ ;
(11)       else
(12)         continue;
(13)       end if
(14)     end for
(15)   Set  $C_{ij}$  as the  $m$ -th signal cluster;
(16)    $m \leftarrow m + 1$ ;
(17) end if
(18) end for

```

ALGORITHM 2: Pseudocode of spatial clustering.

As a special case, when a user is located in A_η at the moment t , he/she may enter an anonymous physical subarea at the next moment. In this case, we assume that the user is equally likely to appear in every physical subarea at the moment $t + 1$, such that

$$P_{t+1}^A(A_l) = \frac{1}{N_{\text{area}}} \quad (7)$$

Then, considering the movement trend of pedestrians in the target environment, the transfer relations between different physical subareas are obtained as follows [21]:

$$\mathbf{P}_{t+1}^A = \mathbf{Q}_A \mathbf{P}_t^A, \quad (8)$$

where

$$\begin{aligned} \mathbf{P}_t^A &= [P_t^A(1), \dots, P_t^A(N_{\text{area}})]^T, \\ \mathbf{P}_0^A &= \left[\frac{1}{N_{\text{area}}}, \dots, \frac{1}{N_{\text{area}}} \right]^T, \\ \mathbf{Q}^A &= \theta \left(\mathbf{P}^A + \frac{\mathbf{e}\mathbf{s}^T}{N_{\text{area}}} \right) + (1 - \theta) \frac{\mathbf{e}\mathbf{e}^T}{N_{\text{area}}}, \end{aligned} \quad (9)$$

and $\theta \in [0, 1]$ is the proportion of users satisfying the transfer relations in (6), $\mathbf{e} = [\frac{1}{N_{\text{area}}}, \dots, \frac{1}{N_{\text{area}}}]^T$, \mathbf{P}^A is a $N_{\text{area}} \times N_{\text{area}}$ matrix, in

which $P_{\eta \rightarrow l}^A$ is the element on the η th row and the l th column, and $\mathbf{s} = [s_1, \dots, s_{N_{\text{area}}}]^T$, in which the η th element satisfies

$$s_\eta = \begin{cases} 1, & \text{If } \sum_{l=1}^{N_{\text{area}}} T_{\eta l}^A = 0 \\ 0, & \text{Otherwise} \end{cases} \quad (10)$$

After that, the set of the PR values of physical subareas, $\mathbf{P}_{\text{hot}}^A$, is obtained as

$$\mathbf{P}_{\text{hot}}^A = \lim_{tz \rightarrow \infty} \mathbf{P}_{tz}^A = [P^A(1), \dots, P^A(N_{\text{area}})]^T \quad (11)$$

Similarly, in RSS logic graph, based on the transfer relations between different RSS clusters, we calculate the transfer frequency from the RSS clusters C_η to C_l as

$$P_{\eta \rightarrow l}^C = \frac{T_{\eta l}^C}{\sum_{k=1}^{N_{\text{cluster}}} T_{\eta k}^C}, \quad (12)$$

where $T_{\eta l}^C$ is the transfer number from C_η to C_l and N_{cluster} is the number of RSS clusters. Then, the set of the PR values of RSS clusters is obtained as

$$\mathbf{P}_{\text{hot}}^C = \lim_{tz \rightarrow \infty} \mathbf{P}_{tz}^C = [P^C(1), \dots, P^C(N_{\text{cluster}})]^T \quad (13)$$

Finally, we construct the sets of the ranked PR values of physical subareas and RSS clusters as $\mathbf{P}_{\text{Rank}}^A$ and $\mathbf{P}_{\text{Rank}}^C$, respectively, in (13).

$$\begin{aligned} \mathbf{P}_{\text{Rank}}^A &= [P_{\text{Rank}}^A(1), \dots, P_{\text{Rank}}^A(N_{\text{area}})]^T \\ \mathbf{P}_{\text{Rank}}^C &= [P_{\text{Rank}}^C(1), \dots, P_{\text{Rank}}^C(N_{\text{cluster}})]^T, \end{aligned} \quad (14)$$

where $P_{\text{Rank}}^A(1) \geq \dots \geq P_{\text{Rank}}^A(N_{\text{area}})$ and $P_{\text{Rank}}^C(1) \geq \dots \geq P_{\text{Rank}}^C(N_{\text{cluster}})$. Then, the RSS clusters are mapped into the physical subareas with same order of PR values. By considering that N_{cluster} is generally larger than N_{area} , the RSS clusters having no physical subarea to be mapped into are discarded in the process of hotspot mapping.

2.5. Localization and Behavior Analysis. In online phase, for each RSS data $\mathbf{rss}_j^{\text{new}} = [\text{rss}_{j1}^{\text{new}}, \dots, \text{rss}_{jN_{\text{AP}}}^{\text{new}}]$ in the newly

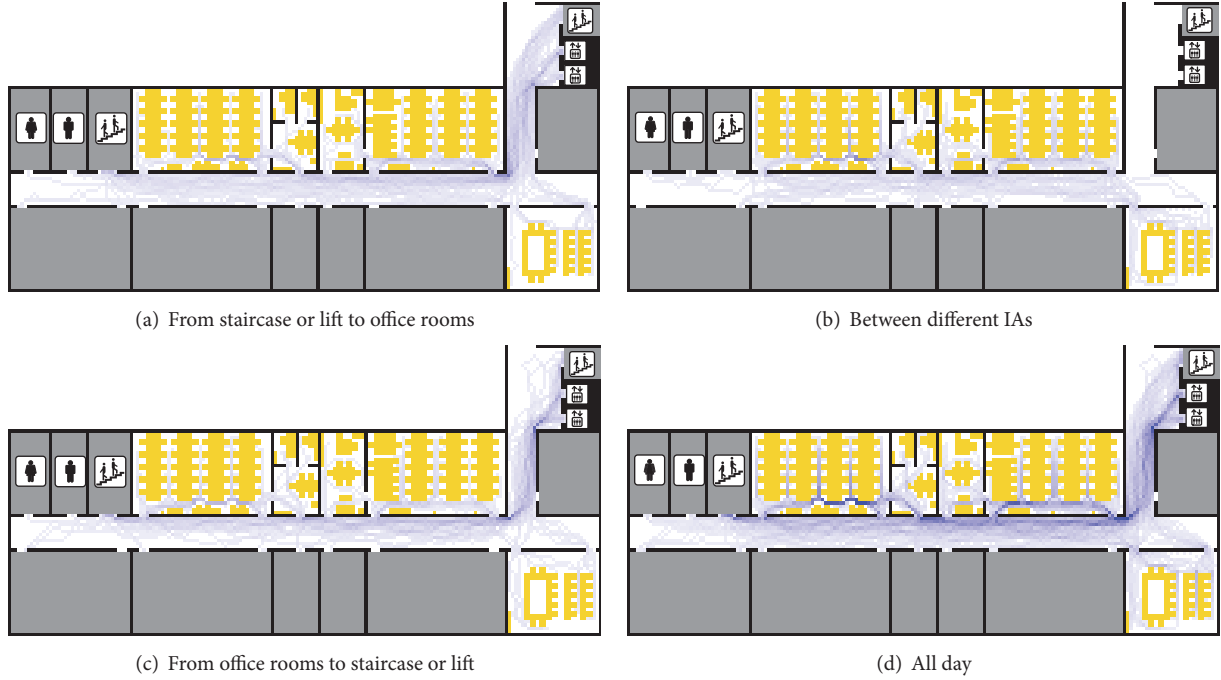


FIGURE 7: Motion paths construction.

collected RSS sequence, we calculate its confidence probability to each RSS cluster as

$$p_j^\eta = \prod_{l=1}^{N_{AP}} p_{lj}^\eta, \quad (15)$$

where p_{lj}^η ($\eta = 1, \dots, N_{\text{cluster}}$) is the confidence probability of the η th RSS cluster with respect to $\mathbf{rss}_j^{\text{new}}$ from the l th AP. Then, based on the established hotspot mapping relations between physical and signal spaces, the physical subarea corresponding to the RSS cluster with the highest confidence probability is chosen as the area where $\mathbf{rss}_j^{\text{new}}$ is most probably to be collected.

After that, according to the area-level localization results, we can analyze users' motion behavior in the target environment by calculating the activity frequency in each physical subarea, F_η^A , and the transfer probability between adjacent physical subareas, $M_{\eta \rightarrow l}^A$, as follows:

$$F_\eta^A = \frac{N_\eta^{\text{loc}}}{\sum_{k=1}^{N_{\text{area}}} N_k^{\text{loc}}}, \quad (16)$$

where N_η^{loc} is the number of the RSS data which are localized in the physical subarea A_k in the newly collected RSS sequence.

$$M_{\eta \rightarrow l}^A = \frac{T_{\eta l}^A}{\sum_{k=1}^{N_{\text{area}}} T_{\eta k}^A}, \quad (17)$$

where $T_{\eta l}^A$ is the number of the pairs of consecutive RSS data which are localized in the physical subareas A_η and A_l , respectively, in the newly collected RSS sequence.

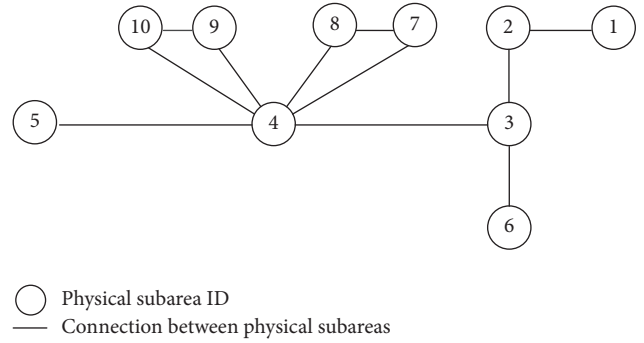


FIGURE 8: Physical logic graph.

3. Experimental Results

3.1. Result of Pedestrian Motion Learning. As shown in Figure 2, the target environment is divided into 10 physical subareas, notated as #1, ..., and #10. Then, based on the heuristic pedestrian motion learning approach, we define 20% pixels as the inaccessible ones and construct 300 motion paths in the transformed image of floor map. The result of simulated motion paths under different types of users' motion behavior is shown in Figure 7, where the pixels in darker color indicate the corresponding locations with higher appearance probabilities. As can be seen from this figure, 300 motion paths are capable of effectively describing the pedestrians' movement trend in the target environment. After that, according to the transfer relations of motion paths between different physical subareas in Figure 2, we construct the physical logic graph in Figure 8.

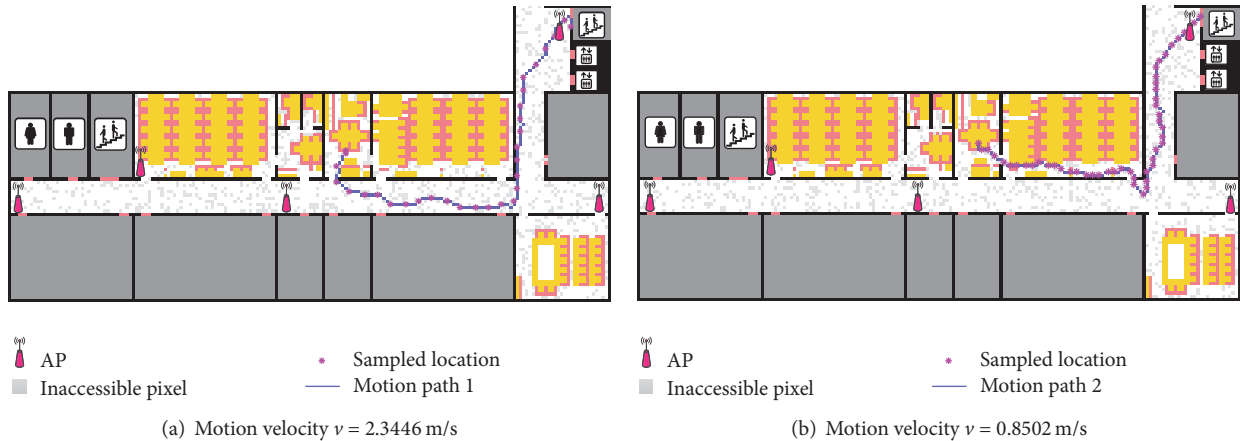


FIGURE 9: Sampled pixels on two motion paths with different motion velocity.

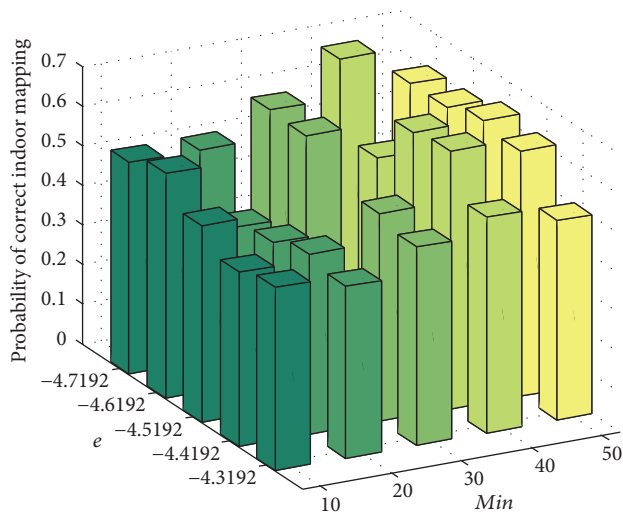


FIGURE 10: Probability of correct indoor mapping with different thresholds.

3.2. Result of Hotspot Mappings. According to the analysis of users' motion velocities [17], some specific pixels are labeled on each motion to calculate the RSS data from the placed APs as shown in Figure 9. This figure gives the result of pixel sampling under different motion velocities on the two constructed motion paths which are with the same starting and ending pixels.

Then, Figure 10 compares the probability of mapping the RSS data into the physical subareas which they actually belong to, namely, probability of correct indoor mapping. Since the defined N_{AP} -dimensional linear distance in formula (4) is sum of the normalized values of different distance measurements, the distance threshold e may be negative. As shown in Figure 10, the highest probability of correct indoor mapping is obtained when the thresholds e and Min are set as -4.7192 and 40 , respectively.

After obtaining the optimal thresholds corresponding to the highest probability of correct indoor mapping, we construct the signal logic graph in Figure 11. In our experiment,

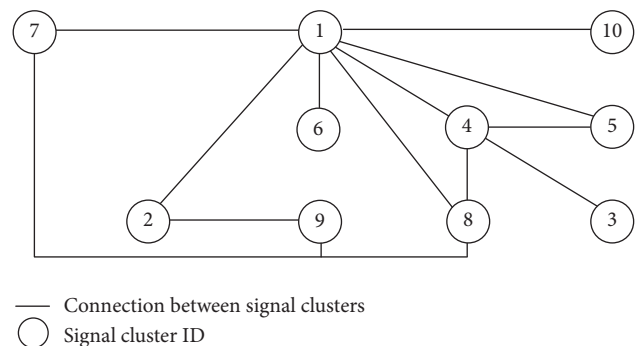


FIGURE 11: Signal logic graph.

TABLE 1: Comparison between different approaches.

Approach	Fingerprints calibration	Time complexity
[12]	No demand	$O(n)$
[13]	No demand	$O(n \times \log(n))$
[14]	Low calibration cost	$O(n^3)$
Proposed	No demand	$O(n \times \log(n))$

the proportion of the users satisfying the transfer relations in formula (6), θ , which is much larger than that of other users, is set as 90%. Based on this, the hotspot mapping between the physical and signal spaces is established in Figure 12.

3.3. Result of Localization and Behavior Analysis. To examine the localization performance of the proposed approach, we collect some calibrated RSS sequences in the consecutive one, two, and three physical subareas, respectively. Figure 13 shows the probabilities of locating the new RSS data into its actually belonging subarea which is defined as correct localization, as well as probabilities into its adjacent subareas which is defined as adjacently correct localization. In addition, combining with Table 1, we can find that compared with [12–14], the proposed approach can generally achieve higher localization accuracy with lower time complexity and without the demand for fingerprints calibration.

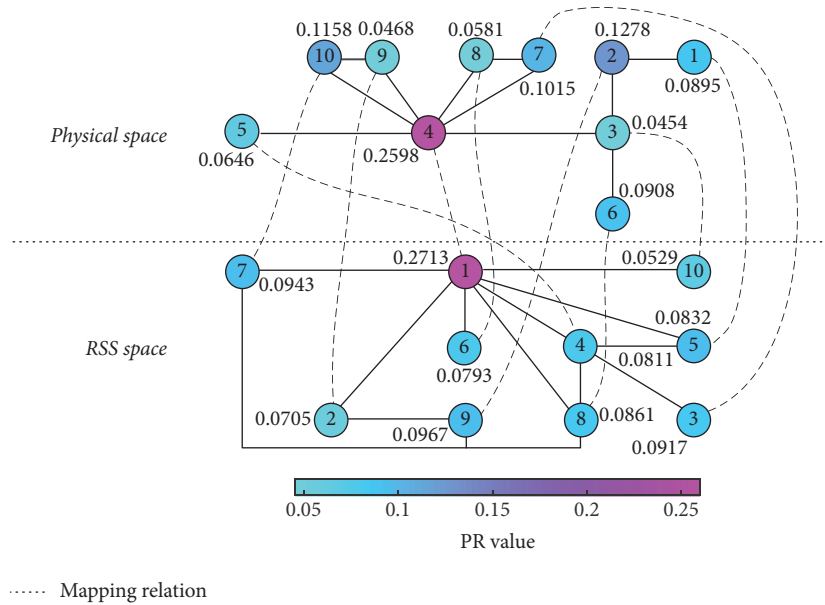


FIGURE 12: Hotspot mapping between physical and signal spaces.

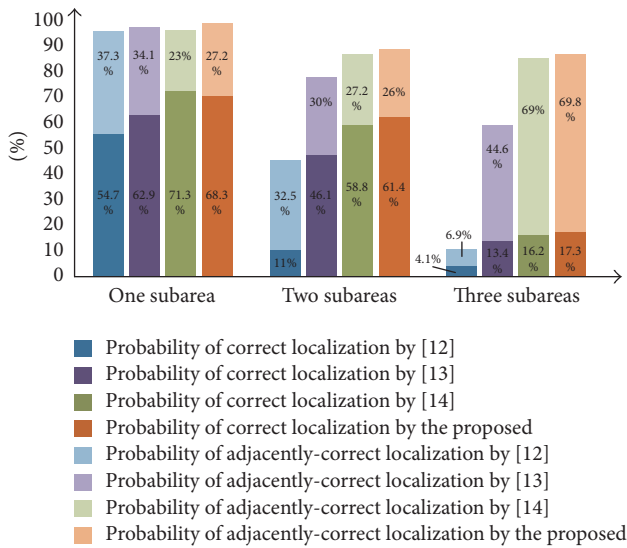


FIGURE 13: Localization result of different approaches.

Based on the area-level localization result, the users' motion behavior can be preliminarily analyzed by calculating the activity frequency in each subarea and the transfer probability between different physical subareas as shown in Figure 14. In this figure, the activity frequency in physical subarea #4 is much higher than the one in other subareas, which can be interpreted by the reason that #4 is with much larger PR value as illustrated in Figure 11. As a special case, the physical activity frequency is very low. This result is due to the fact that the similar RSS distributions in the physical subareas #1 and #2 increase the probability of mapping the RSS data in #2 into its adjacent physical subarea #1 by mistake.

At the same time, with the transfer probability between different physical subareas, we can further explore some

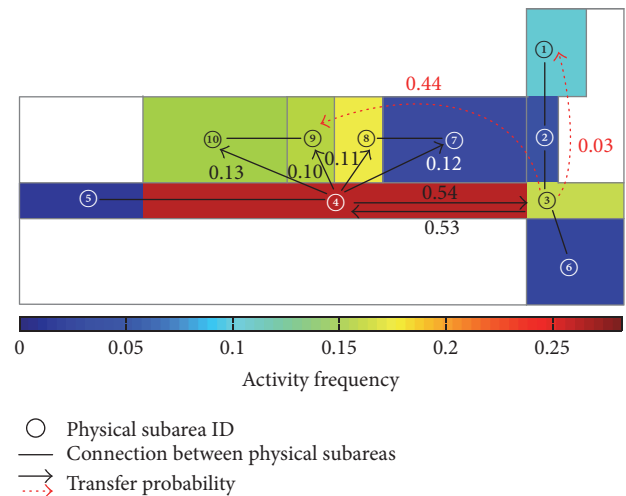


FIGURE 14: Motion behavior of users in the target environment.

users' motion preference in the target environment. As an example, when a user is located in the physical subarea #4, we can predict that he/she is most likely to move to subarea #3 with the confidence probability equalling 0.54. In addition, the nonzero transfer probability between the nonadjacent physical subareas (labeled with red dotted arrows) (i.e., #3 → #9 and #3 → #1 with the confidence probability 0.44 and 0.03, respectively) indicates that these nonadjacent physical subareas are with the similar RSS distributions.

4. Conclusion

In this paper, we propose a new pedestrian motion learning based indoor WLAN localization approach without the assistance of location fingerprinting or motion sensor. Combined with the pedestrian motion learning, density based spatial

clustering on RSS segments, and hotspot mapping strategy, we construct the hotspot mapping between the physical and signal spaces to estimate the target's location. In addition, the area-level localization result is utilized to explore the motion preference of pedestrians in indoor environment. In the future, we will pay more attention to the effective way of subareas division to enhance the hotspot mapping performance as well as reduce the wrong transfer probability between the nonadjacent physical subareas.

Conflicts of Interest

The authors declare that they have no conflicts of interest.

Acknowledgments

This work was supported in part by the National Natural Science Foundation of China (61771083, 61704015), Program for Changjiang Scholars and Innovative Research Team in University (IRT1299), Special Fund of Chongqing Key Laboratory (CSTC), Fundamental and Frontier Research Project of Chongqing (cstc2017jcyjAX0380, cstc2015jcyjBX0065), University Outstanding Achievement Transformation Project of Chongqing (KJZH17117), and Postgraduate Scientific Research and Innovation Project of Chongqing (CYSI7221).

References

- [1] M. Zhou, Y. Wei, Z. Tian, X. Yang, and L. Li, "Achieving cost-efficient indoor fingerprint localization on wlan platform: a hypothetical test approach," *IEEE Access*, vol. 5, pp. 15865–15874, 2017.
- [2] M. Zhou, Y. Tang, Z. Tian, L. Xie, and W. Nie, "Robust neighborhood graphing for semi-supervised indoor localization with light-loaded location fingerprinting," *IEEE Internet of Things Journal*, vol. PP, no. 99, pp. 1-1, 2017.
- [3] A. Yaeli, P. Bak, G. Feigenblat et al., "Understanding customer behavior using indoor location analysis and visualization," *IBM Journal of Research and Development*, vol. 58, no. 5/6, pp. 3:1–3:12, 2014.
- [4] X. Zhai, J. Yang, and L. Cui, "Wireless network localization via alternating projections with TDOA and FDOA measurements," *Ad Hoc & Sensor Wireless Networks*, vol. 38, no. 1-4, pp. 1–20, 2017.
- [5] P. Bahl and V. N. Padmanabhan, "RADAR: an in-building RF-based user location and tracking system," in *Proceedings of the 19th Annual Joint Conference of the IEEE Computer and Communications Societies (IEEE INFOCOM '00)*, vol. 2, pp. 775–784, Tel Aviv, Israel, March 2000.
- [6] M. Youssef and A. Agrawala, "The Horus WLAN location determination system," in *Proceedings of the 3rd International Conference on Mobile Systems, Applications, and Services (MobiSys '05)*, pp. 205–218, ACM, June 2005.
- [7] C. Koweerawong, K. Wipusitwarakun, and K. Kaemarungsi, "Indoor localization improvement via adaptive RSS fingerprinting database," in *Proceedings of the 27th International Conference on Information Networking, ICOIN 2013*, pp. 412–416, January 2013.
- [8] M. W. M. G. Dissanayake, P. Newman, S. Clark, H. F. Durrant-Whyte, and M. Csorba, "A solution to the simultaneous localization and map building (SLAM) problem," *IEEE Transactions on Robotics and Automation*, vol. 17, no. 3, pp. 229–241, 2001.
- [9] H. Shin, Y. Chon, and H. Cha, "Unsupervised construction of an indoor floor plan using a smartphone," *IEEE Transactions on Systems, Man, and Cybernetics, Part C: Applications and Reviews*, vol. 42, no. 6, pp. 889–898, 2012.
- [10] L. Bruno and P. Robertson, "WiSLAM: improving FootSLAM with WiFi," in *Proceedings of the International Conference on Indoor Positioning and Indoor Navigation (IPIN '11)*, pp. 1–10, Guimarães, Portugal, September 2011.
- [11] P. Robertson, M. Angermann, and B. Krach, "Simultaneous localization and mapping for pedestrians using only foot-mounted inertial sensors," in *Proceedings of the 11th International Conference on Ubiquitous Computing (UbiComp '09)*, pp. 93–96, ACM, Orlando, Fla, USA, 2009.
- [12] C. Wu, Z. Yang, Y. Liu, and W. Xi, "WILL: wireless indoor localization without site survey," *IEEE Transactions on Parallel and Distributed Systems*, vol. 24, no. 4, pp. 839–848, 2013.
- [13] X. Zhang, Y. Jin, H. Tan, and W. Soh, "CIMLoc: a crowdsourcing indoor digital map construction system for localization," in *Proceedings of the IEEE Ninth International Conference on Intelligent Sensors, Sensor Networks and Information Processing (ISSNIP '14)*, pp. 1–6, Singapore, April 2014.
- [14] Q. Zhang, M. Zhou, Z. Tian, and Y. Wang, "Indoor localization using semi-supervised manifold alignment with dimension expansion," *Applied Sciences (Switzerland)*, vol. 6, no. 11, Article ID 338, 2016.
- [15] Z. Ji-Lin, R. Yong-jian, Z. Wei, X. Xiang-Hua, W. Jian, and W. Yu, "Webs ranking model based on pagerank algorithm," in *Proceedings of the 2010 2nd International Conference on Information Science and Engineering (ICISE)*, pp. 4811–4814, Hangzhou, China, December 2010.
- [16] M. Zhou, Y. Wang, Z. Tian, and Q. Zhang, "Indoor pedestrian motion detection via spatial clustering and mapping," *IEEE Sensors Letters*, vol. 2, no. 1, pp. 1–4, 2018.
- [17] T. S. Azevedo, R. L. Bezerra, C. A. Campos, and L. F. de Moraes, "An analysis of human mobility using real traces," in *Proceedings of the 2009 IEEE Wireless Communications and Networking Conference*, pp. 1–6, Budapest, Hungary, April 2009.
- [18] F. Lopes, A. B. Costa, and H. S. Gomes, "Empirical ARMA indoor propagation model for WLAN signals in 2.4 GHz," in *Proceedings of the IEEE European Conference on Antennas and Propagation*, pp. 1338–1341, 2013.
- [19] P. Chai and L. Zhang, "Indoor radio propagation models and wireless network planning," in *Proceedings of the IEEE International Conference on Computer Science and Automation Engineering (CSAE '12)*, pp. 738–741, May 2012.
- [20] K. Kaemarungsi and P. Krishnamurthy, "Properties of indoor received signal strength for WLAN location fingerprinting," in *Proceedings of the 1st Annual International Conference on Mobile and Ubiquitous Systems: Networking and Services (MOBIQUITOUS '04)*, pp. 14–23, August 2004.
- [21] X. Zhai, L. Zheng, J. Wang, and C. W. Tan, "Optimization algorithms for epidemic evolution in broadcast networks," in *Proceedings of the 2013 IEEE Wireless Communications and Networking Conference, WCNC 2013*, pp. 1540–1545, April 2013.

Research Article

Multilayer Learning Network for Modulation Classification Assisted with Frequency Offset Cancellation in Satellite to Ground Link

Guan Qing Yang 

College of Electronic and Information Engineering, Shenyang Aerospace University, Shenyang 110136, China

Correspondence should be addressed to Guan Qing Yang; guan.qy@163.com

Received 18 September 2017; Revised 27 February 2018; Accepted 31 March 2018; Published 10 May 2018

Academic Editor: Ioannis Krikidis

Copyright © 2018 Guan Qing Yang. This is an open access article distributed under the Creative Commons Attribution License, which permits unrestricted use, distribution, and reproduction in any medium, provided the original work is properly cited.

A multilayer learning network assisted with frequency offset cancellation is proposed for modulation classification in satellite to ground link. Carrier frequency offset greatly reduces modulation classification performance. It is necessary to cancel frequency offset before modulation classification. Frequency offset cancellation weights are established through multilayer learning network based on MSE criterion. Then the weight and hidden layer of multilayer learning network are also established for modulation classification. The hidden layers and weight are trained and tuned to combat the interference introduced by frequency offset. Compared with current modulation classification algorithm, the proposed multilayer learning network greatly improves the Probability of Correct Classification (PCC). It has been proven that the proposed multilayer learning network assisted with frequency offset has higher performance for modulation classification within the same training sequence.

1. Introduction

Satellite to ground link adopts different modulation technology to satisfy different requirement. With rapid development of communication technology, modulation classification for satellite communication becomes an important research topic in signal recognition, especially in larger frequency offset environment [1–3].

Doppler frequency offset exists between users and satellite, and it greatly damages the link performance and especially affects modulation classification. As satellite is moving at high speed, frequency offsets are also changing. This process requires that modulation classification should overcome frequency offsets within larger SNR dynamic range. So it is very important to adopt frequency offset cancellation method for modulation classification.

In early research work, the literatures were researching on cancellation algorithms for frequency offsets, which were estimated at receivers and then sent back to respective transmitter. But this is not suitable for long-distance transmission in satellite to ground link. Reference [4] analyzed single user in earliest frequency offset cancellation algorithm. Least

squares (LS) and minimum mean-square error (MMSE) were applied in [5]. LS method required frequency offset, while MMSE algorithm required noise powers as well. Reference [6] proposed an iterative cancellation for canceling frequency offset interference, which should need large complex iterations. Huang gave frequency offsets cancellation method using circular convolution in [7], which should need relatively large complexity.

Reference [8] proposed an alternative method in time-domain method for frequency offset compensation, but the precision was not very satisfactory. Reference [9] proposed a joint iterative detection algorithm, which should require ICI matrix inversion in each iteration. In [10], successive interference cancellation (SIC) algorithm was proposed to cancel frequency offset interference. The interference was cancelled by reconstructing signals. SIC algorithm depending on power order was proposed in [11]. Reference [12] gave SIC algorithm based on the signal-to-interference-plus-noise ratio (SINR) order. Reference [13] proposed an iterative parallel interference canceller (PIC) solution. Based on this, selective parallel interference cancellation (SPIC) algorithm was presented in [14] but had a significant implementation

complexity. Based on signal-to-interference ratio (SIR) analyzing, a parallel interference canceller for mitigation of interference due to CFOs was presented in [15].

Modulation classification for communication signal in satellite link is the multivariate pattern classification problem with multiple unknown parameters. Modulation classification algorithms should extract the feature from sampling signal. These algorithms can be classified into the following 5 types.

Type 1 Histogram Features. In 1984, Liedtke et al. proposed a pattern recognition method to classify digital modulated signals. Liedtke et al. used amplitude histogram, frequency histogram, and phase histogram as characteristic parameters. Too many feature dimensions lead to larger computational complexity. However, reducing feature dimensions would affect the ability of different modulation classification with similar distribution functions.

Type 2 Statistical Cumulant Features. In view of the larger number of histogram features, literature [16] proposed a sixth-order cumulants feature in order to improve the performance. However, the sixth-order cumulants algorithm was only based on the energy model, which was not effective for frequency offset. In [17–19], cyclic high-order cumulants were obtained for modulation classification, and the performance in the Gaussian white noise channel was given. But the performance in large frequency offset status was not considered. References [20, 21] used high-order cumulant feature for modulation classification. These feature extraction operations were relatively easy to obtain. However, computational complexity for higher-order cumulants was improved. As modulation classification algorithms obtained features based on cumulants, classification performance within larger frequency offset was not in consideration.

Asoke K. Nandi and EEAZzouz et al. used the statistical features of instantaneous envelope, phase, and frequency of signal data and applied decision theory for modulation classification [22, 23]. A similar algorithm was proposed by Chan and Gadbois. According to the features of the signal envelope, the ratio of the signal envelope variance to the signal mean square was used as the decision criterion [24]. Louis used digital signals such as 2FSK, 4FSK, 8FSK, OQPSK, MSK, BPSK, QPSK, 8PSK, 16QAM, 64QAM, and other digital signals based on instantaneous frequency, phase, and amplitude [17]. Swami adopted normalized cumulative power of the symbol-synchronous sampling sequence to classify QAM, PSK, ASK, and other signals [20]. In 2001, Wong and Nandi [25] used statistical cumulant and spectral features in classification.

Type 3 Transformation Feature Criterion. Cumulant features for satellite signal are only to identify several common modulations. In addition to directly using the statistical parameters and the histogram as a classification feature, the signal can be transformed into other feature spaces and the satellite data analysis can be accomplished by using the feature parameters in the new feature space. With the development of signal processing theory, the signal could be transformed

into various forms. Wavelet transformation feature for modulation classification was proposed in [26]. Haar wavelet feature transform had better antinoise features than the high-order cumulants. But it had weak anti-frequency offset features. In [27], modulation classification algorithm based on cycle spectrum features was proposed. Based on extending this algorithm, modulation classification algorithm based on bispectrum feature was used to classify MPSK signal in [28]. In [29], wavelet packet was proposed, which was decomposed by the wavelet packet. The partial decomposition vector of the average energy was obtained. Then average energy was arranged in a certain order to construct classification feature. In [30], MFSK and MPSK are classified through wavelet transform, and better PCC was obtained when the SNR was greater than 6 dB. In [31], an automatic classification algorithm based on spectral analysis was proposed, which used the statistical characteristics assisted with maximum likelihood estimator.

Type 4 Bayesian Classification Criterion. A classical method for modulation classification is the maximum likelihood method. Modulation classification is obtained through maximum likelihood function. In [32], MPSK signal based on phase maximum likelihood function was proposed. In [33], a joint likelihood function using amplitude and phase was proposed within larger SNR, and it was on the premise that the amplitude and phase were assumed to be independent. In [34], classification for MFSK signal was discussed. After averaging the unknown parameters in the average likelihood function, the integral expression of zero-order modified Bessel function was obtained. The high-order correlation analysis based on Bessel function was derived for modulation classification. In literature [35], a generalized likelihood ratio function for classification framework was proposed, which firstly expanded the power for the likelihood ratio function and then made the expected average processing for the unknown parameters and then formed the classification statistics based on higher correlation order.

The advantage of transformation domain theory for modulation classification is theoretically guaranteeing that the result is optimal under Bayesian cost criterion. The classification performance curve can be obtained by theoretical analysis. The likelihood ratio performance can be used as a theoretical upper limitation. Of course, the maximum likelihood algorithm also has limitations and shortcomings. Firstly, compared to the modulation classification method, it requires more a priori knowledge, such as the form of the distribution function including the mean, variance, and signal-to-noise ratio. Secondly, the existence of unknown parameters results in the complex calculation, which is also difficult for real-time processing.

In order to cancel frequency offset, the eigenvalue is very limited to suppress the noise based on Bayesian classification criterion. Current methods such as feature extraction, classification, and regression can be used as shallow structure algorithms. These methods are limited to complex functions in finite samples and computational units, and their generalization ability is restricted to complex classification problems.

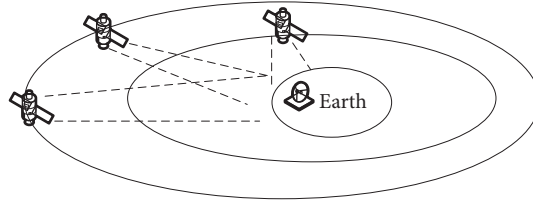


FIGURE 1: Satellite beam enters the target ground station antenna range.

Type 5 Multilayer Neural Network. With improvement of artificial intelligence, researchers introduced multilayer neural network algorithms for modulation classification. Multilayer learning could represent the input data distribution by learning a multilayer nonlinear network structure and implementing complex function approximation. The multilayer learning motivation lies in the establishment of a neural network, which could simulate the human brain for signal analysis and mimic human brain mechanisms to interpret the data.

Multilayer learning algorithms obtain data features by building models with multiple hidden layers to improve classification or prediction accuracy. Multilayer learning algorithm is different from the traditional shallow learning structure; the difference in multilayer learning lies in the following: (1) emphasizing the depth of the model structure usually with many hidden nodes and (2) the importance of feature learning being clearly highlighted. By layer-by-layer feature transformation, the feature of data in the original space is transformed into a new feature space to make classification or prediction easier. Compared with the method of constructing data features manually, the use of data to learn features can better express intrinsic information. Identification part needs to determine the appropriate decision rules and classifier structure.

Common classifiers include tree structure classifiers [36, 37], neural network classifiers [38, 39], and support vector machine classifiers [40, 41]. The tree structure classifier used a multilevel classifier structure, each structure according to one or more of the characteristic parameters. Neural network classifier uses different structures of artificial neural network for a variety of ways to achieve training and testing. SVM classifier inputs feature vector into high-dimensional space and constructs the optimal classification in the high-dimensional space to achieve data classification. In [42], a classifier based on tree structure was adopted. The multilevel tree classifier structure is based on one or more feature parameters. In [43], a multilayer clustering algorithm is used for modulation classification. In [44], K -nearest neighbor algorithm classifier was used to identify modulation mode. Literature [45] used the distance distribution function to optimize and obtain better classification performance. However, this algorithm did not give analysis in larger frequency offset. In [46], an improved KNN multilayer learning architecture was proposed to classify modulation. However, this algorithm was applicable for Gaussian white noise channel environment, and the performance of the algorithm was limited for larger frequency offset.

2. System Model and Problem Formulation

2.1. Satellite to Ground Link Model. Due to high-speed movement of the satellite, the satellite to ground link is established between station and satellite. In this process, it is necessary to accurately calculate the constellation. The process has been shown in Figure 1. In this process, frequency offset of the satellite to ground link is changing, so it is necessary to accurately cancel the interference of frequency offset before modulation classification.

We establish the satellite to ground link communication model. Ossanna has firstly proposed the probability statistical model of satellite to ground link in 1964 [47]. The principle is based on the reflection wave interference, so the angle of reflection is limited. It is fuzzy to use this satellite ground to link model to describe the rural and urban areas. Clarke proposed in 1968 statistical model [48] based on the principle of scattering signal strength, but the model needed to assume that the incident wave formation was the same, so the application of the model was limited. After the 70s, according to the measured data in Canada, Loo proposed a statistical model based on [49]. If the shadow fading follows the Nakagami distribution, the Abdi star fading model is formed [50]. So, it is common for satellite to use probability density function, such as Rician model, Loo model, and Rician-Lognormal model. The scene for the satellite to ground communication system is mainly urban environment, and most of signal transmission has direct path.

2.2. Signal Processing Model. The n th received frame can be written as

$$x(n) = d(n) * h(n), \quad n = 1, \dots, N, \quad (1)$$

where $h(n)$ represents channel impulse response at instant n . At the receiver, frequency offset is induced into the baseband signal due to Doppler frequency and the clock oscillator misalignment between the satellite and user. The baseband signal could be given as

$$s(n) = x(n) e^{j2\pi n \xi / N} + z(n), \quad n = 1, \dots, N, \quad (2)$$

where ξ denotes frequency offset (FO) normalized by the subcarrier spacing and $z(n)$ is the additive white Gaussian noise with zero mean and σ^2 variance.

As shown in Figure 2, the multipath fading satellite communication signal should pass through the downconversion sampling block. Signal-to-noise ratio should be estimated

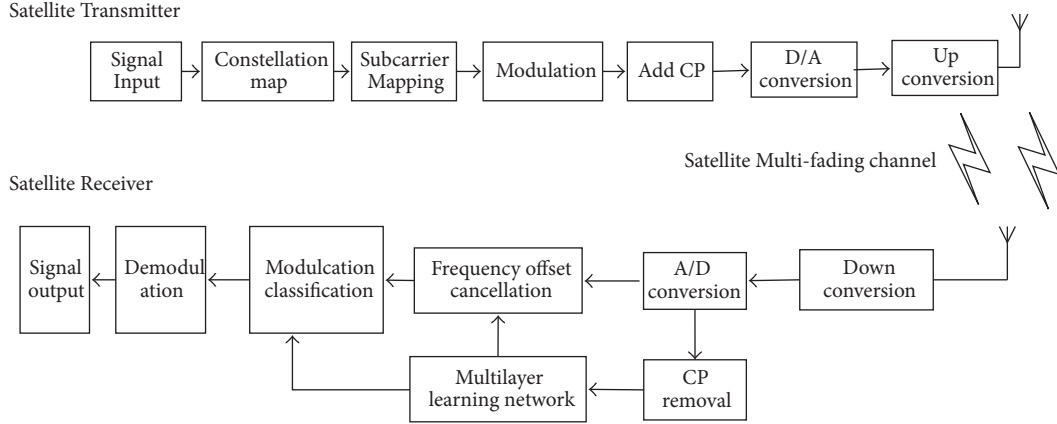


FIGURE 2: Signal processing block diagram in satellite to ground communication link.

firstly, and then signal enters into the frequency offset and modulation classification block based on multilayer learning network. After the corresponding demodulation and decoding, the information can be adopted finally.

3. Multilayer Learning Network for Modulation Classification Assisted with Frequency Offset Cancellation

3.1. Motivation of Multilayer Learning Network. The optimization goal of modulation classification for satellite communication signal with frequency offset is the minimum mean square (MSE) between the received signal $r(n)$ with carrier frequency offset and the expected output signal, which could be expressed as $\min \|r(n) - s(n)\|^2$.

This equation implicates that the optimization cost function exhibits a strong nonlinear behavior. So it is hard to solve the problem with linear method. Reference [16] also involved a nonlinear regression problem that is also hard to solve. Therefore, in the present work, a nonlinear weight solution method based on multilayer learning network is proposed to solve the nonlinearity problem.

Due to carrier frequency offset interference existing, it seriously influences modulation classification for satellite communication signal. In accordance with the signal processing flow, the proposed multilayer learning network is divided into two parts as shown in Figure 3. The first part is carrier frequency offset cancellation module, and the second part is modulation classification module. Carrier frequency offset module can greatly improve the probability of correct classification for the modulation classification.

Multilayer neural network mechanism for frequency offset interference and modulation mode classification are trained separately.

Due to the formation principle of frequency offset interference in satellite communication system, the required multilayer neural network mechanism for frequency offset interference and modulation mode classification are different. And the weights required by the frequency offset interference cancellation neural network and modulation mode

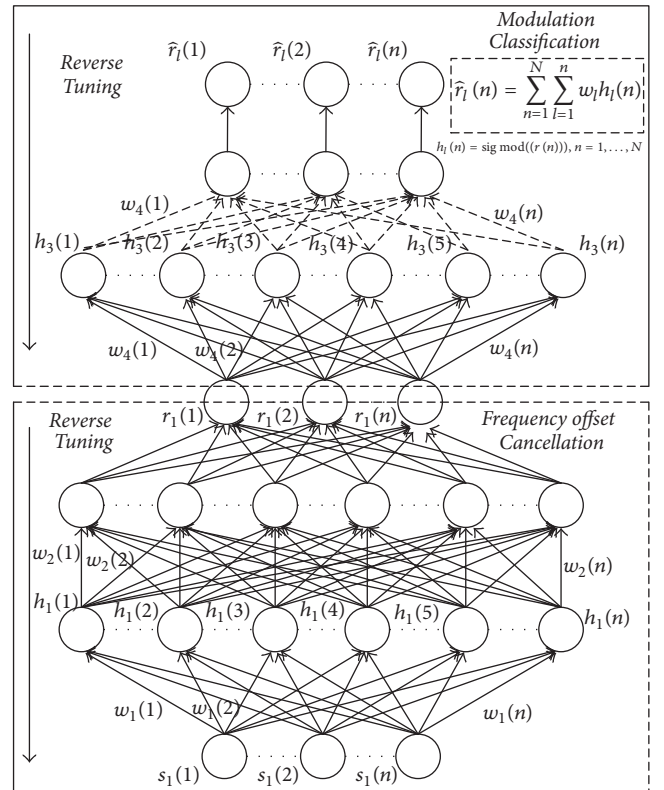


FIGURE 3: Signal processing flow of multilayer learning network for modulation classification of assisted frequency offset cancellation.

classification neural network are greatly different. Therefore, two cascaded neural networks are separately trained and reversely tuned with the same training sequence being used.

3.2. Framework for Communication Signals. Before introducing the multilayer learning network, the framework for communication signal is defined below. Figure 4 shows the defined typical framework, which includes the training symbols and data symbols. The training symbols are known

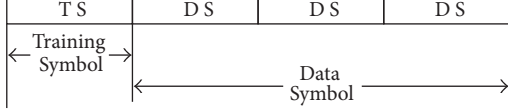


FIGURE 4: Framework for communication signals.

by both the transmitter and the receiver, which are also considered as reference symbols. In other words, every training symbol is already known by the receiver. The multilayer learning network can be trained with convergence by training symbols, and the trained network with the optimal weight can be used for frequency offset cancellation and modulation classification.

4. Multilayer Learning Network for Frequency Offset Cancellation

4.1. Processing Flow for Carrier Frequency Offset Cancellation.

It is effective to obtain optimum weights of multilayer learning network through iterative training symbols. Figure 5 is obtained by $s(n)$ passing through the two-layer learning network with weight $w(n)$, where $s_1(n)$ represents the input signal for the first layer learning network and $s_2(n)$ represents the input signal for the second layer network. Here, we use two layers for frequency offset cancellation. For current analysis, more layers are not able to obviously improve the performance. The relevant theoretical analysis will be given later. N is defined as the length of symbols for input. L is defined as the training symbols, which can be known by the transmitter and the receiver. After multilayer learning networks are trained adaptively through these symbols, weights will converge. In practice, $L \ll N$.

4.2. First Layer for Carrier Frequency Offset Cancellation. We define cost function as

$$J(n) = \sum_{n=1}^N \|s(n) - r(n)\|^2 + \lambda^n \cdot \|w(n)\|^2, \quad (3)$$

where λ is exponential weighting factor and is defined as a positive constant value less than unit. $w_1(n)$ represents the weight for the first layer learning network and $w_2(n)$ represents the weight for the second layer network. $r_1(n)$ represents the output for the first layer network and $r_2(n)$ represents the output for the second layer network.

We further could obtain through the first layer

$$J(n) = \sum_{n=1}^N \|s_1(n) - w_1^*(n) \cdot s_1(n)\|^2 + \lambda^n \cdot \|w_1(n)\|^2. \quad (4)$$

Optimization goals for weight w can be expressed as

$$w^* = \arg \min_{w \in \mathbb{C}^{N \times k}} J(n). \quad (5)$$

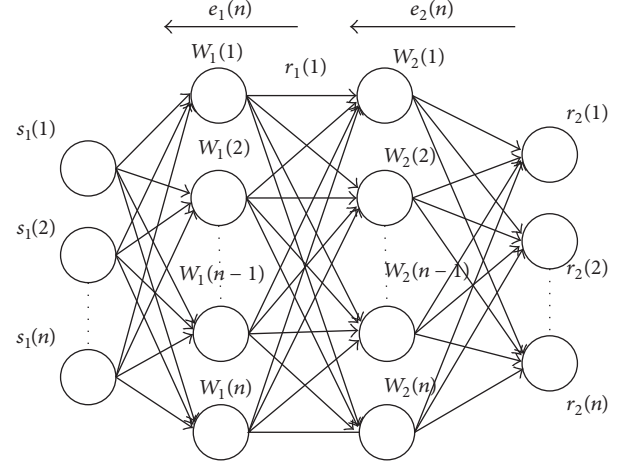


FIGURE 5: Signal processing flow of multilayer learning network for frequency offset cancellation.

$e_1(n)$ is defined as the reverse tuning error for the first layer, which is between the n th reference symbol and n th received symbol. We could obtain

$$e_1(n) = r_1(n) - w_1^*(n) s_1(n). \quad (6)$$

The gradient vector for cost function with respect to $w_1(n)$ can be derived as

$$\frac{\partial J(n)}{\partial w_1(n)} = 0. \quad (7)$$

After some simple mathematic manipulation, we could obtain

$$w_1(n) = \left[\sum_{n=1}^N s_1(n) s_1^*(n) + \lambda^n I \right]^{-1} \cdot \left[\sum_{n=1}^N s_1(n) s_1^*(n) \right]. \quad (8)$$

Define

$$H(n) = \sum_{n=1}^N s_1(n) s_1^*(n) + \lambda^n I. \quad (9)$$

Note that (9) may be rewritten into the iterative form:

$$H(n) = \left[\sum_{n=1}^{N-1} s_1(n) s_1^*(n) + \lambda^{n-1} I \right] + s_1(n) s_1^*(n), \quad (10)$$

$$H(n) = \lambda H(n-1) + s_1(n) s_1^*(n).$$

We could also obtain $w_1(n)$ in iterative form:

$$w_1(n+1) = w_1(n) + H^{-1}(n) s_1(n) e_1^*(n). \quad (11)$$

Substituting $e^{j2\pi\xi n/N}$ into (6), we finally get

$$\begin{aligned} e_1(n) &= s_1(n) - r_1(n) \\ &= s_1(n) - s_1(n) \cdot e^{j2\pi\xi n/N} \cdot w^*(n) \\ &= s_1(n) \cdot \left[1 - e^{j2\pi\xi n/N} \cdot w^*(n) \right], \end{aligned} \quad (12)$$

where

$$\begin{aligned}
s_1(n) e^*(n) &= C \cdot \left[e^{j2\pi n \xi / N} - w_1(n) \right], \\
C &= s(n) \cdot s^*(n), \quad n > 1 \\
H_1^{-1}(n) &= \left[\sum_{n=1}^N s_1(n) s_1^*(n) + \lambda^n I \right]^{-1} \\
&= \left[\sum_{n=1}^N s_1(n) \cdot e^{j2\pi n \xi / N} s_1^*(n) \cdot e^{-j2\pi n \xi / N} + \lambda^n I \right]^{-1} \\
&= D.
\end{aligned} \tag{13}$$

After manipulation, we could obtain that C is also a constant value.

Updating $w(n)$, we obtain

$$\begin{aligned}
w_1(n+1) &= w_1(n) + C e^*(n) \cdot s_1(n) \\
&= w_1(n) + CD \cdot \left[e^{j2\pi n \xi / N} - w_1(n) \right] \\
&= (1 - CD) w_1(n) + CD \cdot e^{j2\pi n \xi / N}, \\
w_1(n) &= (1 - CD)^n \cdot w_1(0) + CD \cdot (1 - CD)^{n-1} \\
&\quad \cdot \sum_{n=1}^{N-1} (1 - CD)^{-n} \cdot e^{j2\pi n \xi / N}, \quad n > 0.
\end{aligned} \tag{14}$$

Taking the limit, we could obtain

$$w_\infty = \lim_{n \rightarrow \infty} w(n) = \frac{CD}{e^{j2\pi \xi / N} - (1 - CD)} e^{j2\pi n \xi / N}. \tag{15}$$

After mathematical operation, the first layer output will be obtained as

$$\begin{aligned}
r_1(n) &= w_\infty^* \cdot s_1(n) \\
&= \frac{CD}{e^{-j2\pi \xi / N} - (1 - CD)} e^{-j2\pi n \xi / N} \cdot x(n) \\
&\quad \cdot e^{j2\pi n \xi / N} = \frac{CD}{e^{-j2\pi \xi / N} - (1 - CD)} \cdot s_1(n) \\
&= T \cdot x(n),
\end{aligned} \tag{16}$$

where

$$T = \frac{CD}{e^{-j2\pi \xi / N} - (1 - CD)}. \tag{17}$$

From (17), we can obtain that the output has the product of $s_1(n)$ and $e^{-j2\pi n \xi / N}$, and the input symbol $s_1(n)$ can be compensated with weights of multilayer learning network. When $\xi \ll 1$, we could obtain that $T \ll 1$. So we have that the interference induced by F could be ignored. If the frequency offset ξ is so large, F would induce the residual frequency offset, which could also destroy the output signal $s_2(n)$. So we establish the second layer for residual frequency offset cancellation.

ζ is defined as the residual interference, which is caused by interference part T . We could also get this result from constellation simulation as shown in Figure 7. This disturbance also causes the phase rotation of ideal signal, so signal passing through the first layer could be expressed as

$$s_2(n) = x(n) \cdot e^{j2\pi \zeta / N} + w(n), \tag{18}$$

where ζ is the residual frequency offset; $e^{j2\pi \zeta / N}$ could only induce the phase rotation for $s_2(n)$.

4.3. Second Layer for Carrier Residual Frequency Offset Cancellation. The second layer for signal processing is similar to the first layer.

Updating $w_2(k)$,

$$\begin{aligned}
w_2(k+1) &= w_2(k) + B e_2^*(k) \cdot Y(k) \\
&= w_2(k) + BC \cdot \left[e^{j2\pi \zeta / N} - w_2(k) \right] \\
&= (1 - BC) w_2(k) + BC \cdot e^{j2\pi \zeta / N},
\end{aligned} \tag{19}$$

where

$$\begin{aligned}
H_2^{-1}(n) &= \left[\sum_{n=1}^N s_2(n) s_2^*(n) + \lambda^n I \right]^{-1} \\
&= \left[\sum_{n=1}^N s_2(n) \cdot e^{j2\pi n \xi / N} s_2^*(n) \cdot e^{-j2\pi n \xi / N} + \lambda^n I \right]^{-1} \\
&= B.
\end{aligned} \tag{20}$$

After manipulation, we could obtain that B is also a constant value.

$$\begin{aligned}
w_2(n) &= (1 - BC)^n \cdot W(0) + BC \cdot (1 - BC)^{n-1} \\
&\quad \cdot \sum_{n=0}^{N-1} (1 - BC)^{-n} \cdot e^{\frac{j2\pi \zeta}{N}}, \quad n \geq 0.
\end{aligned} \tag{21}$$

Taking the limit, we will obtain

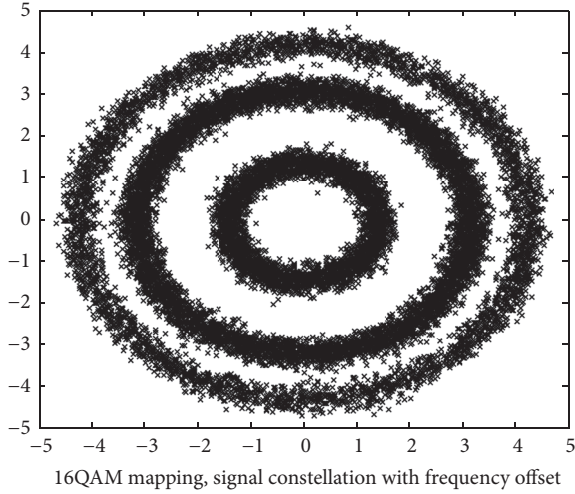
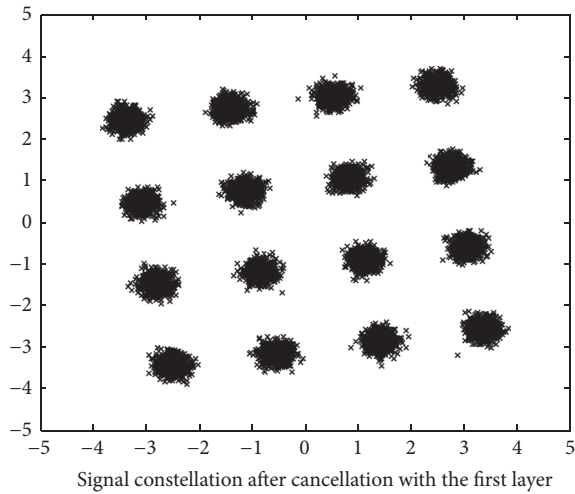
$$w_2 = \lim_{n \rightarrow \infty} w(n) = \frac{BC}{1 - (1 - BC)} e^{j2\pi \zeta / N} = e^{j2\pi \zeta / N}. \tag{22}$$

At the high SNR, the noise can be ignored; the output signal will be

$$r(n) = w_2^* \cdot s_2(n) = e^{-j2\pi \zeta / N} \cdot x(n) \cdot e^{j2\pi \zeta / N} = x(n). \tag{23}$$

From (23), we can obtain that the output has the product of $s_2(n)$ and $e^{-j2\pi \zeta / N}$; we could get the signal $x(n)$ with non-frequency offset. We therefore conclude that the symbol $s_2(n)$ with residual frequency offset can be compensated with second layer of multilayer learning network completely.

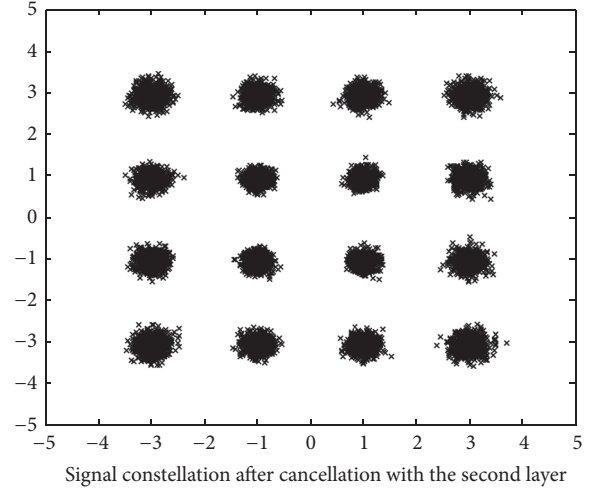
The performance for frequency offset cancellation of multilayer learning network could be obtained by the constellation simulation. Consider that SNR is 20 dB and the number of subcarriers is set as 256. Figure 6 gives out the


 FIGURE 6: Signal constellation with frequency offset $\xi = 0.3$.

 FIGURE 7: Signal constellation after cancellation with first layer of multilayer learning network, with frequency offset $\xi = 0.3$.

constellation of base band signal with the frequency offset $\xi = 0.3$. Figure 7 presents the constellation after the first layer scheme cancellation. Figure 8 presents the constellation after the second layer scheme cancellation. As obtained from these figures, the first layer scheme may cancel the frequency offset completely when frequency offset value is smaller. But, for a larger frequency offset value, there also exists residual frequency offset. After the second layer, scheme may cancel the frequency offset completely when frequency offset value is larger.

5. Multilayer Learning Network for Frequency Offset Cancellation

5.1. Multilayer Learning Network for Modulation Classification. Define $\hat{r} = [\hat{r}(1), \hat{r}(2), \dots, \hat{r}(n)]$ as the prediction output for the network. $\hat{r}(n)$ is defined as the ideal output value for the n th-order network.


 FIGURE 8: Signal constellation after cancellation with second layer of multilayer learning network, with frequency offset $\xi_i = 0.3$.

The output estimator value of the n th layer network can be reconstructed with l th hidden layer unit and the weight w ; the l th layer network can be expressed as

$$\hat{r}_l(n) = \sum_{n=1}^N \sum_{l=1}^n w_l h_l(n), \quad (24)$$

where w_l is defined as the weight for the l th hidden layer.

h_l exists as the l th hidden layer activation function, which is obtained by the following activation function:

$$\text{sig mod } h(x) = \frac{1}{1 + e^{-x}}. \quad (25)$$

From the above, we can obtain that the output response can be obtained through k hidden layer unit, which can be expressed as

$$\hat{r}_l(n) = \sum_{n=1}^N \sum_{l=1}^n w_l h_l(n), \quad n = 1, \dots, N. \quad (26)$$

Define $\{(r(1), x(1)), (r(2), x(2)), \dots, (r(n), x(n))\}$, $n \ll t$, as training, $x(n)$ is the ideal for the n th training unit, and $r(n)$ is the target output of the n th training unit.

In order to improve prediction and classification efficiency for the multilayer learning network, the expected forecast direction is through k th hidden layer unit and l th layer network training; signal output $r(n)$ error is $E_r = \|r_i(n) - \hat{r}_i(n)\|^2 \rightarrow 0$.

Multilayer network input sequence $r(n)$ is the multipath fading signal. After the l th depth learning network training, the l th hidden layer for unit $h(n)$ can be expressed as

$$h_l(n) = \text{sig mod } ((r(n))), \quad n = 1, \dots, N \quad (27)$$

and expanded as

$$\begin{aligned} J(W) &= \sum_{n=1}^N \sum_{l=1}^n \left\| (\hat{r}_l(n)) - (r_l(n)) \right\|^2 \\ &= \sum_{n=1}^N \sum_{l=1}^n ((\hat{r}_l(n)) - (r_l(n))) \overline{((\hat{r}_l(n)) - (r_l(n)))}. \end{aligned} \quad (28)$$

By substitution, we could obtain

$$\begin{aligned} J(W) &= \sum_{n=1}^N \sum_{l=1}^n (w_l h(n) - r_l(n)) \overline{\left(\sum_{n=1}^n w_l h(n) - (r_l(n)) \right)}. \end{aligned} \quad (29)$$

Obtaining w_l for the gradient from the above equation, we could obtain

$$\frac{\partial J(W)}{\partial w_l} = \sum_{n=1}^n h(n) \left[\sum_{l=1}^n \bar{w}_l \bar{h}(n) - (\bar{r}_l(n)) \right]. \quad (30)$$

Then the available is simplified:

$$\sum_{l=1}^n \bar{w}_l \sum_{n=1}^n h(n) \bar{h}_l(n) = \sum_{n=1}^n (\bar{r}_l(n)) h(n). \quad (31)$$

The amplitude weights can be expressed as the above formula and can be represented by the matrix, which can be simplified:

$$\bar{W} = M\Omega^{-1}, \quad (32)$$

where

$$\Omega_l = \sum_{n=1}^n h(n) \bar{h}_l(n), \quad l = 1, \dots, n, \quad (33)$$

$$M_l = \sum_{n=1}^n \ln \bar{r}_l(n) h(n), \quad l = 1, \dots, n.$$

5.2. Reverse Parameter Adjustment. A parametric model for forward training networks $\{h, w\}$ should be adjusted as reversed parameter. The energy model T is used to obtain the gradient for parameters $\{h, w\}$. Through Contrastive Divergence method, we can obtain

$$\begin{aligned} \frac{\partial J(w)}{\partial w_{ij}} &= \langle w \rangle_{p_0} - \langle w \rangle_{p_M}, \\ \frac{\partial J(h)}{\partial h_j} &= \langle h_j \rangle_{p_0} - \langle h_j \rangle_{p_M}, \end{aligned} \quad (34)$$

where $\langle \cdot \rangle_{p_0}$ indicates the expectation of the data distribution and $\langle \cdot \rangle_{p_M}$ indicates the input data after Gibbs sampling.

The parameters $\{h, w\}$ can be adjusted by the following steps:

$$\begin{aligned} w_{lk}^p &= w_0^p + \eta \frac{\partial J(w^{p-1})}{\partial w^p}, \\ h_{lk}^p &= h_0^p + \eta \frac{\partial J(h^{p-1})}{\partial h^p} \end{aligned} \quad (35)$$

where η is the learning rate.

6. Experimental Classification Results and Analysis

Modulation mode commonly used in satellite communication, QPSK, 8PSK, and QAM are defined as the test sets. These modulation signals are defined as the narrowband signals with white Gaussian noise, which are modulated into the signals with narrowband Gaussian white noise. Signal carrier frequency is defined as $f_c = 1000$ kHz, symbol rate is defined as $f_s = 180$ kHz, and sampling rate is defined as $f_s = 4f_c = 4000$ kHz.

The digital signal modulation mode is generated by random generator. Multilayer learning network is simulated by Monte Carlo simulation for 20,000 tests. ξ_{\max} is the maximum normalized frequency offset, which is defined as the ratio between frequency offset and bandwidth.

Typical multipath model is established in Table 1. The main channel adopts the Rice channel model. The second-order model is Rayleigh channel model.

The measured results for urban environment were proposed in [51] with signal carrier frequency of 1.82 GHz. Table 1 shows the measured parameters of the urban environment, rural environment, and suburban environment.

6.1. BER Performance versus SNR. Firstly, we simulate BER versus SNR through frequency offset cancellation performance. The bit-error-rates (BER) versus average SNR for $\xi_{\max} = 0.05$ and $\xi_{\max} = 0.15$ are shown in Figures 9 and 10, respectively. The results with no frequency offset, no compensation, MMSE equalization algorithm [3], iterative algorithm proposed in [15], and the proposed compensation method are presented. By investigating these figures, it is clearly shown that no cancellation suffers from ICI and has a high error floor. MMSE algorithm performs well, since ICI and MUI can be removed. MMSE-SIC algorithm performs better than MMSE algorithm as the effect of noise enhancement can be significantly reduced. It is noticed that the more precise frequency offset can be obtained by the iterative algorithm at the cost of the complex iterative computation and estimation. However, the two layers of multilayer learning network exhibit the best performance.

6.2. PCC Performance versus SNR at Different Modulation. Secondly, we simulate PCC performance versus SNR. Figure 11 shows the PCC of the multilayer learning network at SNR from -5 dB to 20 dB. The frequency offset is defined as $\xi_{\max} = 0.05$. Within the same training sequence for each modulation mode, 2048 sampling points constitute a frame. 100 groups are set as training set; that is, $N = 100$. The remaining 1900 groups are test set. It can be seen from the figure that when the SNR is greater than 0 dB, the PCC of the multilayer learning network is above 93% for the above modulation scheme. At SNR greater than 5 dB, the PCC is more than 96% . Therefore, it is obtained from the simulation that the proposed multilayer learning network assisted with frequency offset cancellation has a better PCC for different signal modulation types.

TABLE I: Channel model parameter in urban environment.

Tap	Distribution function	Parameter	Parameter distribution	Numerical value/dB	Time delay/ns
1	LOS:Rician	Rice factor	K	5.3	0
	nLOS:Rayleigh	Average multipath power	$2\sigma_l^2$	-12.1	
2	Rayleigh	Average multipath power	$2\sigma_l^2$	-17.0	60
3	Rayleigh	Average multipath power	$2\sigma_l^2$	-18.3	100
4	Rayleigh	Average multipath power	$2\sigma_l^2$	-19.1	130
5	Rayleigh	Average multipath power	$2\sigma_l^2$	-22.1	250

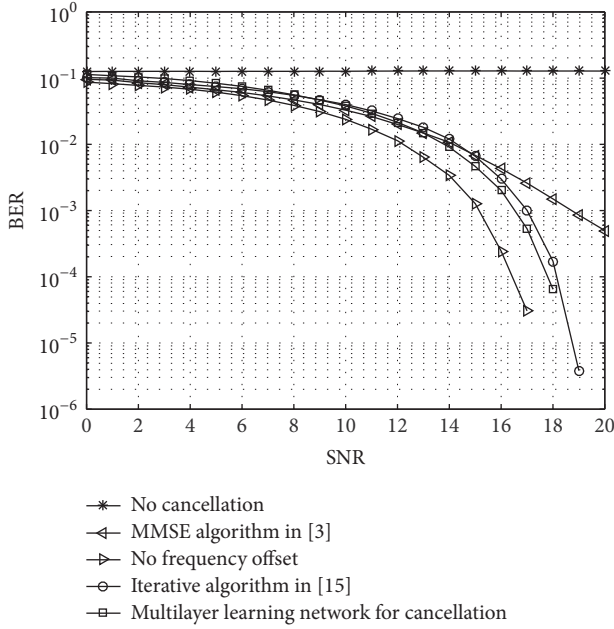


FIGURE 9: BER curves under different average SNR, with frequency offset $\xi_{\max} = 0.05$.

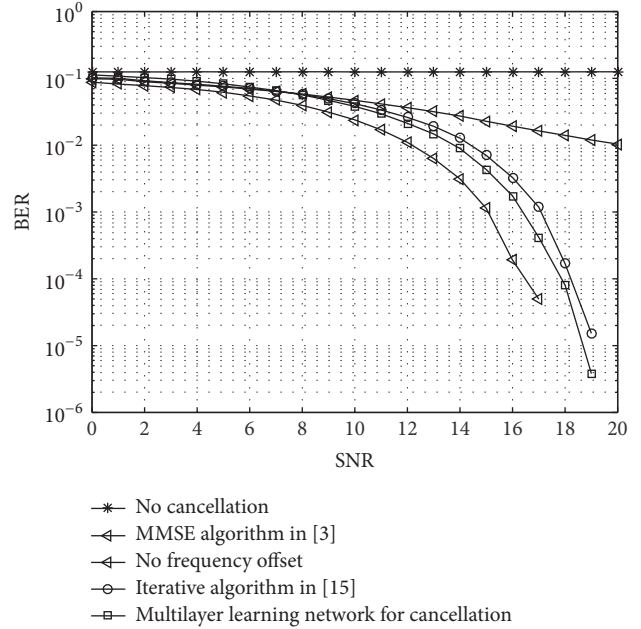


FIGURE 10: BER curves under different average SNR, with frequency offset $\xi_{\max} = 0.15$.

6.3. PCC Performance versus SNR at Different Training Length. Figure 12 shows PCC of satellite to ground link signal modulation pattern under different training lengths. Under the different training sequence conditions for each modulation mode, 2048 data frames constitute a group. Frequency offset is defined as $\xi_{\max} = 0.05$. For classification modulation within 2000 groups, we choose different lengths of training data, 20 groups, 40 groups, and 60 groups for training.

Through the above method, PCC of multilayer learning network including BPSK, QPSK, and 8PSK modulation signal are tested. It can be seen from Figure 7 that when the training length is greater than 20 groups, the PCC is above 93% for the above modulation mode. When it is greater than 40 groups, the PCC is more than 96%. Therefore, it is possible to know from the simulation that the proposed multilayer learning network has a better PCC for different types of signal modulation. The proposed multilayer learning network has more profound signal features.

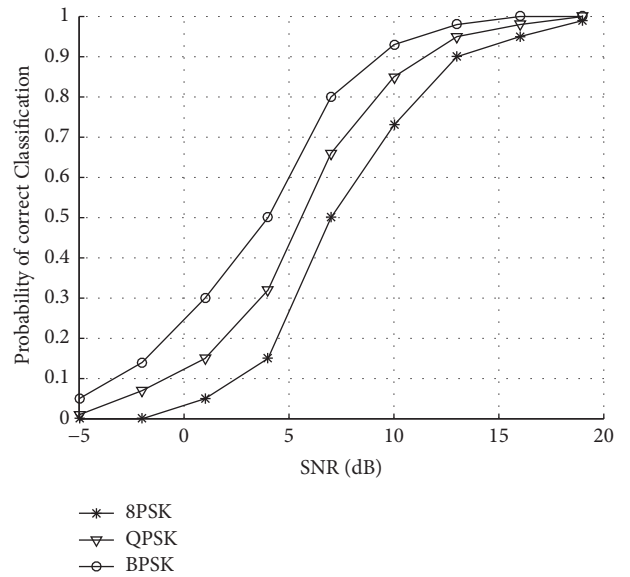


FIGURE 11: Probability of Correct Classification for the proposed learning network based on different modulation.

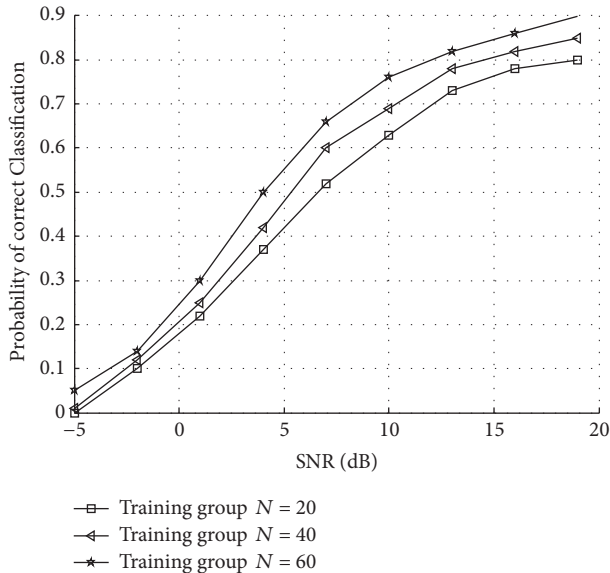


FIGURE 12: Probability of Correct Classification for the proposed learning network based on different lengths of training sequences.

6.4. *Probability of Correct Classification Simulation at Different SNR.* Figure 13 shows the PCC of proposed multilayer learning network from -5 dB to 20 dB compared with different algorithms proposed in [20, 26, 46]. Define the same training sequence for each modulation mode. 2048 data points constitute a frame, and 1024 frames constitute a group. For 2000 groups, 100 groups are training sets; that is, $N = 100$. The remaining 1900 groups are defined as the test group. When $\text{SNR} = 0$ dB, PCC for communication signal modulation mode of all algorithms is below 90%, and the performance of the algorithm is affected by noise interference.

When $\text{SNR} = 5$ dB, the performance of the algorithm for PCC has increased. The SVM proposed in literature [26] is based on the principle of wavelet packet decomposition criterion, and the PCC performance is higher based on making full use of the wavelet packet features. The PCC of SVM increases rapidly. Therefore, SVM has better PCC in Gaussian white noise. However, in case of frequency offset status, the performance for wavelet packet decomposition is constrained; thus the SVM algorithm does not show an advantage. The modulation classification algorithm based on sixth-order cumulants is proposed in literature [20]; the performance is stable under different SNR conditions. This is because the cumulants features are constrained by the frequency offset status. With frequency offset increasing, cumulants-based signal features are constrained. It can be seen from the simulation results that the proposed algorithm has high accuracy and stability under different SNR conditions. Compared with the KNN algorithm proposed in [46], the proposed multilayer learning has higher PCC under the same SNR condition. This is because the proposed multilayer learning network assisted frequency offset using the multilayer network weights for signal reconstruction.

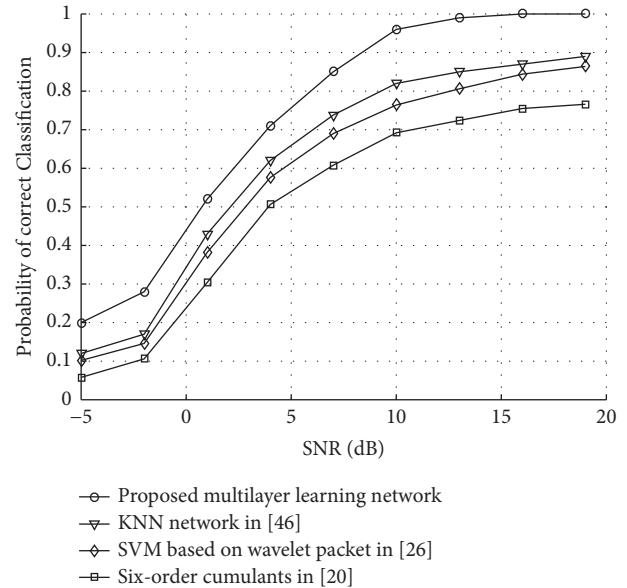


FIGURE 13: Probability of Correct Classification simulation based on different signal-to-noise ratio for different algorithms.

TABLE 2: Performance analysis of different algorithms.

SNR	Proposed network	SVM	KNN network	Cumulants
0 dB	0.43	0.31	0.34	0.23
5 dB	0.76	0.62	0.65	0.53
10 dB	0.96	0.76	0.82	0.69
15 dB	0.99	0.82	0.86	0.74
20 dB	0.995	0.85	0.89	0.78

When SNR is not less than 10 dB, the Probability of Correct Classification can reach more than 95%.

Table 2 shows the PCC performance of proposed multilayer learning network from 0 dB to 20 dB, which is compared with different algorithms proposed in [20, 26, 46].

Table 3 shows the measured parameters for the proposed multilayer learning network, which is compared with different algorithms proposed in [20, 26, 46].

6.5. *Importance for Multilayer Learning Network with MSE Guidelines.* For the frequency offset interference cancellation neural network, the interference is induced by the instantaneous linear exponential multiplicative interference, according to relevant proofs given about formulations (15)–(17), (19), (21), (22), and (23) in Sections 4.2 and 4.3.

The MSE criterion can obtain the optimal interference cancellation performance, and the multiplicative exponential linear interference cancellation can be eliminated. Obtaining few training samples according to MSE criterion, the generated weight network can be trained and the optimal interference cancellation performance can be obtained. So it is effective for adopting the MSE criterion to establish the neural network.

In order to prove the effectiveness of the MSE criterion, Figure 14 shows PCC of satellite to ground link signal

TABLE 3: Parameters analysis of different algorithms.

Method	Proposed network	SVM	KNN network	Cumulants
Parameters	Nonlinear	Nonlinear	Nonlinear	linear

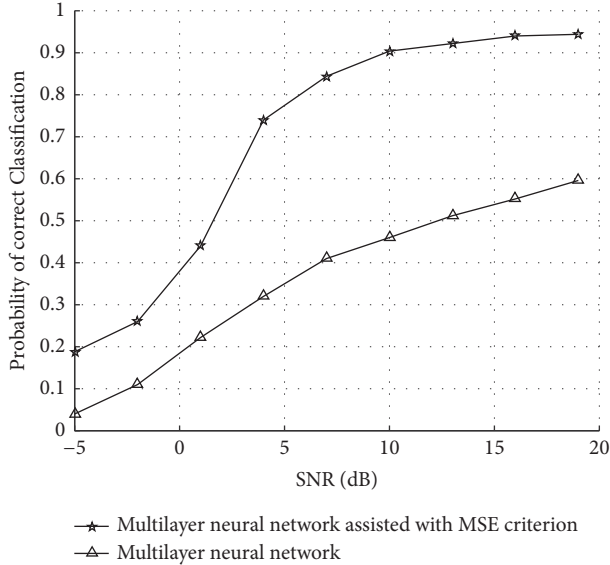


FIGURE 14: Modulation classification assisted with MSE criterion.

modulation classification assisted or not with MSE criterion. For classification modulation within 2000 groups, we choose 200 groups for training. 2048 data frames constitute a group. Frequency offset is defined as $\xi_{\max} = 0.05$.

Through the above method, PCC of deep learning network including BPSK, QPSK, and 8PSK modulation signal are tested. It can be seen from Figure 13 that when the training length is the same, the PCC is above 93% for modulation classification assisted with MSE criterion, which can obtain the optimal interference cancellation performance. Therefore, it is possible to know from the simulation that the proposed deep learning network has a better PCC for different types of signal modulation. Based on MSE criterion, the proposed deep learning network has more profound signal features.

6.6. Overfitting Analysis of Multilayer Learning Assisted with Frequency Offset Cancellation. For the characteristics of satellite link communication signals, the influence of modulation mode classification is mainly due to the interference of larger carrier frequency offset. If the frequency offset interference is not eliminated, more training samples are needed to ensure correct fitting. Due to the innovation of the paper, carrier frequency offset interference cancellation is performed with fewer samples assisted with MSE criterion; thus it improves the accuracy of the modulation mode classification.

Excluding related frequency offset interferences, the classification features are obtained based on the modulation mode, and the model can be established by a small amount of data to ensure the PCC and prevent overfitting of the data.

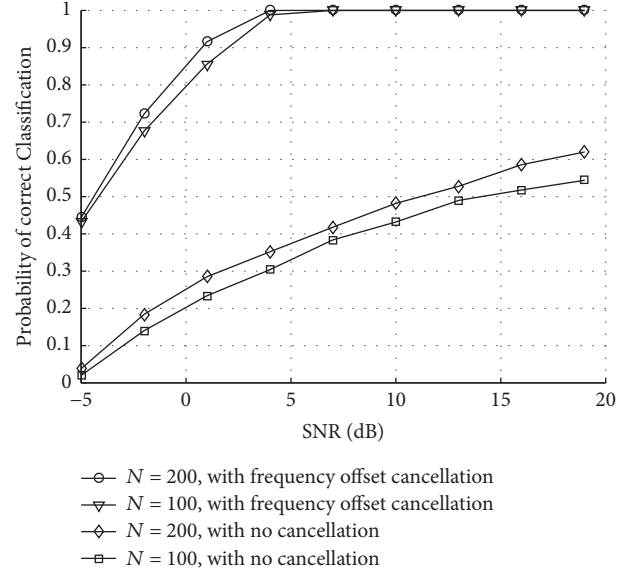


FIGURE 15: PCC for signal modulation classification assisted with frequency offset cancellation.

At the same time, we perform simulation with different training samples. In the condition of frequency offset interference, we could need more training samples in order to ensure a reasonable PCC. And it is the thesis that a small amount of training samples is used to ensure the precancellation of frequency offset interference that makes it possible to obtain a higher classification recognition rate with fewer training sequences.

In order to prove that the small training set can be potentially overfit for the dataset, Figure 15 shows PCC of satellite to ground link signal modulation classification assisted or not with frequency offset cancellation. For classification modulation within 2000 groups, we choose 100 groups and 200 groups for training. 2048 data frames constitute a group. Frequency offset is defined as $\xi_{\max} = 0.05$.

Through the above method, PCC of deep learning network including BPSK, QPSK, and 8PSK modulation signal are tested. It can be seen from Figure 12 that when the training length is the small, the PCC is above 97% for modulation classification assisted with frequency offset cancellation, which can obtain the ideal performance. Therefore, it is possible to know from the simulation that the proposed multilayer learning network has a better PCC for small training set.

7. Conclusion

A multilayer learning network assisted with frequency offset cancellation is proposed for modulation classification in satellite to ground link. Larger carrier frequency offset

greatly degrades the performance of modulation classification. Firstly, we establish cancellation weights for frequency offset through multilayer learning network. Secondly, we establish the weights and hidden layers for modulation classification through multilayer learning network. We also train hidden layers and weight using positive fine-tuning to cancel the interference introduced by frequency offset in the satellite to ground link. Compared with current modulation classification algorithm, the proposed multilayer learning offset greatly improves the PCC. It has been proven that the multilayer learning network model assisted with frequency offset has higher performance for the satellite communication signal classification within the same training sequence.

Conflicts of Interest

The author declares that there are no conflicts of interest.

Acknowledgments

This work is supported by the National Natural Science Foundation of China (no. 61501306), the Natural Science Foundation of Liaoning Province of China (no. 2015020026), and the Natural Science Foundation of Liaoning Provincial Department of Education (no. L2015402).

References

- [1] S. Jajodia, P. Ammann, and C. D. McCollum, "Surviving information warfare attacks," *The Computer Journal*, vol. 32, no. 4, pp. 57–63, 1999.
- [2] X. Li, J. Luo, and Y. Cao, "Multi-agent model of information warfare system," in *Proceedings of the International Symposium on Communications and Information Technologies, ISCIT '05*, pp. 554–557, October 2005.
- [3] T. A. Lipinski, "Information warfare, American style," *IEEE Technology and Society Magazine*, vol. 18, no. 1, pp. 10–19, 1999.
- [4] A. Tonello and S. Pupolin, "Performance of single user detectors in multitone multiple access asynchronous communications," in *Proceedings of the Vehicular Technology Conference. IEEE 55th Vehicular Technology Conference. VTC Spring '02*, pp. 199–203, Birmingham, AL, USA.
- [5] C. Z. Ren, U. Tureli, and Y. Yu-Dong, "Analysis of two receiver schemes for interleaved OFDMA uplink," in *Proceedings of the Signals, Systems and Computers, Conference Record of the Thirty-Sixth Asilomar Conference*, vol. 2, pp. 1818–1821.
- [6] M. Huang, X. Chen, S. Zhou, and J. Wang, "Iterative ICI cancellation algorithm for uplink OFDMA system with carrier-frequency offset," in *Proceedings of the 62nd Vehicular Technology Conference, VTC 2005*, pp. 1613–1617, USA, September 2005.
- [7] D. Huang and K. B. Letaief, "An interference-cancellation scheme for carrier frequency offsets correction in OFDMA systems," *IEEE Transactions on Communications*, vol. 53, no. 7, pp. 1155–1165, 2005.
- [8] J. Choi, C. Lee, H. W. Jung, and Y. H. Lee, "Carrier frequency offset compensation for uplink of OFDM-FDMA systems," *IEEE Communications Letters*, vol. 4, no. 12, pp. 414–416, 2000.
- [9] M.-O. Pun, M. Morelli, and C.-C. J. Kuo, "Iterative detection and frequency synchronization for OFDMA uplink transmissions," *IEEE Transactions on Wireless Communications*, vol. 6, no. 2, pp. 629–639, 2007.
- [10] R. Fantacci, D. Marabissi, and S. Papini, "Multiuser interference cancellation receivers for ofdma uplink communications with carrier frequency offset," in *Proceedings of the GLOBECOM '04 - IEEE Global Telecommunications Conference*, vol. 5, pp. 2808–2812, IEEE, 2004.
- [11] V. D. Trajković, P. B. Rapajic, and R. A. Kennedy, "Adaptive ordering for imperfect successive decision feedback multiuser detection," *IEEE Transactions on Communications*, vol. 56, no. 2, pp. 173–176, 2008.
- [12] S. Hou and C. C. Ko, "Inter-carrier interference suppression for OFDMA uplink in time and frequency selective Rayleigh fading channels," in *Proceedings of the 2008 IEEE 67th Vehicular Technology Conference-Spring, VTC*, pp. 1438–1442, Singapore, May 2008.
- [13] D. Sreedhar and A. Chockalingam, "MMSE receiver for multiuser interference cancellation in uplink OFDMA," in *Proceedings of the 2006 IEEE 63rd Vehicular Technology Conference, VTC 2006-Spring*, vol. 5, pp. 2125–2129, July 2006.
- [14] D. Marabissi, R. Fantacci, and S. Papini, "Robust multiuser interference cancellation for OFDM systems with frequency offset," *IEEE Transactions on Wireless Communications*, vol. 5, no. 11, pp. 3068–3076, 2006.
- [15] K. Raghunath and A. Chockalingam, "SIR analysis and interference cancellation in uplink OFDMA with large carrier frequency and timing offsets," in *Proceedings of the IEEE Wireless Communications and Networking Conference, WCNC '07*, pp. 996–1001, March 2007.
- [16] V. Orlić and M. L. Dukić, "Algorithm for automatic modulation classification in multipath channel based on sixth-order cumulants," in *Proceedings of the 9th International Conference on Telecommunication in Modern Satellite, Cable, and Broadcasting Services (TELSIKS '09)*, pp. 423–426, IEEE, Niš, Serbia, October 2009.
- [17] A. Swami and B. M. Sadler, "Hierarchical digital modulation classification using cumulants," *IEEE Transactions on Communications*, vol. 48, no. 3, pp. 416–429, 2000.
- [18] O. Dobre, Y. Bar-Ness, and W. Su, "Robust QAM modulation classification algorithm using cyclic cumulants," in *Proceedings of the IEEE Wireless Communications and Networking Conference*, pp. 745–748, March 2004.
- [19] A. E. El-Mahdy, "Classification of MFSK signals over time-varying flat correlated fading channels under class-A impulsive noise environment," *The Journal of the Institution of Electrical Engineers*, vol. 151, no. 6, pp. 619–626, 2004.
- [20] P. Li, F. Wang, and Z. Wang, "Algorithm for modulation recognition based on high-order cumulants and subspace decomposition," in *Proceedings of the 8th International Conference on Signal Processing, ICSP '06*, 2006.
- [21] M. R. Mirarab and M. A. Sobhani, "Robust modulation classification for PSK/QAM/ASK using higher-order cumulants," in *Proceedings of the 6th International Conference on Information, Communications and Signal Processing, ICICS '07*, 2007.
- [22] H. You and D.-H. Wang, "Dynamics of multiple-choice decision making," *Neural Computation*, vol. 25, no. 8, pp. 2108–2145, 2013.
- [23] T. Wimalajeewa and P. K. Varshney, "Asymptotic performance of categorical decision making with random thresholds," *IEEE Signal Processing Letters*, vol. 21, no. 8, pp. 994–997, 2014.

- [24] Y. T. Chan and L. G. Gadbois, "Identification of the modulation type of a signal," *Signal Processing*, vol. 16, no. 2, pp. 149–154, 1989.
- [25] M. L. D. Wong and A. K. Nandi, "Automatic digital modulation recognition using spectral and statistical features with multi-layer perceptrons," in *Proceedings of the 6th International Symposium on Signal Processing and Its Applications, ISSPA '01*, pp. 390–393, August 2001.
- [26] F. Zhao, Y. Hu, and S. Hao, "Classification using wavelet packet decomposition and support vector machine for digital modulations," *Journal of Systems Engineering and Electronics*, vol. 19, no. 5, pp. 914–918, 2008.
- [27] N. Ghani and R. Lamontagne, "Neural networks applied to the classification of spectral features for automatic modulation recognition," in *Proceedings of the MILCOM '93 - IEEE Military Communications Conference*, pp. 111–115, Boston, MA, USA.
- [28] M. Lu, X. Xiao, and L. Li, "Cyclic spectral features based modulation recognition," in *Proceedings of the 1996 International Conference on Communication Technology Proceedings, ICCT'96. Part 2 (of 2)*, pp. 792–795, May 1996.
- [29] N. P. Ta, "A wavelet packet approach to radio signal classification," in *Proceedings of the IEEE-SP International Symposium on Time-Frequency and Time-Scale Analysis*, pp. 508–511, 1994.
- [30] K. C. Ho, W. Prokopiw, and Y. T. Chan, "Modulation identification of digital signals by the wavelet transform," *IEE Proceedings—Radar, Sonar and Navigation*, vol. 147, no. 4, pp. 169–176, 2000.
- [31] S. Huang, Y. Yao, Y. Xiao, and Z. Feng, "Cumulant based maximum likelihood classification for overlapped signals," *IEEE Electronics Letters*, vol. 52, no. 21, pp. 1761–1763, 2016.
- [32] Y. Yang and S. S. Soliman, "A suboptimal algorithm for modulation classification," *IEEE Transactions on Aerospace and Electronic Systems*, vol. 33, no. 1, pp. 38–45, 1997.
- [33] C. Schreyoegg and J. Reichert, "Modulation classification of QAM schemes using the DFT of phase histogram combined with modulus information," in *Proceedings of the Military Communications Conference Proceedings, MILCOM '97*, vol. 3, pp. 1372–1376, IEEE, 1997.
- [34] B. F. Beidas and C. L. Weber, "Asynchronous classification of mfsk signals using the higher order correlation domain," *IEEE Transactions on Communications*, vol. 46, no. 4, pp. 480–493, 1998.
- [35] D. Boiteau and C. Le Martret, "A general maximum likelihood framework for modulation classification," in *Proceedings of the 23rd IEEE International Conference on Acoustics, Speech and Signal Processing, ICASSP '98*, pp. 2165–2168, 1998.
- [36] A. Ahmad and G. Brown, "Random projection random discretization ensembles - Ensembles of linear multivariate decision trees," *IEEE Transactions on Knowledge and Data Engineering*, vol. 26, no. 5, pp. 1225–1239, 2014.
- [37] M. Biswal and P. K. Dash, "Measurement and classification of simultaneous power signal patterns with an s-transform variant and fuzzy decision tree," *IEEE Transactions on Industrial Informatics*, vol. 9, no. 4, pp. 1819–1827, 2013.
- [38] H. G. Zhang, Z. S. Wang, and D. R. Liu, "A comprehensive review of stability analysis of continuous-time recurrent neural networks," *IEEE Transactions on Neural Networks and Learning Systems*, vol. 25, no. 7, pp. 1229–1262, 2014.
- [39] J. Wang, C.-H. Wang, and C. L. P. Chen, "The bounded capacity of fuzzy neural networks (FNNs) via a new fully connected neural fuzzy inference system (F-CONFIS) with its applications," *IEEE Transactions on Fuzzy Systems*, vol. 22, no. 6, pp. 1373–1386, 2014.
- [40] Z. Lu, J. Sun, and K. Butts, "Multiscale asymmetric orthogonal wavelet kernel for linear programming support vector learning and nonlinear dynamic systems identification," *IEEE Transactions on Cybernetics*, vol. 44, no. 5, pp. 712–724, 2014.
- [41] Z. Hao, L. He, B. Chen, and X. Yang, "A linear support higher-order tensor machine for classification," *IEEE Transactions on Image Processing*, vol. 22, no. 7, pp. 2911–2920, 2013.
- [42] Y. Zhao, C. K. Li, and Z. Wu, "An efficient parallel decision algorithm for recognition of modulation systems in a software radio," *IEICE Transactions on Communications*, vol. E87-B, no. 13, pp. 174–178, 2004.
- [43] A. Swami and B. Sadler, "Modulation classification via hierarchical agglomerative cluster analysis," in *Proceedings of the 1st IEEE Signal Processing Workshop on Signal Processing Advances in Wireless Communications, SPAWC '97*, pp. 141–144, April 1997.
- [44] M. L. D. Wong and A. K. Nandi, "Automatic digital modulation recognition using artificial neural network and genetic algorithm," *Signal Processing*, vol. 84, no. 2, pp. 351–365, 2004.
- [45] P. Urriza, E. Rebeiz, and D. Cabric, "Optimal discriminant functions based on sampled distribution distance for modulation classification," *IEEE Communications Letters*, vol. 17, no. 10, pp. 1885–1888, 2013.
- [46] M. W. Aslam, Z. Zhu, and A. K. Nandi, "Automatic modulation classification using combination of genetic programming and KNN," *IEEE Transactions on Wireless Communications*, vol. 11, no. 8, pp. 2742–2750, 2012.
- [47] J. F. Ossanna, "A model for mobile radio fading due to building reflections: theoretical and experimental fading waveform power spectra," *Bell System Technical Journal*, vol. 43, no. 6, pp. 2935–2971, 1964.
- [48] R. H. Clarke, "A statistical theory of mobile-radio reception," *Bell Labs Technical Journal*, vol. 47, no. 2, pp. 957–1000, 1968.
- [49] C. Loo, "A statistical model for a land mobile satellite link," *IEEE Transactions on Vehicular Technology*, vol. 34, no. 3, pp. 122–127, 1985.
- [50] A. Abdi, W. C. Lau, M. Alouini, and M. Kaveh, "A new simple model for land mobile satellite channels: first-and second-order statistics," *IEEE Transactions on Wireless Communications*, vol. 2, no. 3, pp. 519–528, 2003.
- [51] E. Lutz, M. Werner, and A. Jahn, *Satellite Systems for Personal and Broadband Communication Germany*, Springer, Berlin, Germany, 2000.

Research Article

The Parallel Algorithm Based on Genetic Algorithm for Improving the Performance of Cognitive Radio

Liu Miao ¹, Zhenxing Sun,^{1,2,3} and Zhang Jie⁴

¹Department of Electronics and Information Engineering, Northeast Petroleum University, No. 550, West Hebei Avenue, Qinhuangdao 066004, China

²School of Computer Science and Engineering, Northeastern University, Shenyang, China

³Qinhuangdao Economic and Technological Development Zone, No. 143 Taishan Road, Qinhuangdao, Hebei 066004, China

⁴Editorial Board of Journal of Jilin University (Information and Science Edition), Jilin University, Changchun 130012, China

Correspondence should be addressed to Liu Miao; lm_jlu@163.com

Received 21 September 2017; Revised 20 December 2017; Accepted 4 January 2018; Published 12 March 2018

Academic Editor: Fei Hu

Copyright © 2018 Liu Miao et al. This is an open access article distributed under the Creative Commons Attribution License, which permits unrestricted use, distribution, and reproduction in any medium, provided the original work is properly cited.

The intercarrier interference (ICI) problem of cognitive radio (CR) is severe. In this paper, the machine learning algorithm is used to obtain the optimal interference subcarriers of an unlicensed user (un-LU). Masking the optimal interference subcarriers can suppress the ICI of CR. Moreover, the parallel ICI suppression algorithm is designed to improve the calculation speed and meet the practical requirement of CR. Simulation results show that the data transmission rate threshold of un-LU can be set, the data transmission quality of un-LU can be ensured, the ICI of a licensed user (LU) is suppressed, and the bit error rate (BER) performance of LU is improved by implementing the parallel suppression algorithm. The ICI problem of CR is solved well by the new machine learning algorithm. The computing performance of the algorithm is improved by designing a new parallel structure and the communication performance of CR is enhanced.

1. Introduction

Cognitive radio (CR) technologies based on the dynamic spectrum access concept can utilize temporarily idle spectrum resources [1, 2]. CR can improve the current tension of spectrum resources and enhance wireless communication performance [3]. Spectrum Pooling is a very effective spectrum utilization technology of CR. The licensed spectrum of different businesses is merged into a public spectrum pool by Spectrum Pooling [4]. Unlicensed users can utilize the idle spectrum which is not occupied by licensed users in Spectrum Pooling. Spectrum Pooling based on Orthogonal Frequency Division Multiplexing (OFDM) has been widely accepted [5]. However, the side lobe interference of OFDM signal is the shortcoming of Spectrum Pooling based on OFDM [6]. Spectrum Pooling based on Wavelet-Based Orthogonal Frequency Division Multiplexing (SP-WOFDM) can not only obtain the same perfect performance of OFDM but also configure subchannels flexibly and suppress Intersymbol Interference (ISI), pulse interference, and narrow

band interference more effectively. And it can realize multi-rate signal transmission to meet the requirements of different businesses and business quality more conveniently [7, 8]. Moreover, SP-WOFDM owns better bandwidth effectiveness without side lobe interference because it does not need guard interval and pilot.

In a multipath environment, the orthogonality of WOFDM signal is lost so that Intersymbol Interference (ISI) and Intercarrier Interference (ICI) occur [9, 10]. The performance of SP-WOFDM can be destroyed by ICI and ISI. Masking one or more un-LU's subcarriers can mitigate the ICI of SP-WOFDM. But it can sacrifice bandwidth in the rental system. So, it is important to research the trade-off between reducing the interference power and maintaining the bandwidth of the unlicensed system. The genetic algorithm (GA) is an efficient, practical, and robust optimization technique. Its essence is parallel, efficient, and global search methods. It can obtain and accumulate the related knowledge of the search space automatically and control the search process adaptively to get the optimal solution. The GA has characteristics including

operating on the encoding of the parameter, no deducing and additional information, the uncertainty of optimization rules, self-organization, self-adaption, and self-learning, compared with the traditional optimal algorithms.

In the paper, GA for suppression ICI energy of SP-WOFDM is proposed. The optimal interference subcarriers for suppression ICI that the un-LU causes to the LU can be obtained by a new algorithm. Moreover, the parallel ICI suppression algorithm is designed to improve the calculation speed of ICI suppression based on GA and meet the practical requirement of CR. The new algorithm does not only realize the trade-off between reducing the interference power and maintaining the bandwidth of the unlicensed system, but also consider the calculation speed and practicability of the algorithm.

The paper is organized as follows. The system model and ICI energy of SP-WOFDM are provided in Section 2. In Section 3, GA for ICI suppression is proposed. The parallel ICI suppression algorithm is designed in Section 4. The simulation results are described in Section 5. Section 6 concludes the paper.

2. The CR System Model

The SP-WOFDM with an ICI suppression unit is shown in Figure 1. The modulated signal $y(n)$ can be expressed in the discrete domain as [11]

$$y(n) = \sum_i \sum_j^{M-1} (\bar{x}_{i,j} h_j(n - iM)) \uparrow_M \quad \bar{x}_{i,j} = w_{i,j} x_{i,j}. \quad (1)$$

In Spectrum Pooling, the average ICI energy which influences subcarrier j of LU can be deduced as [12]

$$\sigma_{RU_j}^2 = \frac{1}{N_l} \sum_{i=1}^{N_l} \left(\sum_{n=-\infty}^{+\infty} \left| \sum_{m=-\infty}^{+\infty} h_{l_i}(m-p) h_{r_j}^*(m-2^{D_i}n) \right|^2 \right). \quad (2)$$

3. The GA for CR ICI Suppression

GA is an adaptive method to solve the search problem. It is based on parallel search of the chromosome group, selecting operations with guessing, switching operations, and mutation operations. So, GA has the following characteristics.

GA begins its search from the set of problem solutions, rather than the single solution. This is a great difference between GA and traditional optimization algorithms. The traditional optimization algorithms get local optimal solutions easily because they obtain the optimal solution from a single initial value iteration. GA begins its search from the set of problem solutions. So, it covers a wide area and it is good for global choice.

GA need not search spatial knowledge or other auxiliary information. It utilizes the fitness function value to evaluate individuals and carry out genetic operation. The fitness function is not limited to continuous differentiable functions, and its definition domain can be set arbitrarily. This feature expands the application range of GA greatly.

GA adopts the changing rules of probability rather than deterministic rules to guide its search direction.

GA is self-organizing, adaptive, and self-learning. When GA uses the information of the evolution process to organize the search, the individual with large fitness has a higher probability of survival and can obtain a more adaptive genetic structure.

The Spectrum Pooling ICI suppression algorithm based on GA is shown in Figure 2. At first, the data transmission rate threshold R_{thr} of un-LU and the fitness threshold are set. The masked subcarrier sequence length L is calculated by R_{thr} . The subcarrier set b_i , $i = 1, 2, \dots, L$, is randomly selected from un-LU subcarriers as the original sequence. The better intermediate carrier sequence is selected by the fitness function. The new subcarrier sequence is produced by overlapping and variation. The fitness function is adjusted constantly to produce the new intermediate carrier sequence until the fitness reaches the set threshold. The optimal interference subcarrier sequence is obtained. The CR interference suppression is realized by masking the optimal interference subcarrier sequence.

The specific process of ICI suppression algorithm is described as follows:

(1) Setting the data transmission rate threshold R_{thr} of un-LU and the fitness threshold.

(2) Original selecting subcarrier sequence of un-LU.

We select subcarrier set b_i , $i = 1, 2, \dots, L$, from subcarriers of un-LU randomly,

$$L = \frac{R(x) - R_{\text{thr}}}{\text{bit}_x}, \quad (3)$$

where $R(x)$ is the original data transmission rate of un-LU before the interference is suppressed. bit_x is the number of bits assigned to each subcarrier.

(3) Selecting a better intermediate carrier sequence.

A better intermediate carrier sequence is selected by the fitness function. The average ICI energy of the j un-LU's subcarrier infecting LU (2) is selected as the fitness function of the j un-LU's subcarrier. The fitness function can be described as follows:

$$f(b_j) = \frac{1}{N_l} \sum_{i=1}^{N_l} \left(\sum_{n=-\infty}^{+\infty} \left| \sum_{m=-\infty}^{+\infty} h_{l_i}(m-p) h_{r_j}^*(m-2^{D_i}n) \right|^2 \right), \quad (4)$$

where h_l is the filter of LU for modulating subcarriers, $h_l = [h_{l_1} h_{l_2} \dots h_{l_{N_l}}]$. h_r is the filter of un-LU for modulating subcarriers, $h_r = [h_{r_1} h_{r_2} \dots h_{r_{N_l}}]$. The ranges of m and n are decided by the length of the filter. p is the additional delay of the channel. h_{l_i} and h_{r_j} are wavelet filter functions for modulating subcarriers i and j of LU, respectively. N_l is the number of LU's subcarriers. D_i , $i = 0 \dots N - 1$, is the level of filter i .

The fitness adjustment formula can be described as

$$f(b_j + 1) = af(b_j) + b, \quad (5)$$

$$\max \{f(b_j) \mid b_j \in \{0, 1\} L\},$$

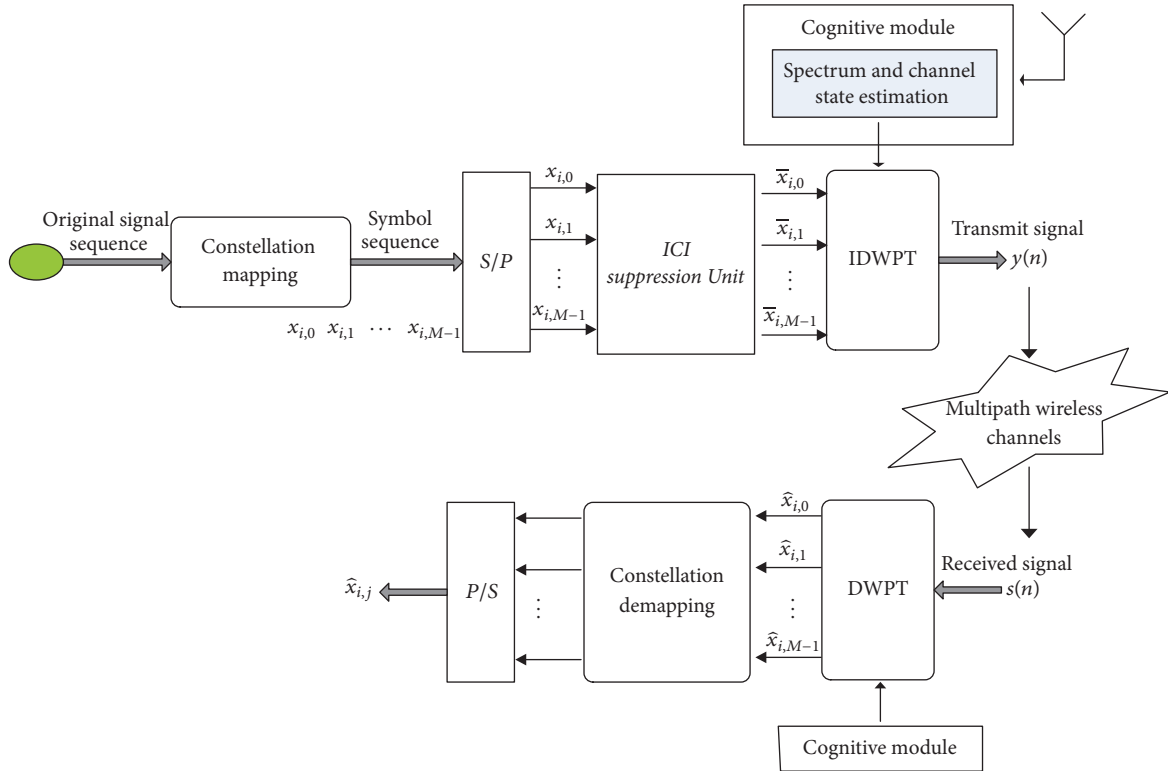


FIGURE 1: The block diagram of Spectrum Pooling with an ICI suppression unit.

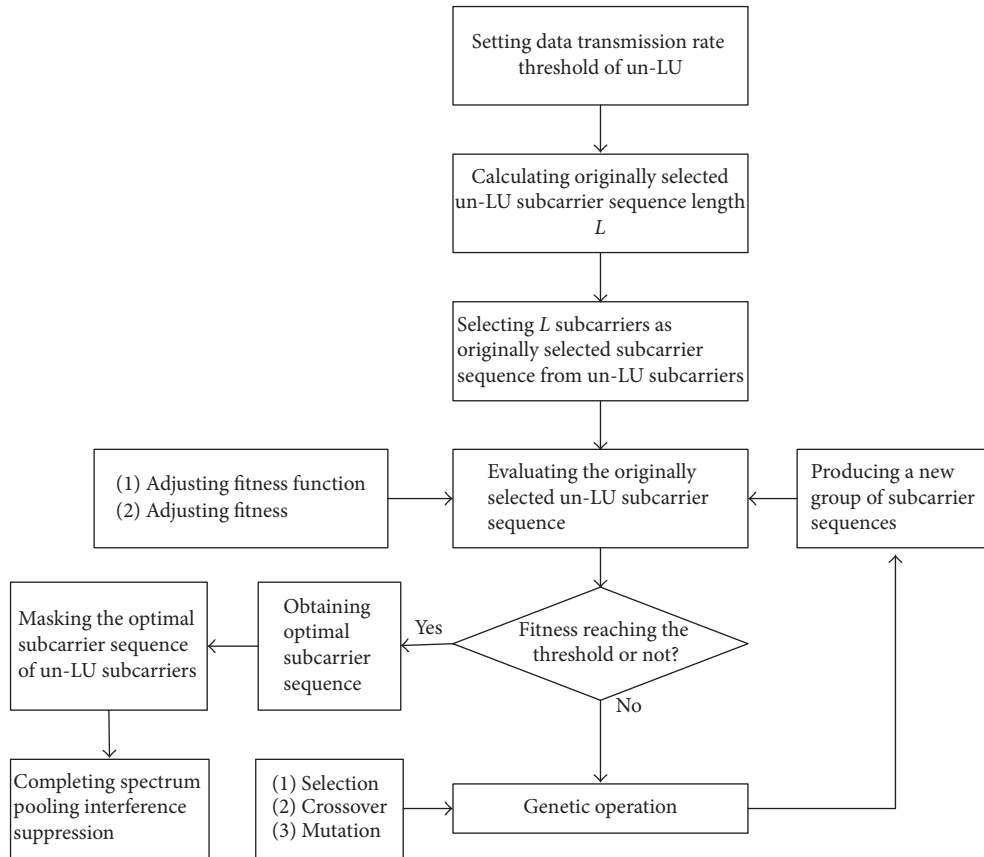


FIGURE 2: The flowchart of GA for ICI suppression.

where $f(b_j) \neq f(b_j + 1)$, a and b are the fitness parameters, and L is the length of the original set.

(4) Crossing and generating the new optional carriers.

Two intermediate carriers selected from intermediate carrier sequence are crossed to generate the new optional carriers by crossover probability p . p is defined as

$$p(b_j) = \frac{f(b_j)}{\sum_{j=1}^n f(b_j)}, \quad (6)$$

where b_j is the original carrier sequence and $f(b_j)$ is a fitness function.

(5) Variation and generating the new optional carriers.

The new optional carriers can be generated by variation probability p_m . p_m is defined as follows.

For a given carrier group $s = b_1 b_2 \cdots b_L$,

$$O(p_m, x) : b_j = \begin{cases} 1 - b_j, & \text{if } x_j \leq p_m \\ b_j, & \text{else,} \end{cases} \quad (7)$$

where $j \in \{1, 2, \dots, L\}$, L is the original carrier set, and $x_j \in [1, 0]$.

(6) Obtaining optimal interference subcarrier sequences.

When the fitness of optimal subcarrier reaches the given threshold, the optimal interference subcarrier sequence is obtained. The interference suppression of CR is realized by masking the optimal interference subcarrier sequence.

The complexity of GA is $O(N^2)$.

4. Parallel Algorithm Design for CR

Parallel computing is the process of using multiple computing resources to solve computing problems. Traditional serial computing is the process of performing single operations one by one on a single central processing unit. But parallel computing can simultaneously perform multiple operations on a set of processor units. Parallel computing can quickly solve large and complex computing problems. In the multicore era, better performance can be obtained by designing a parallel computing algorithm based on multithreads on a multicore computing platform.

The Spectrum Pooling ICI suppression parallel algorithm based on multithreads is designed by us to improve the calculation speed of Spectrum Pooling ICI suppression algorithm based on GA and make it more practical. The Spectrum Pooling ICI suppression algorithm based on GA can be parallelized as follows:

(1) Parallelizing fitness evaluation of originally selected subcarriers.

The fitness evaluation of the selected subcarriers takes up most of the execution time and there is no dependence on each other. So, fitness evaluation computing of originally selected subcarriers can be assigned to different cores in a multicore processor.

(2) Parallelizing each genetic operator.

The operation of cross, selection, and variation can be threaded and performed on different cores independently and concurrently.

The specific process of parallel ICI suppression algorithm is described as follows:

- (1) Setting the data transmission rate threshold of un-LU and the fitness threshold.
- (2) Original selecting of subcarrier sequence of un-LU.
- (3) Parallel selecting of better intermediate carrier sequence.
- (4) Parallel performing of the crossing operation and generating the new optional carriers.
- (5) Parallel performing of the variation operation and generating the new optional carriers.
- (6) Obtaining optimal interference subcarrier sequences.

The parallel ICI suppression algorithm can run on a multicore computing platform and it has the advantage of multithreads. So, the parallel ICI suppression algorithm can not only improve the calculation speed of the original ICI suppression algorithm based on GA, but also meet the practical requirement of CR.

5. Simulation Results

To test the performance of the ICI suppression algorithm based on GA, we construct Spectrum Pooling with 32 subcarriers. Spectrum Pooling is divided into 8 subbands and each subband matches 4 subcarriers. The Daubechies-4 (Db(4)) is implemented to modulate the subcarriers of Spectrum Pooling. QPSK is used to realize symbol constellation.

To simulate the wireless channel environment, we use the two-path wireless channel model. The impulse response of channel is defined as follows [13]:

$$h_{\text{ch}}(n) = \delta(n) + \delta(n - pp) e^{j\theta_1}, \quad (8)$$

where pp is a positive integer; it represents an additional delay of the channel and is normalized as a symbol period. θ_1 is the random phase; the range of θ_1 is $[0, 2\pi)$.

Set the crossover probability $p = 0.8$ and variation probability $p_m = 0.1$.

The simulation scene is designed as follows.

Scene 1. LU occupies the central 3–6 subbands and 4–5 subbands of Spectrum Pooling, respectively.

Scene 2. LU occupies the 2, 3, 5, and 7 subbands of Spectrum Pooling. LU occupies the 2, 4, 6, and 8 subbands of Spectrum Pooling. LU occupies the 2 and 6 subbands of Spectrum Pooling.

Figures 3 and 4 are the simulation results of Scene 1 and Scene 2. It is shown that the ICI energy of un-LU decreases if the number of masked optimal interference subcarriers increases for both Scene 1 and Scene 2. Furthermore, the ICI energy of un-LU decreases with the number of LU's subcarriers increasing if the same number of optimal interference subcarriers is masked.

In Figures 5 and 6, the LU occupied 8 subcarriers in the Spectrum Pooling and the two-path wireless channel model

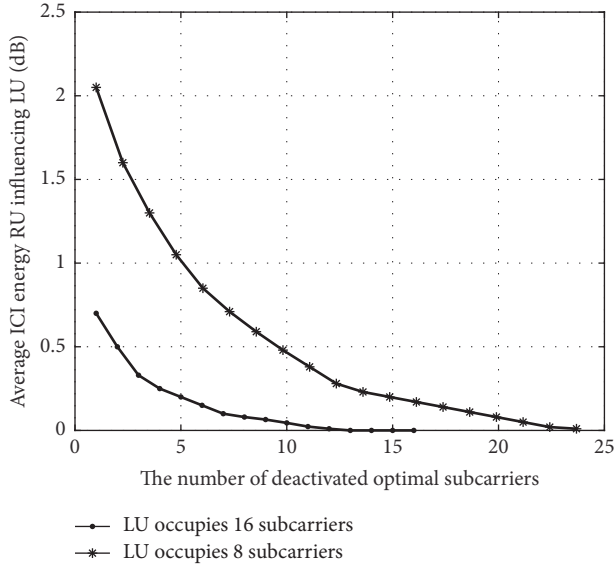


FIGURE 3: The relation between the number of masked optimal subcarriers and ICI energy in Scene 1 based on Db(4).

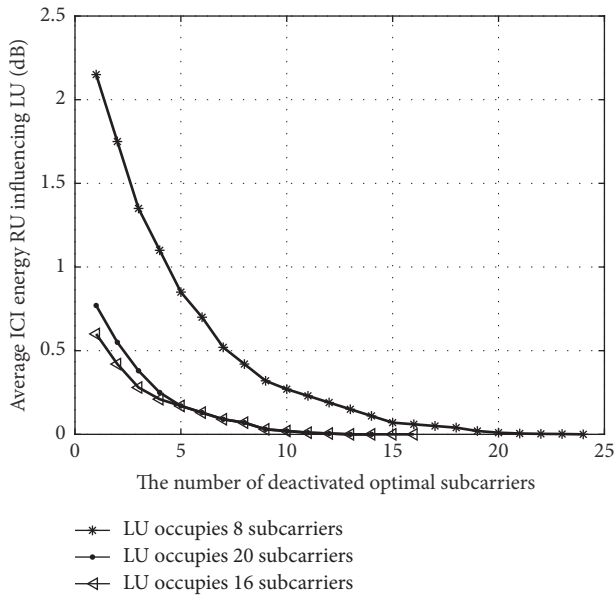


FIGURE 4: The relation between the number of masked optimal interference subcarriers and ICI energy in Scene 2 based on Db(4).

with $p = 0, \theta_1 = \pi/5$ is implemented. In the wireless channel with only multipath effect, Figures 5 and 6 are the simulation results of LU occupying central successive subbands and the 2 and 6 subbands. It is shown that the BER performance of LU is improved if the number of masked optimal interference subcarriers increases.

The GA is used to obtain the optimal subcarriers. Figures 3, 4, 5, and 6 describe the ICI performance of LU masking different numbers of optimal subcarriers and the BER performance of LU masking different numbers of optimal subcarriers. The results show that the ICI of LU can be suppressed and BER performance of LU can be improved by GA.

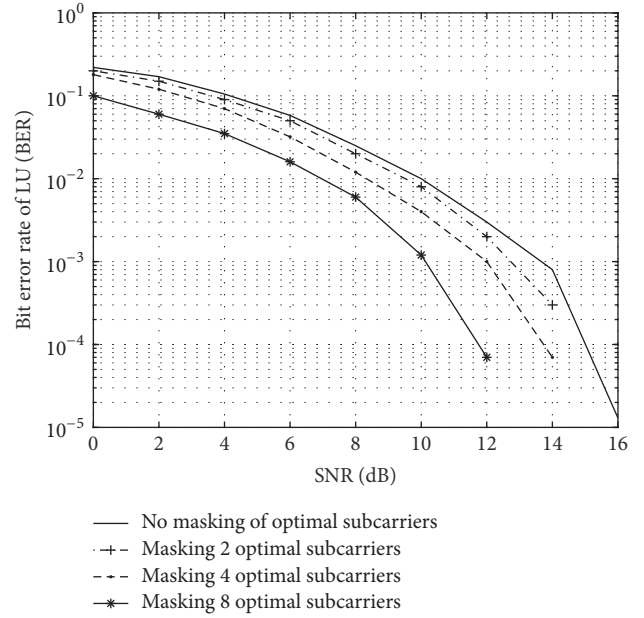


FIGURE 5: $p = 0, \theta_1 = \pi/5$, and BER performance of LU occupying central successive subbands based on Db(4).

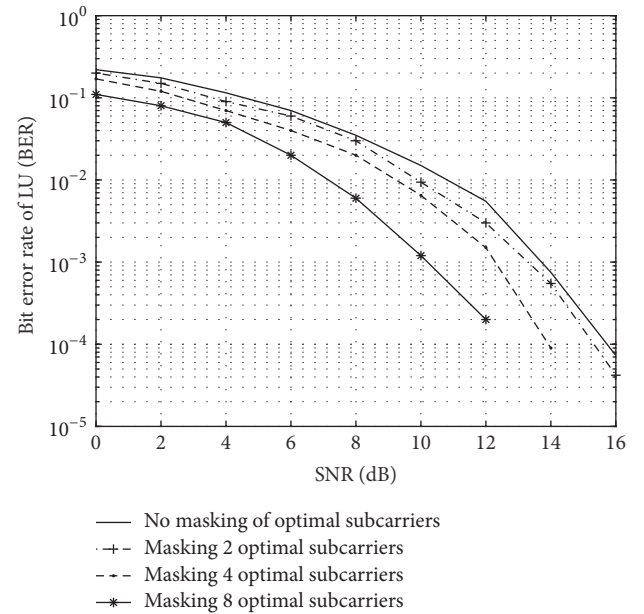


FIGURE 6: $p = 0, \theta_1 = \pi/5$, and BER performance of LU occupying 2 and 6 subbands based on Db(4).

6. Conclusions

The CR is a new method to share spectrum resources with more flexibility and efficiency. However, the orthogonality of LU signal and un-LU signal is disrupted because of multipath fading impulse. So, ICI between LU and un-LU occurs. GA can obtain and accumulate the related knowledge of search space automatically and control the search process adaptively to get the optimal solution. This paper proposes and discusses the GA used to obtain the optimal interference subcarriers

for ICI suppression. The average ICI energy of the j un-LU's subcarrier infecting LU is selected as the fitness function of the j un-LU's subcarrier.

Parallelizing the original algorithm is an effective method to improve the operation speed. So, the parallel ICI suppression algorithm is designed. The simulation results show that the average ICI power of LU can be improved by masking the optimal interference subcarriers. In addition, the BER performance of LU is improved. In the future, more self-learning optimization algorithms will be studied to obtain optimal interference subcarriers for suppressing the ICI of Spectrum Pooling.

Conflicts of Interest

The authors declare that they have no conflicts of interest.

Acknowledgments

This work was supported by the National Natural Science Foundation of China (no. 61601111) and Postdoctoral Scientific Research Developmental Fund of China (no. LBH-Q16309).

References

- [1] Z. I. A. M. Ahmed, K. H. D. Bilal, and D. M. M. Alhassan, "Cognitive radio network review," *International Journal of Engineering*, vol. 13, no. 1, pp. 320–327, 2016.
- [2] A. A. Khan, M. H. Rehmani, and M. Reisslein, "Cognitive radio for smart grids: survey of architectures, spectrum sensing mechanisms, and networking protocols," *IEEE Communications Surveys & Tutorials*, vol. 18, no. 1, pp. 860–898, 2016.
- [3] M. R. Mili and L. Musavian, "Interference efficiency: a new concept to analyze the performance of cognitive radio networks," in *Proceedings of the 2017 IEEE International Conference on Communications Workshops, ICC Workshops 2017*, pp. 1105–1110, France, May 2017.
- [4] B. Cao, Q. Zhang, and J. W. Mark, *Optimal Communication Strategies in Cooperative Cognitive Radio Networking*. Cooperative Cognitive Radio Networking, Springer International Publishing, 2016.
- [5] K. V. Krishnan, R. M. Sajith, and S. Khara, "Dynamic resource allocation in OFDM based cognitive radio system considering primary user QoS and secondary user proportional constraints," *Journal of Communications Technology and Electronics*, vol. 60, no. 11, pp. 1269–1275, 2015.
- [6] G. Singh and P. Mehta, "Implementation of optimization algorithm by sub-carriers assignment and power allocation for LTE and cognitive radio network using OFDM signal," *European Journal of Advances in Engineering and Technology*, vol. 2, no. 3, pp. 19–23, 2015.
- [7] D. Shahbazzabar and H. Farrokhi, "Designing non-contiguous orthogonal frequency division multiplexing transceiver based on wavelet transform and removable cyclic prefix for spectrum sharing in cognitive radio systems," *IET Communications*, vol. 8, no. 9, pp. 1508–1517, 2014.
- [8] M. Liu, K. Wang, Y. Huang, and X. Li, "Reducing PAPR by selecting optimal wavelet tree structure in WOFDM," *Computers and Electrical Engineering*, vol. 37, no. 3, pp. 253–260, 2011.
- [9] J. Chunkath, S. Arjun, V. Sheeba, and S. A. Raj, "Performance improvement of multicarrier systems using wavelet filter banks," *Procedia Technology*, vol. 24, pp. 775–781, 2016.
- [10] N. Taşpinar and Y. T. Bozkurt, "PAPR reduction using genetic algorithm in lifting-based wavelet packet modulation systems," *Turkish Journal of Electrical Engineering & Computer Sciences*, vol. 24, no. 1, pp. 184–195, 2016.
- [11] L. Miao, W. Ke, and H. Yan, "Adaptive guard bands for Spectrum Pooling," in *Proceedings of the 2010 2nd International Conference on Computer Engineering and Technology, ICCET 2010*, pp. V4103–V4107, China, April 2010.
- [12] L. Miao, L. Na, and Z.-X. Sun, "Optimal deactivated sub-carriers guard bands for spectrum pooling systems based on wavelet-based orthogonal frequency division multiplexing," *IET Communications*, vol. 8, no. 7, pp. 1117–1123, 2014.
- [13] B. G. Negash and H. Nikookar, "Wavelet-based multicarrier transmission over multipath wireless channels," *IEEE Electronics Letters*, vol. 36, no. 21, pp. 1787–1788, 2000.